GENERATING DIRECTED GRAPHS WITH DUAL ATTENTION AND ASYMMETRIC ENCODING

Anonymous authorsPaper under double-blind review

000

001

002 003 004

006

008

010 011

012

013

014

016

017

018

019

021

023

025

026

027

028

031

032

033

034

037

040

041

042

043

044

045

046

047

048

051

052

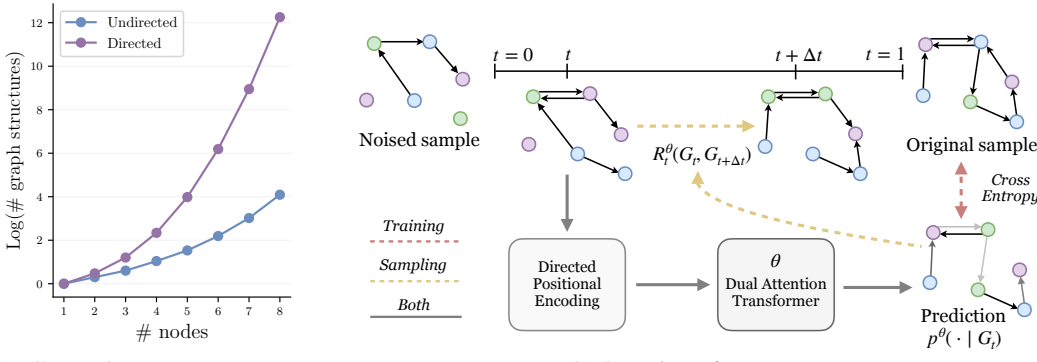
ABSTRACT

Directed graphs naturally model systems with asymmetric, ordered relationships, essential to applications in biology, transportation, social networks, or visual understanding. Generating such graphs enables simulation, data augmentation and novel instance discovery; however, this task remains underexplored. We identify two key reasons: first, modeling edge directionality introduces a substantially larger dependency space, making the underlying distribution harder to learn; second, the absence of standardized benchmarks hinders rigorous evaluation. Addressing the former limitation requires more expressive models that are sensitive to directional topologies. Thus, we propose DIRECTO, the first generative model for directed graphs built upon the discrete flow matching framework. Our approach combines: (i) a dual-attention mechanism distinctly capturing incoming and outgoing dependencies, (ii) a robust, discrete generative framework, and (iii) principled positional encodings tailored to asymmetric pairwise relations. To address the second limitation and support evaluation, we introduce a novel and extensive benchmark suite covering synthetic and real-world datasets. Experiments show that our method outperforms existing directed graph generation approaches across diverse settings and competes with specialized models for particular classes, such as directed acyclic graphs. These results highlight the effectiveness and generality of our approach, establishing a solid foundation for future research in directed graph generation.

1 Introduction

Directed graphs (digraphs) model systems with asymmetric relationships, capturing essential structures such as flows, dependencies, and hierarchies that arise in many real-world applications. This makes digraphs particularly well-suited for problems in diverse domains including biology (Li et al., 2006; Takane et al., 2023; Wei et al., 2024), transportation (Concas et al., 2022), social dynamics (Schweimer et al., 2022), and, more recently, image and video understanding (Chang et al., 2023; Rodin et al., 2023), where structured and directional representations are critical for interpretation and reasoning. Consequently, generating digraphs is central to tasks such as simulation, data augmentation and novel instance discovery in domains with directional structure.

Graph generative models have shown strong potential in diverse applications, including drug discovery (Mercado et al., 2020; Vignac et al., 2023b), finance (Li et al., 2023), social network modeling (Tsai et al., 2023), and medicine (Nikolentzos et al., 2023). However, most generative models focus on undirected graphs (Liao et al., 2019; Martinkus et al., 2022; Vignac et al., 2023a; Siraudin et al., 2024; Xu et al., 2024; Eijkelboom et al., 2024; Qin et al., 2025a), with only limited efforts on directed settings where recent works propose auto-regressive models for DAGs (Zhang et al., 2019; Li et al., 2025) and, more recently, for general digraphs (Law et al., 2025). We identify two main factors limiting progress in this direction. First, at the modeling level, the directed setting is inherently more challenging than its undirected counterpart, as edge directionality greatly enlarges the learnable space (see Figure 1a: for graphs with 4 nodes, there are 218 possible digraphs, compared to only 11 undirected ones). We will see that simply extending undirected architectures without explicit directional components fails on this larger space of digraphs. This is further amplified in settings where domain-specific structural constraints must be respected, such as directed acyclic graphs (DAGs). Second, beyond these technical challenges, we identify the lack of standardized benchmarks for directed graph generation as a barrier to rigorous evaluation and fair comparison. Current DAG methods (Li et al., 2025) typically rely only on proxy metrics derived from downstream tasks, with no established benchmarks to evaluate digraph generative quality systematically.



(a) Comparison on # structures.

(b) Overview of DIRECTO.

Figure 1: (a) The learnable space increases drastically with the number of nodes for digraphs compared to undirected graphs (Harary & Palmer, 1973), highlighting challenges in extending graph generative models to directed structures. (b) Overview of our generative model for directed graphs. During training, the *dual attention transformer* (denoising network), parameterized by θ , is enhanced with *asymmetric positional encoding*, learning to reverse predictions using cross-entropy loss. During inference, we compute the *rate matrix* $R_t^{\theta}(G_t, G_{t+\Delta t})$, which governs the evolution of the generative process over finite intervals Δt , based on the model prediction $p^{\theta}(\cdot \mid G_t)$.

To address the first challenge, we introduce DIRECTO¹, the first iterative refinement-based generative model for directed graphs. Our approach brings together three core components of expressive graph generative modeling: (i) an expressive neural architecture, (ii) a robust generative framework, and (iii) informative input features. For the architecture, we employ a dual attention mechanism that performs cross-attention between edge features and their reversed counterparts, capturing both source-to-target and target-to-source information flow. All this is integrated within a robust discrete-state flow matching framework that enables efficient generation with state-of-the-art performance and is also readily extendable to conditional generation tasks through classifier-free guidance (Ho & Salimans, 2022). Finally, the network's input features include positional encodings designed for asymmetric adjacency matrices, which we show outperform directionality-agnostic alternatives. Figure 1b gives an overview of our method and its components.

To tackle the second challenge, we propose a new benchmarking framework for rigorous evaluation of directed graph generation, spanning both synthetic and real-world datasets. The synthetic benchmarks cover different distributions, including acyclic and community-based graphs, while real-world benchmarks include a DAG dataset for *Neural Architecture Search* (NAS) (Phothilimthana et al., 2023) and a scene understanding dataset (Krishna et al., 2017). The evaluation metrics are systematic and tailored to directed graphs, including distributional distances for fidelity, and dataset-specific metrics reflecting the graph types used in different tasks. We evaluate DIRECTO on the proposed benchmarks, where it consistently outperforms prior approaches across all settings, underscoring its effectiveness on structurally diverse datasets. Extensive ablations further reveal that the dual attention mechanism is critical for modeling directional dependencies, while positional encodings play a role in enhancing overall generation quality.

Our main contributions are summarized as follows:

- (i) We propose DIRECTO, the first flow-based digraph generative model, combining a direction-aware dual attention block with positional encodings that capture asymmetric structure.
- (ii) We address the lack of benchmarks by releasing an evaluation suite covering synthetic graphs with relevant structural properties and real-world datasets with meaningful applications.
- (iii) We conduct an extensive empirical analysis demonstrating that DIRECTO achieves state-ofthe-art performance on structurally diverse synthetic and real-world graphs, while showing the need for a dedicated directed architecture.

Overall, by addressing the two main bottlenecks in directed graph generation, we propose an effective, new generative framework and provide standardized benchmarks, aiming to lay the groundwork for future research and to support real-world applications.

¹Code available at: https://anonymous.4open.science/r/DirectoAnonymous

2 BACKGROUND: DISCRETE FLOW MATCHING FOR GRAPH GENERATION

Notation We denote by $G = \left(x^{(1:n:N)}, \, e^{(1:i\neq j:N)}\right)$ directed graphs with N nodes. The set of nodes is denoted by $\{x^{(n)}\}_{n=1}^N$, and the set of directed edges by $\{e^{(i,j)}\}_{1\leq i\neq j\leq N}$. Both nodes and edges are categorical variables, where $x^{(n)} \in \{1,\ldots,X\}$ and $e^{(i,j)} \in \{1,\ldots,E\}$. Inspired by standard practice in iterative refinement for undirected graphs (Vignac et al., 2023a; Xu et al., 2024; Siraudin et al., 2024; Qin et al., 2025a), we assume that every ordered pair of distinct nodes corresponds to a directed edge in one of several possible classes, including a class representing an absent edge. Finally, we use a subscript t to denote variables at time t, e.g., $x_t^{(n)}$ or $e_t^{(i,j)}$.

Problem statement Graph generative models aim to learn the probability distribution of a set of observed graphs, enabling the generation of new samples that preserve structural and statistical properties. *Discrete Flow Matching* (DFM)-based models (Gat et al., 2024; Campbell et al., 2024) have recently achieved state-of-the-art performance in undirected graph generation (Qin et al., 2025a). DFM belongs to a broader class of discrete state-space methods that recover the original graph distribution p_1 by progressively denoising samples from a pre-specified noise distribution p_{noise} (Vignac et al., 2023a; Xu et al., 2024; Siraudin et al., 2024). It distinguishes itself from other methods in this class by decoupling sampling from training, allowing for post-training sampling optimization. Additionally, by operating directly in the discrete spaces, these methods naturally align with the discreteness of graphs and are well-suited to capture complex dependencies through iterative refinement. We hypothesize that this added expressivity is especially valuable for modeling the added complexity of digraphs. We now introduce the two main processes of DFM: *noising* and *denoising*.

Noising process The noising process runs from t=1 to t=0, progressively corrupting the original input graphs through a linear interpolation between the data distribution and the limit distribution $p_0 = p_{\text{noise}}$ (as detailed in Figure 1b). This interpolation is applied *independently* to each variable (Gat et al., 2024; Campbell et al., 2024), corresponding to each node and edge in the case of graphs. For example, for each node $x_1^{(n)}$, its noisy distribution at step t is defined as:

$$p_{t|1}^{X}(x_t^{(n)} \mid x_1^{(n)}) = t \,\delta(x_t^{(n)}, x_1^{(n)}) + (1 - t) \,p_{\text{noise}}^{X}(x_t^{(n)}),\tag{1}$$

where $\delta(\cdot, \cdot)$ denotes the Kronecker delta and p_{noise}^X is the limit distribution over node categories. A similar construction is used for the edges (Qin et al., 2025a).

Denoising process The denoising process aims to reverse the noising trajectory, running from t = 0 to t = 1. It is formulated as a *Continuous-Time Markov Chain* (CTMC), which starts sampling a noisy graph $G_0 \sim p_0$ and evolves according to:

$$\mathbf{p}_{t+\Delta t|t}(G_{t+\Delta t} \mid G_t) = \boldsymbol{\delta}(G_t, G_{t+\Delta t}) + \mathbf{R}_t(G_t, G_{t+\Delta t}) \,\mathrm{d}t, \tag{2}$$

where R_t is the CTMC rate matrix (Campbell et al., 2024). In practice, this update rule is approximated in two ways: first, by discretizing time with a finite step size Δt , in an Euler method step; and second, by approximating the ground-truth rate matrix with an estimate R_t^{θ} computed from the predictions of a denoising neural network $p_{1|t}^{\theta}(\cdot \mid G_t)$ parametrized by θ . This network is trained to predict the clean node $p_{1|t}^{\theta,(n)}$ and edge $p_{1|t}^{\theta,(i,j)}$ distributions given a noisy graph, aggregated as:

$$\mathbf{p}_{1|t}^{\theta}(\cdot|G_t) = \left(\left(\mathbf{p}_{1|t}^{\theta,(n)}(x_1^{(n)} \mid G_t) \right)_{1 \le n \le N}, \left(\mathbf{p}_{1|t}^{\theta,(i,j)}(e_1^{(i,j)} \mid G_t) \right)_{1 \le i \ne j \le N} \right). \tag{3}$$

This network is trained using a cross-entropy loss independently to each node and each edge:

$$\mathcal{L} = \mathbb{E}_{t,G_1,G_t} \left[-\sum_{n} \log \left(p_{1|t}^{\theta,(n)} \left(x_1^{(n)} \mid G_t \right) \right) - \lambda \sum_{i \neq j} \log \left(p_{1|t}^{\theta,(i,j)} \left(e_1^{(i,j)} \mid G_t \right) \right) \right], \quad (4)$$

where the expectation is taken over time t, sampled from a predefined distribution over [0,1] (e.g., uniform); $G_1 \sim p_1(G_1)$ is a clean graph from the dataset; and $G_t \sim p_t(G_t|G_1)$ is its noised version at time t (Qin et al., 2025a). The hyperparameter $\lambda \in \mathbb{R}^+$ controls the relative weighting between node and edge reconstruction losses. Further details are provided in Appendix I.

3 GENERATING DIGRAPHS WITH ASYMMETRIC ENCODING AND DUAL ATTENTION

In this section, we introduce DIRECTO, the first flow-based digraph generative model. We begin by outlining the overall generative framework, followed by the two directionality-aware components that form the core of DIRECTO: asymmetric positional encoding and dual attention.

3.1 DIRECTED GRAPH GENERATION VIA DISCRETE FLOW MATCHING

Building on the formulation of Section 2, we extend DFM to the directed graph setting. To address the added complexity of asymmetric adjacency matrices in digraphs (Figure 1a), we exploit a key strength of DFM: the decoupling of training and sampling. This enables post-training optimizations such as time-adaptive schedules and custom CTMC rate matrices Qin et al. (2025a), which we can extend to directed graphs (details in Appendix C). While these strategies improve performance (see Appendix H.8), they remain insufficient to capture the structural properties of digraphs (see Section 5). We therefore introduce architectural components explicitly tailored for directionality-aware graph generation, providing the complete training and sampling algorithms in Appendix D.

3.2 ASYMETRIC POSITIONAL ENCODING

Our generative framework employs a denoising GNN, which inherently struggles to capture global or higher-order patterns due to the locality of message passing (Xu et al., 2019; Morris et al., 2019). To maximize the capacity of our method, we augment our GNN with positional encodings (PEs) that inject structural information beyond local neighborhoods (Beaini et al., 2021; Bouritsas et al., 2020). Common choices for undirected graphs include Laplacian eigenvectors or shortest-path distances, effective in enriching node and edge representations (Vignac et al., 2023a; Qin et al., 2025a). However, these encodings do not respect edge directionality, failing to distinguish asymmetric structural roles. To overcome this, we adopt direction-aware positional encodings (Geisler et al., 2023; Huang et al., 2025) that account for both outgoing and incoming connectivity. We append them to node and edge features, allowing our model to better capture the structural dependencies unique to digraphs.

Specifically, we experiment with three families of encodings: (i) the **Magnetic Laplacian** (**MagLap**) (Geisler et al., 2023), which introduces complex-valued phase shifts into the standard Laplacian to retain edge orientation; (ii) its **Multi-**q **MagLap** extension (Huang et al., 2025), which stacks Q Multiple Magnetic Laplacians with different complex potentials to provide richer representations; and (iii) **Directed Relative Random Walk Probabilities** (**RRWP**) (Geisler et al., 2023), which combine forward and reverse transition probabilities to capture outgoing and incoming asymmetric flows. These encodings are designed to provide direction-sensitive structural signals that better reflect the properties of directed graphs, and are described in detail in Appendix B.

We hypothesize that incorporating directionality-aware positional encodings improves digraph generative performance. To test this, we design an ablation study evaluating which of the described encodings provide the most informative structural signals, while also considering their computational cost, to identify the best tradeoff between performance and efficiency.

3.3 Graph transformer with dual attention

Graph Transformers (Dwivedi & Bresson, 2021; Rampášek et al., 2022) effectively model node interactions by leveraging the adjacency matrix to encode structural information. However, in directed graphs, it is crucial for the model to distinguish the different semantics carried by incoming and outgoing edges, which makes the standard graph transformer insufficiently expressive. Generating digraphs thus requires models that (i) capture bidirectional information flow to learn how source and target nodes influence each other distinctly, and (ii) integrate structural signals across nodes, edges, and the global graph to preserve relational dependencies and ensure coherent outputs.

To address this, our model jointly processes stacked node features \boldsymbol{X} , edge features \boldsymbol{E} , and global features \boldsymbol{y} through a Transformer composed of L layers of a dual attention block (see Figure 2). This dual attention mechanism introduces two key components: (i) an attention-based aggregation scheme that captures directional information, and (ii) modulation layers to incorporate information at different levels of granularity across nodes, edges, and the global graph structure.

Bidirectional information flow via dual attention aggregation To model directional dependencies more effectively, we use a cross-attention mechanism between source-to-target (outgoing)

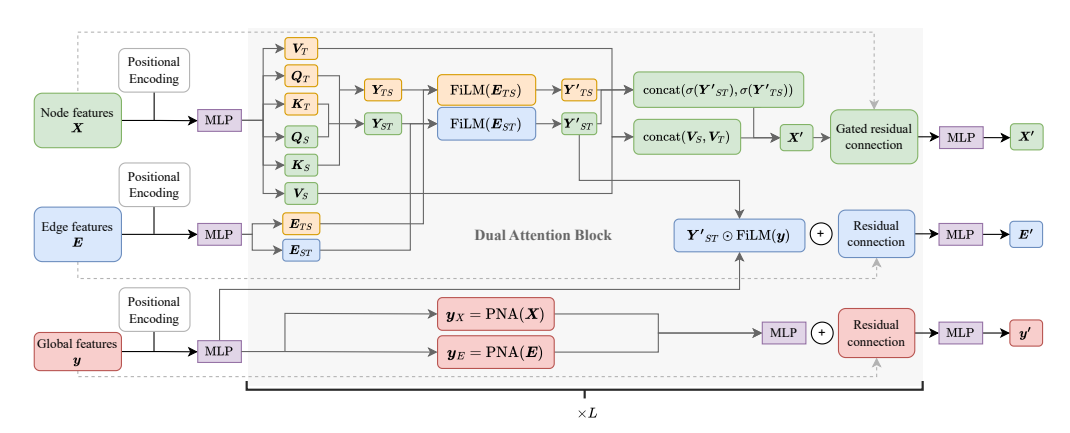


Figure 2: Network architecture of DIRECTO. We stack L dual attention layers that account for both source-to-target and target-to-source information via cross-attention mechanisms. X, E and y denote the stacked input node, edge, and global features. X', E' and y' are the output of the model, i.e., predicted clean node and edge distribution, and graph feature. FiLM (Perez et al., 2018) and PNA pooling layers (Corso et al., 2020) are incorporated to enable flexible modulation between node, edge, and graph-level features. Full technical details are provided in Appendix A.

edge features $E_{\rm ST}$ and their reversed target-to-source (incoming) counterparts $E_{\rm TS}$. By explicitly attending to both directions, our architecture, which builds on ideas from Wang et al. (2024), reasons bidirectionally and better captures directed relationships, improving expressiveness and accuracy. Concretely, we compute two directional attention maps between role-specific node projections:

$$\mathbf{Y}_{ST}[i,j] = \frac{\mathbf{Q}_{S}[i] \cdot \mathbf{K}_{T}[j]}{\sqrt{d_q}}, \quad \mathbf{Y}_{TS}[i,j] = \frac{\mathbf{Q}_{T}[i] \cdot \mathbf{K}_{S}[j]}{\sqrt{d_q}},$$
 (5)

where Q_S , Q_T , K_S , and K_T are the role-specific projections for nodes that act as the source or the target of an edge, respectively, and d_q is the query feature dimension. These attention weights are modulated through a FiLM layer (see Equation (8)) using edge features to enable effective reasoning, producing the updated attention maps Y'_{TS} and Y'_{TS} .

To further consolidate directional information, we introduce an *attention aggregation mechanism*. Instead of treating the attentions from the two directions independently, we concatenate the modulated attention maps and apply a single softmax operation to obtain unified attention weights:

$$\boldsymbol{A}_{\mathrm{aggr}} = \mathrm{softmax}(\mathrm{concat}(\boldsymbol{Y}_{\mathrm{ST}}', \boldsymbol{Y}_{\mathrm{TS}}')) \in \mathbb{R}^{n \times 2n}, \quad \boldsymbol{V}_{\mathrm{aggr}}^{\top} = \mathrm{concat}(\boldsymbol{V}_{\mathrm{S}}^{\top}, \boldsymbol{V}_{\mathrm{T}}^{\top}) \in \mathbb{R}^{2n \times h}, \quad (6)$$

where h is the hidden dimension, V_S , V_T are the value vectors for source and target nodes, and the concatenation operation is performed along the node dimensions. These unified weights are then used to aggregate the value vectors through weighted summation:

$$X' = A_{\text{aggr}} V_{\text{aggr}} \in \mathbb{R}^{n \times h}. \tag{7}$$

This aggregation allows the model to assign asymmetric importance to the outgoing and the incoming directions. The node features are then updated using a gated residual connection, which adaptively combines the original and updated features by learning a gate that controls how much of the new information should be integrated in the update.

Multi-scale information modulation for graph denoising A graph denoising model should predict clean node and edge types from noisy inputs, which requires integrating both local interactions and global structure from node, edge, and graph-level features. Building on standard graph generation architectures (Vignac et al., 2023a; Siraudin et al., 2024; Qin et al., 2025a), we incorporate *Feature-wise Linear Modulation* (FiLM) (Perez et al., 2018) and *Principal Neighbourhood Aggregation* (PNA) (Corso et al., 2020) layers to enhance multi-scale feature fusion. FiLM adaptively modulates edge features using attention signals: given the edge feature matrix E, the attention matrix $E_{\rm attn}$, and the learnable weights $W^1_{\rm FiLM}$, $W^2_{\rm FiLM}$, it computes

$$FiLM(E, E_{attn}) = EW_{FiLM}^1 + (EW_{FiLM}^2) \odot E_{attn} + E_{attn}, \tag{8}$$

where \odot denotes element-wise multiplication. These layers are also used to integrate global graph-level signals y into the construction of edge features.

To complement this, PNA layers aggregates multi-scale neighborhood information via pooling operations: given node (or edge) features $X \in \mathbb{R}^{n \times h}$ and a learnable weight matrix W_{PNA} :

$$PNA(\boldsymbol{X}) = \operatorname{concat}(\max(\boldsymbol{X}), \min(\boldsymbol{X}), \operatorname{mean}(\boldsymbol{X}), \operatorname{std}(\boldsymbol{X})) \, \boldsymbol{W}_{PNA} \in \mathbb{R}^{4h}, \tag{9}$$

with concatenation performed along the feature dimension. We use PNA layers to update global graph signals based on local node- and edge-level information at each attention pass. Together, these components enable expressive and scalable integration of local and global features, allowing the model to capture higher-order structure which is critical for accurate graph denoising.

4 BENCHMARKING DIRECTED GRAPH GENERATION

Despite growing interest in digraphs (Sun et al., 2024), benchmarking in this area remains underdeveloped (Bechler-Speicher et al., 2025). Existing approaches typically rely on downstream task performance, failing to directly evaluate generative quality. With the objective of establishing standard datasets and metrics, we propose a comprehensive benchmark that covers synthetic and real-world digraphs, along with tailored metrics that directly assess key generative qualities, including sample validity, diversity, and distributional alignment.

4.1 Datasets

To enable systematic evaluation, we introduce a suite of synthetic directed datasets alongside two real-world use cases: (i) neural architecture search (NAS), where DAGs model computational pipelines, and (ii) scene graphs, where directed edges encode semantic relations in visual scenes. Further details and statistics for all datasets are available in Appendix E.

Synthetic datasets We sample from the directed and DAG Erdős–Rényi (binomial) model; from Price's model, a directed analogue of the Barabási–Albert model that produces DAGs; and from a directed version of the Stochastic Block Model (SBM) dataset proposed in Martinkus et al. (2022). Each dataset comprises 200 graphs, split into 128 training, 32 validation, and 40 test graphs.

Real-world datasets A relevant application of DAGs is Neural Architecture Search, which aims to generate novel instance to achieve an automated design of efficient Neural Networks (Elsken et al., 2019). The TPU Tiles dataset (Phothilimthana et al., 2023) contains computational graphs extracted from Tensor Processing Unit workloads, split into 5,040 training, 630 validation, and 631 test graphs following Li et al. (2025). On the other hand, the Visual Genome dataset (Krishna et al., 2017), is a widely adopted benchmark for scene graph generation, supporting tasks such as image retrieval, captioning, or visual question answering. The resulting graphs are not acyclic but instead represent general directed structures, with nodes corresponding to objects (entities), relationships (directed interactions), or attributes (object properties). We extract 203 training, 51 validation, and 63 test graphs. Generating new samples is useful for data augmentation, or scenario simulation, and complements recent scene-to-image generation work (Johnson et al., 2018; Yang et al., 2022).

4.2 METRICS

To evaluate digraph generations, we build upon the evaluation metrics from the undirected graph generation literature (Martinkus et al., 2022; Bergmeister et al., 2024; Thompson et al., 2022) and further extend the ones already present in the directed setting (Law et al., 2025).

Validity, uniqueness, and novelty For synthetic datasets, *validity* is assessed via statistical tests of adherence to the generative distribution and, for DAG datasets, by ensuring acyclicity. On the TPU Tiles dataset, we measure acyclicity, while for Visual Genome we check typed structural constraints (e.g., edges go from objects to attributes and relationships, and from relationships to objects). To measure generative diversity while avoiding memorization, we compute *uniqueness* (fraction of non-isomorphic generated graphs) and *novelty* (fraction of generated graphs not in the training set). The V.U.N. ratio reports the proportion of samples that are simultaneously valid, unique, and novel.

Structure distributional alignment To evaluate proximity to the original distribution, we compute the Maximum Mean Discrepancy (MMD) (Martinkus et al., 2022) between generated and test graphs across several statistics: outgoing and incoming degree distributions, directed clustering coefficients, spectral, and wavelet-based features. Spectral features are derived from the directed Laplacian (Chung, 2005), simplifying computations compared to the Magnetic Laplacian. We normalize results as the ratio from the generated samples MMD to that of the training data and then average the ratios.

Table 1: Directed graph generation performance for different configurations of DIRECTO. Results are the mean \pm standard deviation across five sampling runs. We considered Q=10 for MagLap in the synthetic datasets and Q=5 in the real-world ones (due to the computational cost of this positional encoding). OOT indicates that the model could not be run within a reasonable timeframe.

	ER-DAG SBM TPU Tiles				Visual Genome					
Model	Ratio ↓	V.U.N. ↑	Ratio ↓	V.U.N. ↑	Ratio ↓	V.U.N. ↑	RBF ↓	Ratio ↓	V.U.N. ↑	RBF ↓
Training set	1.0	0.0	1.0	0.0	1.0	0.0	0.002	1.0	0.0	0.021
MLE D-VAE	15.1 ± 0.2 106.6 ± 5.4	0.0 ± 0.0 0.0 ± 0.0	11.6 ± 0.2	0.0 ± 0.0	149.8 ± 0.7 OOT	24.7 ± 0.0 OOT	1.039 ± 0.033 OOT	17.0 ± 0.6	0.0 ± 0.0	0.618 ± 0.025
LayerDAG DiGress DeFoG	$\begin{array}{c} 4.2 \pm 3.2 \\ 1.9 \pm 0.3 \\ 1.6 \pm 0.2 \end{array}$	$\begin{array}{c} 21.5 \pm 2.7 \\ 34.0 \pm 4.1 \\ 75.0 \pm 2.2 \end{array}$	3.9 ± 0.9 4.3 ± 0.8	$41.5 \pm 5.1 \\ 37.0 \pm 6.6$	$413.6 \pm 70.1 \\ \underline{57.5} \pm 1.7 \\ 63.7 \pm 2.6$	98.5 ± 3.0 70.9 ± 3.4 72.0 ± 2.4	$\begin{array}{c} 1.021 \pm 0.023 \\ 0.097 \pm 0.033 \\ 0.059 \pm 0.015 \end{array}$	$17.0 \pm 0.6 \\ 10.8 \pm 0.7$	$\begin{array}{c} -0.3 \pm 0.6 \\ 50.8 \pm 8.4 \end{array}$	$\begin{array}{c} - \\ 0.232 \pm 0.028 \\ 0.085 \pm 0.023 \end{array}$
DIRECTO-DD RRWP DIRECTO-DD MagLap DIRECTO RRWP DIRECTO MagLap	$\frac{1.4 \pm 0.3}{1.5 \pm 0.2}$ 1.7 ± 0.1 1.3 ± 0.2	79.0 ± 3.7 85.0 ± 9.2 94.0 ± 1.0 92.0 ± 3.7	$\frac{1.7}{1.5} \pm 0.4$ 1.8 ± 0.5 2.0 ± 0.3	81.5 ± 3.2 95.5 ± 3.7 99.5 ± 1.0 96.5 ± 2.5	61.0 ± 2.9 64.3 ± 5.3 75.4 ± 8.1 44.0 ± 7.1	76.8 ± 1.9 77.0 ± 7.0 77.0 ± 2.9 80.5 ± 4.6	$\begin{array}{c} 0.058 \pm 0.023 \\ 0.079 \pm 0.027 \\ \underline{0.044} \pm 0.018 \\ \hline \textbf{0.042} \pm 0.001 \end{array}$	15.3 ± 0.8 7.6 ± 0.7 12.8 ± 0.6 6.2 ± 0.5	$\frac{72.7}{61.9} \pm 3.9$ 83.8 ± 4.3 67.0 ± 4.3	0.039 ± 0.004 0.042 ± 0.006 0.038 ± 0.005 0.051 ± 0.012

Joint node-edge distributional alignment To better capture performance on attributed graphs, we extend evaluation beyond structural statistics to joint node-edge distributions. Specifically, we measure MMD over label histograms to assess coverage of categorical proportions. We also compute triplet-based precision and recall by matching semantic tuples (e.g., (object, relation, object)) between generated and test graphs. Finally, we evaluate embedding-based distances (MMD with RBF kernel and FID) over GNN-derived representations that encode both labels and structure (Thompson et al., 2022). These metrics provide a comprehensive view of alignment with the reference distribution.

Among all metrics, we consider V.U.N. and the average ratio as the most informative for structural distributional alignment, and the RBF MMD for the joint node-label distributional alignment in real-world datasets. Additional details on the evaluation metrics are provided in Appendix F.

5 EXPERIMENTS

In this Section, we first evaluate the flexibility of our method to generate digraphs across two of the synthetic and both real-world datasets. Then, we analyze the role of the proposed architectural improvements on generative performance and analyze scalability and conditional generation.

Baselines In the general directed setting, we compare DIRECTO to a Maximum Likelihood Estimation (MLE) baseline of the node count, node types, and edge types. For DAG settings, we also include the only two publicly available baselines: D-VAE (Zhang et al., 2019) and LAYERDAG (Li et al., 2025). Notably, the architectural improvements in Sections 3.2 and 3.3 are agnostic to the underlying iterative refinement framework. To demonstrate versatility and enable wider experimentation, we extend DIRECTO to a discrete diffusion (Vignac et al., 2023a) backbone (DIRECTO-DD), described in Appendix I.3. We also include DEFOG (Qin et al., 2025a) and DIGRESS (Vignac et al., 2023a), discrete flow matching and diffusion methods in the undirected setting, respectively, adapting both to the directed case by removing edge symmetrization. For each experiment, we highlight the **best result** and <u>second-best</u> method, with further experimental details in Appendix G.

5.1 GENERATIVE PERFORMANCE EVALUATION

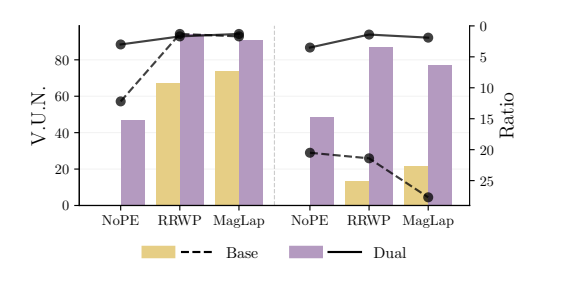
Synthetic datasets Table 1 reports the results on two synthetic datasets: ER-DAG and SBM. In both settings, DIRECTO consistently achieves the best trade-off between sample quality and validity. For ER-DAG, it achieves the highest validity score using directed RRWP as positional encoding, with a V.U.N. ratio of 94%. Notably, while LAYERDAG enforces acyclicity by design, it fails to capture the ER structure of the target graph distribution, as evidenced by its low V.U.N. score (21.5%; see Table 16 for details). In the SBM case, DIRECTO also successfully captures the distribution and consistently outperforms the baselines, achieving up to 99.5% in V.U.N. ratio and keeping low average graph statistics ratios. We provide the complete results for the distributional alignment metrics and the results for the other two synthetic datasets in Appendices H.1 and H.4.

Real-world datasets Table 1 shows the performance for the two real-world datasets. In TPU tiles, all DIRECTO variants significantly outperform DAG generation baselines in terms of structure-aware metrics. The ratio scores for DIRECTO are consistently and substantially lower than those observed in MLE, and especially LayerDAG, which indicates a more realistic distribution. Again, DIRECTO variants achieve higher V.U.N. than all baselines, with the exception of LAYERDAG, which benefits

from enforcing acyclicity, the only validity constraint evaluated in this case. For Visual Genome, results reinforce the versatility of DIRECTO. DIRECTO RRWP achieves the highest V.U.N., indicating a superior ability to generate diverse and novel graphs while maintaining structural fidelity. Finally, we also see that DIRECTO achieves the lowest RBF MMD score for both datasets, demonstrating that the model is successful in capturing the joint node-label dependencies of the distribution in the original dataset. Complete results are available in Tables 10 and 11 in Appendix H.2.

5.2 Ablations and further experiments

Impact of dual attention We now analyze the influence of the dual attention mechanism on the performance of DIRECTO. In Figure 3, we compare the V.U.N metric and the average graph statistics ratios ("Ratio") score across both synthetic datasets (ER-DAG and SBM), highlighting the impact of dual attention on generation quality and graph realism. We observe that the dual attention mechanism consistently improves generative performance, regardless of the positional encoding it is combined with. Notably, even in the absence of any positional encoding ("No PE"), dual attention still achieves non-zero V.U.N., highlighting its capacity to independently capture directionality-relevant information. See Appendix H.3 for the full ablation tables, both for DIRECTO and DIRECTO-DD.



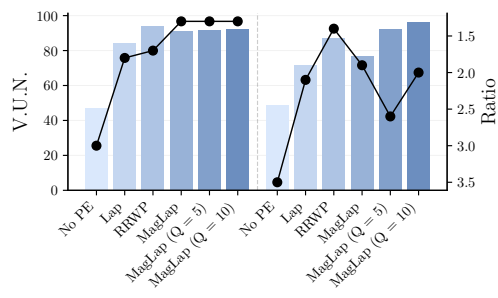


Figure 3: Ablation results for dual attention (left) and positional encodings (right). Each plot shows results on the ER-DAG (left bars/lines) and SBM (right bars/lines) datasets. Better performance corresponds to V.U.N. bars and Ratio lines appearing closer to the top of each subplot.

Impact of positional encodings We also evaluate the sensitivity of DIRECTO to different positional encodings, including a direction-agnostic baseline with the Laplacian ("Lap") on synthetic datasets (see Appendix B for details on how it is computed using the symmetrized adjacency matrix). In Figure 3, we observe consistent trends across datasets: integrating positional encodings improves V.U.N. and Ratio, mirroring the undirected setting; moreover, direction-aware encodings outperform agnostic ones, supporting our modeling hypothesis. Among the encodings tested, Directed RRWP achieves the best overall performance on ER-DAG, and MultiMagLapPE with Q=10 on SBM. Nevertheless, we remark that RRWP demonstrates clear superiority in both scalability and runtime efficiency (see Appendix G.3). Overall, while positional encodings contribute to performance, the dual attention mechanism remains the most critical component for capturing directional dependencies. Full tables for both DIRECTO and DIRECTO-DD can be found in Appendix H.4.

Scalability study We investigate scalability across three axes: dataset size, parameter efficiency, and graph size (Appendix H.6). Increasing the amount of training data improves performance but comes with longer training time (Table 17). For parameter efficiency, our dual attention mechanism demonstrates clear higher performance then simply enlarging the adapted undirected model, as can be seen in Table 2. Finally, while larger graphs pose challenges, particularly for enforcing strict acyclicity, DIRECTO achieves strong generation quality (Ratio) across all graph sizes commonly used in the literature of the applications explored in this paper (Table 20).

Table 2: Directed graph generation performance for the dual attention mechanism versus doubling the depth of the standard network.

Dataset	Model	Ratio \downarrow	V.U.N. ↑
ER-DAG	RRWP - Double RRWP - Dual MagLap - Double MagLap - Dual	4.9 ± 0.2 1.7 ± 0.1 4.3 ± 0.7 1.3 ± 0.2	72.0 ± 9.8 94.0 ± 1.0 80.0 ± 6.3 91.0 ± 2.5
SBM	RRWP - Double RRWP - Dual MagLap - Double MagLap - Dual	27.1 ± 2.3 1.4 ± 0.2 24.8 ± 4.6 1.9 ± 0.3	0.0 ± 0.0 87.0 ± 5.1 6.0 ± 4.9 77.0 ± 7.6

Conditional generation As groundwork for directed graph generation, we prioritize strong unconditional generation, which we consider a key prerequisite for effective digraph modeling. At the same

time, steering generation with graph-level properties is important for many downstream tasks. To illustrate the flexibility of our framework, we show that DIRECTO can be extended to conditional generation without major architectural changes via classifier-free guidance (Ho & Salimans, 2022). On TPU Tiles, we condition on the execution time of the computational graph, aiming at low execution times. DIRECTO performs competitively with specialized autoregressive models like GraphRNN and LayerDAG (Appendix H.7), even surpassing the OneShotDAG variant of Li et al. (2025).

6 RELATED WORK

Graph generative methods Initial methods include *auto-regressive* models (You et al., 2018; Liao et al., 2019), which grow the graph progressively by inserting nodes and edges, but require node ordering for feasibility. On the other hand, one-shot graph generative models such as VAEs (Kipf & Welling, 2016; Simonovsky & Komodakis, 2018; Jin et al., 2018; Ma & Zhang, 2021; Vignac & Frossard, 2022), GANs (De Cao & Kipf, 2018; Krawczuk et al., 2021; Martinkus et al., 2022), and normalizing flows (Kaushalya et al., 2019; Wehenkel & Louppe, 2021; Lippe & Gavves, 2021; Luo et al., 2021b) can directly generate full graphs in a single forward pass, thereby eliminating the need for predefined node ordering. Graph diffusion models also belong to this class, with the initial approaches consisting of adaptations of continuous state-space discrete-time diffusion frameworks (Sohl-Dickstein et al., 2015; Ho et al., 2020; Song & Ermon, 2019) to the graph setting. These include works such as EDP-GNN (Niu et al., 2020), DGSM (Luo et al., 2021a), and GeoDiff (Xu et al., 2022). Later, the discrete state-space diffusion framework (Austin et al., 2021) was adopted, with DiGress (Vignac et al., 2023a) and MCD (Haefeli et al., 2022) operating in discrete time. On the other hand, methods that operate in continuous time (Song et al., 2021; Campbell et al., 2022) were introduced, including GDSS (Jo et al., 2022) and GruM (Jo et al., 2024) in continuous state-spaces and DisCo (Xu et al., 2024) and Cometh (Siraudin et al., 2024) for discrete state-spaces. Recent approaches combine the sequential modeling of auto-regressive methods with the global denoising of diffusion (Zhao et al., 2024). Finally, DeFoG (Qin et al., 2025a) recently achieves state-of-the-art performance by leveraging discrete flow matching (Campbell et al., 2024; Gat et al., 2024).

Directed graph generation The vast majority of works in this area focus solely on DAG generation, with research including autoencoders (Zhang et al., 2019), autoregressive methods (Li et al., 2022) and, more recently, combining diffusion in different steps of an auto-regressive process (Li et al., 2025). However, they require the input DAGs to be topologically ordered, which can result in higher computational cost. Other approaches (Asthana et al., 2024; An et al., 2024) use ideas from discrete diffusion for Neural Architecture Search (NAS), but they are tailored to the specific application and, therefore, to DAGs. Finally, Law et al. (2025) are the first to propose a general digraph generation method from an auto-regressive perspective. Unfortunately, to the best of our knowledge, its implementation is not publicly available, limiting its accessibility for study and evaluation.

7 CONCLUSION AND FUTURE DIRECTIONS

We propose DIRECTO, a discrete flow matching-based method for directed graph generation. It combines directionality-aware positional encodings with a dual-attention mechanism that handles both source-to-target and target-to-source dependencies, overcoming the limitations of naïve extensions from undirected models. We also introduce a dedicated benchmarking framework to address the lack of standardized evaluation. Empirical results show that DIRECTO outperforms existing baselines on synthetic and real-world datasets, successfully generating directed structures and preserving key properties, such as acyclicity, without explicit constraints, highlighting its generality and robustness.

Limitations and future directions Despite these promising results, limitations remain. First, scalability can be further improved in handling larger datasets and graph sizes (a direct result of the combinatorial complexity of digraphs). Incorporating scalable strategies, such as sparsity-aware attention (Qin et al., 2025b), hierarchical (Bergmeister et al., 2024; Jang et al., 2024), or latent diffusion (Yang et al., 2024), could help extend DIRECTO at scale. Second, although our current setup includes classifier-free conditional generation, exploring alternative conditional strategies could further improve performance. Third, while DIRECTO can learn structural properties like acyclicity implicitly, enforcing such constraints (e.g., via PRODIGY (Sharma et al., 2024) or ConStruct (Madeira et al., 2024)) could further improve controllability and domain-specific validity. Exploring these directions would enhance the applicability and impact of digraph generative models, particularly on new real-world scenarios. Appendix L includes a detailed discussion of limitations and future work.

REPRODUCIBILITY STATEMENT

To ensure the reproducibility of our results, we have taken the following steps. An anonymous implementation of our method is provided in an anonymous repository, including all code and scripts necessary to reproduce the experiments and details on how to run it. In addition, we detail the proposed algorithm in Appendix D, while Appendix G provide full descriptions of baselines, training setup, and hyperparameters employed. We also report the computational resources used and the runtime required for all experiments. Together, these materials are intended to enable researchers to fully replicate and build upon our work.

ETHICS STATEMENT

The objective of this work is to advance methodologies for the generation of directed graphs by introducing architectural mechanisms that explicitly model directionality and asymmetric relationships. Directed graphs are central to a wide range of applications, including causal inference, traffic modeling, and biological network analysis. Accordingly, improvements in directed graph generation have the potential to support progress in scientific research, decision-making systems, infrastructure design, or causal discovery.

The proposed framework enhances the expressiveness of generative models to directed graphs, and, at the moment, we do not identify any immediate societal risks associated with its deployment in its current form. Moreover, although the method is capable of generating structured and semantically meaningful graphs, the scale and complexity of these outputs remain limited, which may difficult direct applicability in high-impact domains such as real-time clinical diagnostics or large-scale policy modeling at this stage.

REFERENCES

- Sohyun An, Hayeon Lee, Jaehyeong Jo, Seanie Lee, and Sung Ju Hwang. DiffusionNAG: predictor-guided neural architecture generation with diffusion models. In *International Conference on Learning Representations (ICLR)*, 2024.
- Rohan Asthana, Joschua Conrad, Youssef Dawoud, Maurits Ortmanns, and Vasileios Belagiannis. Multi-conditioned Graph Diffusion for Neural Architecture Search. *Transactions on Machine Learning Research (TMLR)*, 2024.
- Jacob Austin, Daniel D Johnson, Jonathan Ho, Daniel Tarlow, and Rianne Van Den Berg. Structured denoising diffusion models in discrete state-spaces. In Advances in Neural Information Processing Systems (NeurIPS), 2021.
- Dominique Beaini, Saro Passaro, Vincent Létourneau, Will Hamilton, Gabriele Corso, and Pietro Lió. Directional Graph Networks. In *International Conference on Machine Learning (ICML)*, Proceedings of Machine Learning Research, 2021.
- Maya Bechler-Speicher, Ben Finkelshtein, Fabrizio Frasca, Luis Müller, Jan Tönshoff, Antoine Siraudin, Viktor Zaverkin, Michael M. Bronstein, Mathias Niepert, Bryan Perozzi, Mikhail Galkin, and Christopher Morris. Position: Graph Learning Will Lose Relevance Due To Poor Benchmarks. In *International Conference on Machine Learning (ICML)*, 2025.
- Andreas Bergmeister, Karolis Martinkus, Nathanaël Perraudin, and Roger Wattenhofer. Efficient and Scalable Graph Generation through Iterative Local Expansion. In *International Conference on Learning Representations (ICLR)*, 2024.
- Giorgos Bouritsas, Fabrizio Frasca, Stefanos Zafeiriou, and Michael M. Bronstein. Improving graph neural network expressivity via subgraph isomorphism counting. *IEEE Transactions on Pattern Analysis and Machine Intelligence (TPAMI)*, 2020.
- Andrew Campbell, Joe Benton, Valentin De Bortoli, Thomas Rainforth, George Deligiannidis, and Arnaud Doucet. A continuous time framework for discrete denoising models. In *Advances in Neural Information Processing Systems (NeurIPS)*, 2022.

- Andrew Campbell, Jason Yim, Regina Barzilay, Tom Rainforth, and Tommi Jaakkola. Generative flows on discrete state-spaces: Enabling multimodal flows with applications to protein co-design. In *International Conference on Machine Learning (ICML)*, 2024.
 - Xiaojun Chang, Pengzhen Ren, Pengfei Xu, Zhihui Li, Xiaojiang Chen, and Alex Hauptmann. A Comprehensive Survey of Scene Graphs: Generation and Application. *IEEE Transactions on Pattern Analysis and Machine Intelligence (TPAMI)*, 2023.
 - Fan Chung. Laplacians and the Cheeger inequality for directed graphs. *Annals of Combinatorics*, 9: 1–19, 2005.
 - Anna Concas, Caterina Fenu, Lothar Reichel, Giuseppe Rodriguez, and Yunzi Zhang. Chained structure of directed graphs with applications to social and transportation networks. *Applied Network Science*, 7(1), 2022.
 - Gabriele Corso, Luca Cavalleri, Dominique Beaini, Pietro Liò, and Petar Veličković. Principal neighbourhood aggregation for graph nets. In *Advances in Neural Information Processing Systems* (NeurIPS), 2020.
 - Nicola De Cao and Thomas Kipf. MolGAN: An implicit generative model for small molecular graphs. In *International Conference on Machine Learning (ICML)*, 2018.
 - Derek J. de Solla Price. Networks of Scientific Papers. Science, 149(3683):510–515, 1965.
 - Vijay Prakash Dwivedi and Xavier Bresson. A generalization of transformer networks to graphs. In *AAAI Conference on Artificial Intelligence (AAAI)*, 2021.
 - Floor Eijkelboom, Grigory Bartosh, Christian Andersson Naesseth, Max Welling, and Jan-Willem van de Meent. Variational Flow Matching for Graph Generation. In *Advances in Neural Information Processing Systems (NeurIPS)*, 2024.
 - Thomas Elsken, Jan Hendrik Metzen, and Frank Hutter. Neural architecture search: A survey. *Journal of Machine Learning Research (JMLR)*, 20(55):1–21, 2019.
 - Paul Erdös and Alfred Rényi. On random graphs I. Publ. math. debrecen, 6(290-297):18, 1959.
 - Itai Gat, Tal Remez, Neta Shaul, Felix Kreuk, Ricky T. Q. Chen, Gabriel Synnaeve, Yossi Adi, and Yaron Lipman. Discrete flow matching. In *Advances in Neural Information Processing Systems* (*NeurIPS*), 2024.
 - Simon Geisler, Yujia Li, Daniel J Mankowitz, Ali Taylan Cemgil, Stephan Günnemann, and Cosmin Paduraru. Transformers meet directed graphs. In *International Conference on Machine Learning (ICML)*, 2023.
 - Kilian Konstantin Haefeli, Karolis Martinkus, Nathanael Perraudin, and Roger Wattenhofer. Diffusion models for graphs benefit from discrete state spaces. In *Advances in Neural Information Processing Systems (NeurIPS)*, 2022.
 - Frank Harary and Edgar M. Palmer. Graphical Enumeration. Academic Press, 1973.
 - Leonhard Held and Daniel Sabanés Bové. *Applied Statistical Inference: Likelihood and Bayes*. Springer Publishing Company, Incorporated, 2013. ISBN 3642378862.
 - Jonathan Ho and Tim Salimans. Classifier-free diffusion guidance. *arXiv preprint arXiv:2207.12598*, 2022.
 - Jonathan Ho, Ajay Jain, and Pieter Abbeel. Denoising Diffusion Probabilistic Models. In *Advances in Neural Information Processing Systems (NeurIPS)*, 2020.
 - Paul W. Holland, Kathryn Blackmond Laskey, and Samuel Leinhardt. Stochastic blockmodels: First steps. *Social Networks*, 5(2):109–137, 1983.
 - Yinan Huang, Haoyu Wang, and Pan Li. What Are Good Positional Encodings for Directed Graphs? In *International Conference on Learning Representations (ICLR)*, 2025.

- Yunhui Jang, Dongwoo Kim, and Sungsoo Ahn. Graph Generation with K^2 -trees. In *International Conference on Learning Representations (ICLR)*, 2024.
 - Wengong Jin, Regina Barzilay, and Tommi Jaakkola. Junction tree variational autoencoder for molecular graph generation. In *International Conference on Machine Learning (ICML)*, 2018.
 - Jaehyeong Jo, Seul Lee, and Sung Ju Hwang. Score-based generative modeling of graphs via the system of stochastic differential equations. In *International Conference on Machine Learning (ICML)*, 2022.
 - Jaehyeong Jo, Dongki Kim, and Sung Ju Hwang. Graph Generation with Diffusion Mixture. In *International Conference on Machine Learning (ICML)*, 2024.
 - Justin Johnson, Agrim Gupta, and Li Fei-Fei. Image generation from scene graphs. In *IEEE Conference on Computer Vision and Pattern Recognition (CVPR)*, 2018.
 - Madhawa Kaushalya, Ishiguro Katushiko, Nakago Kosuke, and Abe Motoki. GraphNVP: An Invertible Flow Model for Generating Molecular Graphs. *arXiv preprint arXiv:1905.11600*, 2019.
 - Thomas N. Kipf and Max Welling. Variational Graph Auto-Encoders. In *Advances in Neural Information Processing Systems (NeurIPS)*, 2016.
 - Igor Krawczuk, Pedro Abranches, Andreas Loukas, and Volkan Cevher. GG-GAN: A Geometric Graph Generative Adversarial Network. *OpenReview*, 2021.
 - Ranjay Krishna, Yuke Zhu, Oliver Groth, Justin Johnson, Kenji Hata, Joshua Kravitz, Stephanie Chen, Yannis Kalantidis, Li-Jia Li, David A Shamma, et al. Visual genome: Connecting language and vision using crowdsourced dense image annotations. *International Journal of Computer Vision*, 123:32–73, 2017.
 - Marc T. Law, Karsten Kreis, and Haggai Maron. Directed Graph Generation with Heat Kernels. *Transactions on Machine Learning Research (TMLR)*, 2025.
 - Chun Li, Nannan Tang, and Jun Wang. Directed graphs of DNA sequences and their numerical characterization. *Journal of Theoretical Biology*, 241(2):173–177, 2006.
 - Hongsheng Li, Guangming Zhu, Liang Zhang, Youliang Jiang, Yixuan Dang, Haoran Hou, Peiyi Shen, Xia Zhao, Syed Afaq Ali Shah, and Mohammed Bennamoun. Scene Graph Generation: A Comprehensive Survey. *Neurocomputing*, 556, 2024.
 - Muchen Li, Jeffrey Yunfan Liu, Leonid Sigal, and Renjie Liao. GraphPNAS: learning distribution of good neural architectures via deep graph generative models. *arXiv preprint arXiv:2211.15155*, 2022.
 - Mufei Li, Viraj Shitole, Eli Chien, Changhai Man, Zhaodong Wang, Srinivas Sridharan, Ying Zhang, Tushar Krishna, and Pan Li. LayerDAG: A Layerwise Autoregressive Diffusion Model for Directed Acyclic Graph Generation. In *International Conference on Learning Representations (ICLR)*, 2025.
 - Xujia Li, Yuan Li, Xueying Mo, Hebing Xiao, Yanyan Shen, and Lei Chen. Diga: Guided Diffusion Model for Graph Recovery in Anti-Money Laundering. In *International Conference on Knowledge Discovery and Data Mining (KDD)*, 2023.
 - Renjie Liao, Yujia Li, Yang Song, Shenlong Wang, Charlie Nash, William L. Hamilton, David Duvenaud, Raquel Urtasun, and Richard Zemel. Efficient Graph Generation with Graph Recurrent Attention Networks. In *Advances in Neural Information Processing Systems (NeurIPS)*, 2019.
 - Phillip Lippe and Efstratios Gavves. Categorical Normalizing Flows via Continuous Transformations. In *International Conference on Learning Representations (ICLR)*, 2021.
 - Julian Lorenz, Robin Schon, Katja Ludwig, and Rainer Lienhart. A Review and Efficient Implementation of Scene Graph Generation Metrics. *IEEE Conference on Computer Vision and Pattern Recognition Workshops*, 2024.

- Shitong Luo, Chence Shi, Minkai Xu, and Jian Tang. Predicting molecular conformation via dynamic graph score matching. In *Advances in Neural Information Processing Systems (NeurIPS)*, 2021a.
 - Youzhi Luo, Keqiang Yan, and Shuiwang Ji. GraphDF: A Discrete Flow Model for Molecular Graph Generation. In *International Conference on Machine Learning (ICML)*, Proceedings of Machine Learning Research, 2021b.
 - Changsheng Ma and Xiangliang Zhang. GF-VAE: A Flow-based Variational Autoencoder for Molecule Generation. ACM International Conference on Information & Knowledge Management, 2021.
 - Manuel Madeira, Clement Vignac, Dorina Thanou, and Pascal Frossard. Generative Modelling of Structurally Constrained Graphs. In *Advances in Neural Information Processing Systems* (NeurIPS), 2024.
 - Karolis Martinkus, Andreas Loukas, Nathanaël Perraudin, and Roger Wattenhofer. SPECTRE: Spectral Conditioning Helps to Overcome the Expressivity Limits of One-shot Graph Generators. In *International Conference on Machine Learning (ICML)*, Proceedings of Machine Learning Research, 2022.
 - Rocío Mercado, Tobias Rastemo, Edvard Lindelöf, Günter Klambauer, Ola Engkvist, Hongming Chen, and Esben Jannik Bjerrum. Graph Networks for Molecular Design. *Machine Learning: Science and Technology*, 2020.
 - Christopher Morris, Martin Ritzert, Matthias Fey, William L. Hamilton, Jan Eric Lenssen, Gaurav Rattan, and Martin Grohe. Weisfeiler and Leman Go Neural: Higher-order Graph Neural Networks. In *AAAI Conference on Artificial Intelligence (AAAI)*, 2019.
 - Alexander Quinn Nichol and Prafulla Dhariwal. Improved denoising diffusion probabilistic models. In *International Conference on Machine Learning (ICML)*, 2021.
 - Giannis Nikolentzos, Michalis Vazirgiannis, Christos Xypolopoulos, Markus Lingman, and Erik G. Brandt. Synthetic electronic health records generated with variational graph autoencoders. *Digital Medicine*, 6(1):83, 2023.
 - Chenhao Niu, Yang Song, Jiaming Song, Shengjia Zhao, Aditya Grover, and Stefano Ermon. Permutation invariant graph generation via score-based generative modeling. In *International Conference on Artificial Intelligence and Statistics (AISTATS)*, 2020.
 - Tiago P. Peixoto. Efficient Monte Carlo and greedy heuristic for the inference of stochastic block models. *Physical Review E*, 89(1), 2014.
 - Ethan Perez, Florian Strub, Harm De Vries, Vincent Dumoulin, and Aaron Courville. FiLM: Visual reasoning with a general conditioning layer. In *AAAI Conference on Artificial Intelligence (AAAI)*, 2018.
 - Phitchaya Mangpo Phothilimthana, Sami Abu-El-Haija, Kaidi Cao, Bahare Fatemi, Michael Burrows, Charith Mendis, and Bryan Perozzi. TpuGraphs: A Performance Prediction Dataset on Large Tensor Computational Graphs. In *Advances in Neural Information Processing Systems (NeurIPS)*, 2023.
 - Yiming Qin, Manuel Madeira, Dorina Thanou, and Pascal Frossard. DeFoG: Discrete Flow Matching for Graph Generation. In *International Conference on Machine Learning (ICML)*, 2025a.
 - Yiming Qin, Clement Vignac, and Pascal Frossard. SparseDiff: Sparse Discrete Diffusion for Scalable Graph Generation. *Transactions on Machine Learning Research (TMLR)*, 2025b.
 - Ladislav Rampášek, Michael Galkin, Vijay Prakash Dwivedi, Anh Tuan Luu, Guy Wolf, and Dominique Beaini. Recipe for a general, powerful, scalable graph transformer. In *Advances in Neural Information Processing Systems (NeurIPS)*, 2022.
 - Ivan Rodin, Antonino Furnari, Kyle Min, Subarna Tripathi, and Giovanni Maria Farinella. Action Scene Graphs for Long-Form Understanding of Egocentric Videos. In *IEEE Conference on Computer Vision and Pattern Recognition (CVPR)*, 2023.

- Christoph Schweimer, Christine Gfrerer, Florian Lugstein, David Pape, Jan A Velimsky, Robert Elsässer, and Bernhard C Geiger. Generating simple directed social network graphs for information spreading. *ACM Web Conference* 2022, 2022.
 - Kartik Sharma, Srijan Kumar, and Rakshit S Trivedi. Diffuse, sample, project: plug-and-play controllable graph generation. In *International Conference on Machine Learning (ICML)*, 2024.
 - Martin Simonovsky and Nikos Komodakis. GraphVAE: Towards Generation of Small Graphs Using Variational Autoencoders. In *Artificial Neural Networks and Machine Learning (ICANN)*. Springer International Publishing, 2018.
 - Antoine Siraudin, Fragkiskos D Malliaros, and Christopher Morris. Cometh: A continuous-time discrete-state graph diffusion model. *arXiv preprint arXiv:2406.06449*, 2024.
 - Jascha Sohl-Dickstein, Eric Weiss, Niru Maheswaranathan, and Surya Ganguli. Deep unsupervised learning using nonequilibrium thermodynamics. In *International Conference on Machine Learning (ICML)*, 2015.
 - Yang Song and Stefano Ermon. Generative modeling by estimating gradients of the data distribution. In *Advances in Neural Information Processing Systems (NeurIPS)*, 2019.
 - Yang Song, Jascha Sohl-Dickstein, Diederik P Kingma, Abhishek Kumar, Stefano Ermon, and Ben Poole. Score-based generative modeling through stochastic differential equations. In *International Conference on Learning Representations (ICLR)*, 2021.
 - Henan Sun, Xunkai Li, Daohan Su, Junyi Han, Rong-Hua Li, and Guoren Wang. Towards Data-centric Machine Learning on Directed Graphs: a Survey. *arXiv preprint arXiv:2412.01849*, 2024.
 - Martha Takane, Saúl Bernal-González, Jesús Mauro-Moreno, Gustavo García-López, Bruno Méndez-Ambrosio, and Francisco F De-Miguel. Directed Graph Theory for the Analysis of Biological Regulatory Networks. *biorXiv preprint biorXiv:2023.10.02.560622*, 2023.
 - Rylee Thompson, Boris Knyazev, Elahe Ghalebi, Jungtaek Kim, and Graham W. Taylor. On Evaluation Metrics for Graph Generative Models. In *International Conference on Learning Representations (ICLR)*, 2022.
 - Jui-Yi Tsai, Ya-Wen Teng, Ho Chiok Yew, De-Nian Yang, and Lydia Y. Chen. CDGraph: Dual Conditional Social Graph Synthesizing via Diffusion Model. *arXiv preprint arXiv:2311.01729*, 2023.
 - Clement Vignac and Pascal Frossard. Top-N: Equivariant Set and Graph Generation without Exchangeability. In *International Conference on Learning Representations (ICLR)*, 2022.
 - Clement Vignac, Igor Krawczuk, Antoine Siraudin, Bohan Wang, Volkan Cevher, and Pascal Frossard. DiGress: Discrete Denoising diffusion for graph generation. In *International Conference on Learning Representations (ICLR)*, 2023a.
 - Clement Vignac, Nagham Osman, Laura Toni, and Pascal Frossard. MiDi: Mixed Graph and 3D Denoising Diffusion for Molecule Generation. *European Conference on Machine Learning*, 2023b.
 - Qitong Wang, Georgios Kollias, Vasileios Kalantzis, Naoki Abe, and Mohammed J Zaki. Directed Graph Transformers. *Transactions on Machine Learning Research (TMLR)*, 2024.
- Antoine Wehenkel and Gilles Louppe. Graphical Normalizing Flows . In *International Conference on Artificial Intelligence and Statistics (AISTATS)*, 2021.
- Pi-Jing Wei, Ziqiang Guo, Zhen Gao, Zheng Ding, Rui-Fen Cao, Yansen Su, and Chun-Hou Zheng. Inference of gene regulatory networks based on directed graph convolutional networks. *Briefings in Bioinformatics*, 25(4), 2024.
- Keyulu Xu, Weihua Hu, Jure Leskovec, and Stefanie Jegelka. How Powerful are Graph Neural Networks? In *International Conference on Learning Representations (ICLR)*, 2019.

- Minkai Xu, Lantao Yu, Yang Song, Chence Shi, Stefano Ermon, and Jian Tang. Geodiff: A geometric diffusion model for molecular conformation generation. In *International Conference on Learning Representations (ICLR)*, 2022.
- Zhe Xu, Ruizhong Qiu, Yuzhong Chen, Huiyuan Chen, Xiran Fan, Menghai Pan, Zhichen Zeng, Mahashweta Das, and Hanghang Tong. Discrete-state Continuous-time Diffusion for Graph Generation. In *Advances in Neural Information Processing Systems (NeurIPS)*, 2024.
- Ling Yang, Zhilin Huang, Yang Song, Shenda Hong, Guohao Li, Wentao Zhang, Bin Cui, Bernard Ghanem, and Ming-Hsuan Yang. Diffusion-based scene graph to image generation with masked contrastive pre-training. *arXiv* preprint arXiv:2211.11138, 2022.
- Ling Yang, Zhilin Huang, Zhilong Zhang, Zhongyi Liu, Shenda Hong, Wentao Zhang, Wenming Yang, Bin Cui, and Luxia Zhang. Graphusion: Latent Diffusion for Graph Generation. *IEEE Transactions on Knowledge and Data Engineering*, 2024.
- Jiaxuan You, Rex Ying, Xiang Ren, William L. Hamilton, and Jure Leskovec. GraphRNN: Generating Realistic Graphs with Deep Auto-regressive Models. In *International Conference on Machine Learning (ICML)*, Proceedings of Machine Learning Research, 2018.
- Muhan Zhang, Shali Jiang, Zhicheng Cui, Roman Garnett, and Yixin Chen. D-VAE: A Variational Autoencoder for Directed Acyclic Graphs. In *Advances in Neural Information Processing Systems* (*NeurIPS*), 2019.
- Lingxiao Zhao, Xueying Ding, and Leman Akoglu. Pard: Permutation-Invariant Autoregressive Diffusion for Graph Generation. In *Advances in Neural Information Processing Systems (NeurIPS)*, 2024.

Appendix

 Table of Contents

A I	Dual Attention	1
ВЕ	Positional Encodings	1
C S	Sampling Optimization in DIRECTO	2
D I	DIRECTO Training and Sampling Algorithms	2
E I	Dataset descriptions	2
F	E.1 Synthetic datasets	2
F	E.2 TPU Tiles	2
F	E.3 Visual Genome	2
F I	Further details on evaluation metrics	2
F	F.1 Validity metrics	2
F	F.2 Uniqueness and novelty	2
F	3.3 Maximum Mean Discrepancy metrics	2
F	F.4 Joint node-edge distributional metrics	2
F	7.5 Downstream tasks metrics	2
G I	Experimental details	2
(G.1 Details on baselines	2
(G.2 Training setup	2
(G.3 Resources and runtime	2
H A	Additional results	2
ŀ	H.1 Extended results for synthetic datasets	2
F	H.2 Extended results for real-world datasets	3
F	H.3 The role of dual attention	3
ŀ	H.4 The role of positional encodings	3
F	H.5 ER vs DAG performance	3
F	H.6 Scalability experiments	3
ŀ	H.7 Conditional generation	3
I	H.8 Impact of sampling optimization using discrete flow matching	3
I I	terative Refinement Methods for Graph Generation	3
I	.1 Graph iterative refinement methods	3
I	.2 Discrete flow matching for graph generation	3
I	.3 Discrete diffusion for graph generation	3
JU	Use of Large Language Models	4
K V	Visualizations	4
	Limitations and future work	4

A DUAL ATTENTION

In this section, we provide a detailed description of the dual attention mechanism used in our model, which effectively integrates both target-to-source and source-to-target information to enhance the graph generation process.

We start with the stacked tensors of node $X \in \mathbb{R}^{B \times N \times d_x}$, edge $E \in \mathbb{R}^{B \times N \times N \times d_e}$ and global $y \in \mathbb{R}^{B \times d_y}$ features, where B is the batch size, N is the number of nodes of the biggest graph in the batch, and d_x , d_e , and d_y are the node, edge, and global feature dimensions respectively. To handle different node sizes in a batch, we use a binary node mask $M \in \{0,1\}^{B \times N \times 1}$ that accounts for the presence of nodes in each graph.

First, we begin by projecting the queries, keys, and values for the source and the target directions. These are then projected and reshaped into n_h heads of dimension $d_q = d_x/n_h$, thus obtaining for each node:

$$Q_{\mathrm{S}} = \mathrm{reshape}(M \odot W_{\mathrm{O}}^{\mathrm{S}} X), \quad K_{\mathrm{S}} = \mathrm{reshape}(M \odot W_{\mathrm{K}}^{\mathrm{S}} X), \quad V_{\mathrm{S}} = \mathrm{reshape}(M \odot W_{\mathrm{V}}^{\mathrm{S}} X), \quad (10)$$

$$Q_{\mathrm{T}} = \mathrm{reshape}(M \odot W_{\mathrm{O}}^{\mathrm{T}} X), \quad K_{\mathrm{T}} = \mathrm{reshape}(M \odot W_{\mathrm{K}}^{\mathrm{T}} X), \quad V_{\mathrm{T}} = \mathrm{reshape}(M \odot W_{\mathrm{V}}^{\mathrm{T}} X), \quad (11)$$

where $W_Q^S, W_K^S, W_V^S, W_Q^T, W_K^T, W_V^T$ are the learned linear projections. The final shape of each of the elements after the reshaping is $B \times N \times n_h \times d_g$.

Then we compute the dual attention, both from source to target and from target to source:

$$\mathbf{Y}_{ST}[i,j] = \frac{\mathbf{Q}_{S}[i] \cdot \mathbf{K}_{T}[j]}{\sqrt{d_q}}, \quad \mathbf{Y}_{TS}[i,j] = \frac{\mathbf{Q}_{T}[i] \cdot \mathbf{K}_{S}[j]}{\sqrt{d_q}}.$$
 (12)

with i, j the index nodes and each $\boldsymbol{Y} \in \mathbb{R}^{B \times N \times N \times n_h \times d_q}$.

To incorporate edge features into the attention mechanism, we apply FiLM-style modulation (Perez et al., 2018) using additive and multiplicative projections W_{mul} , W_{add} :

$$E_{\text{mul}}^{\text{S}} = \text{reshape}(W_{\text{mul}}^{\text{S}}(E)), \qquad E_{\text{add}}^{\text{S}} = \text{reshape}(W_{\text{add}}^{\text{S}}(E)), \qquad (13)$$

$$\boldsymbol{E}_{\text{nul}}^{\text{T}} = \text{reshape}(\boldsymbol{W}_{\text{nul}}^{\text{T}}(\boldsymbol{E}^{\top})), \qquad \boldsymbol{E}_{\text{add}}^{\text{T}} = \text{reshape}(\boldsymbol{W}_{\text{add}}^{\text{T}}(\boldsymbol{E}^{\top})), \qquad (14)$$

where we reshape the edge features to $E \in \mathbb{R}^{B \times N \times N \times n_h \times d_q}$. This is done so that they can be added or multiplied to the attention scores Y_{ST} and Y_{TS} to modify them:

$$Y_{\text{ST}} \leftarrow Y_{\text{ST}} \cdot (E_{\text{mul}}^{\text{S}} + 1) + E_{\text{add}}^{\text{S}},$$
 (15)

$$Y_{\text{TS}} \leftarrow Y_{\text{TS}} \cdot (E_{\text{mul}}^{\text{T}} + 1) + E_{\text{add}}^{\text{T}}.$$
 (16)

Edge Feature Update To get the final update of the edge features, the attention-weighted edge representations are flattened and modulated by global features y using FiLM with additive and multiplicative projections $W_{\rm add}^E$ and $W_{\rm mul}^E$:

$$E' = W_{\text{add}}^{y}(y) + (W_{\text{mul}}^{y}(y) + 1) \odot \text{flatten}(Y_{\text{ST}}), \tag{17}$$

where we flatten over the last dimension. We use Y_{ST} as it captures the directional flow from source to target, avoiding ambiguity in the directional influence, and still effectively encoding the influence of source nodes on their targets. Then, the result is followed by an output projection and a residual connection

$$E' = W_{\text{out}}^E(E'), \quad E' \leftarrow E + E',$$
 (18)

resulting in the updated $E' \in \mathbb{R}^{B \times N \times N \times d_e}$.

Node Feature Update To perform the node feature update, first we concatenate the dual attention scores and apply softmax:

$$\mathbf{A}_{\text{aggr}} = \operatorname{softmax}\left(\operatorname{concat}(\mathbf{Y}_{\text{ST}}, \mathbf{Y}_{\text{TS}})\right) \in \mathbb{R}^{B \times N \times 2N \times n_h \times d_e},$$
 (19)

$$V_{\text{aggr}} = \text{concat}(V_{\text{T}}, V_{\text{T}}) \in \mathbb{R}^{B \times 2N \times n_h \times d_x},$$
 (20)

with concat() being the concatenation over the third dimension for A_{aggr} and over the second dimension for V_{aggr} .

After this, the unified weights are aggregated through weighted summation and the result flattened over the second dimension to produce:

$$X_{\text{aggr}} = \text{attn}_{\text{aggr}} V_{\text{aggr}} \in \mathbb{R}^{B \times N \times n_h \times d_x}.$$
 (21)

We then FiLM-modulate the attended features with the global vector y with additive and multiplicative projections W_{add}^X and W_{mul}^X to produce:

$$\boldsymbol{X}_{\text{mod}} = \boldsymbol{W}_{\text{add}}^{X}(\boldsymbol{y}) + (\boldsymbol{W}_{\text{mul}}^{X}(\boldsymbol{y}) + 1) \odot \boldsymbol{X}_{\text{aggr}}, \tag{22}$$

To allow the model to adaptively balance between preserving the original node features and incorporating the updated ones, we introduce a learnable gating mechanism $gX \in [0,1]$:

$$g_X = \sigma(W_{\text{gate}}^X \odot \text{concat}(X, V_{\text{aggr}})),$$
 (23)

followed by a gated residual connection:

$$X' = (1 + g_X) \odot X + (1 - g_X) \odot X_{\text{mod}}, \tag{24}$$

where the weights assigned to X and X_{mod} sum up to 2, ensuring that the overall magnitude remains consistent with the ungated case.

Finally, the result is followed by an output projection:

$$X' = W_{\text{out}}^X(X'), \tag{25}$$

resulting in the updated $X' \in \mathbb{R}^{B \times N \times d_x}$.

Global Features Update The updated global vector is computed by aggregating from the node X and edge E projections:

$$y' = y + W_y(y) + X_{\rightarrow y}(X) + E_{\rightarrow y}(E), \tag{26}$$

where $X_{\to y}$ and $E_{\to y}$ are PNA layers (Corso et al., 2020) that given node features $\boldsymbol{X} \in \mathbb{R}^{B \times N \times d_x}$ or edge features $\boldsymbol{E} \in \mathbb{R}^{B \times N \times N \times d_e}$ and a learnable weight matrix \boldsymbol{W}_{PNA} , computes

$$PNA(\boldsymbol{X}) = concat(\max(\boldsymbol{X}), \min(\boldsymbol{X}), \max(\boldsymbol{X}), \operatorname{std}(\boldsymbol{X})) \, \boldsymbol{W}_{PNA} \in \mathbb{R}^{4d_x}, \tag{27}$$

$$PNA(\mathbf{E}) = concat(max(\mathbf{E}), min(\mathbf{E}), mean(\mathbf{E}), std(\mathbf{E})) \mathbf{W}_{PNA} \in \mathbb{R}^{4d_e},$$
(28)

where the different operations are performed over the features and then concatenation is performed along the feature dimension. Both results then pass through a linear layer resulting in $X_{\to y}(X), E_{\to y}(E) \in \mathbb{R}^{d_y}$.

Once again, we use an output projection

$$\mathbf{y'} = \mathbf{W}_{\text{out}}^{y}(\mathbf{y'}),\tag{29}$$

which results in the updated global features $\boldsymbol{y'} \in \mathbb{R}^{B \times d_y}$.

This dual attention block is applied L times within the graph transformer.

B Positional Encodings

To effectively capture the structural properties of directed graphs, we explore a range of positional encodings (PEs) that can be incorporated into the transformer architecture. These encodings provide nodes with a sense of position and orientation within the digraph, enabling the model to better reason about directionality. Below, we detail the specific PEs evaluated in our work.

Laplacian (Lap) Traditionally in the undirected case, the eigenvectors of the combinatorial Laplacian are widely used to encode graph structure, relying on the spectral decomposition $L = \Gamma \Lambda \Gamma^{-1}$ where L is the combinatorial Laplacian, Λ is the diagonal matrix of eigenvalues, and Γ is the matrix of eigenvectors. The unnormalized and normalized Laplacians are defined as

$$L_U = D - A_s, \quad L_N = I - D^{-1/2} A_s D^{-1/2},$$
 (30)

where A_s is the adjacency matrix (symmetrized when working with digraphs) and D is the degree matrix. However, when dealing with directed graphs, this symmetrization discards directionality information, as it enforces $A_s =_s^\top$, but it is necessary to guarantee that L_U and L_N are symmetric and positive semi-definite.

Magnetic Laplacian (MagLap) To retain directional information while preserving desirable spectral properties, Geisler et al. (2023) propose the *Magnetic Laplacian*, which introduces a complex-valued phase encoding into the adjacency matrix. Specifically, the (unnormalized and normalized) Magnetic Laplacians are given by:

$$\boldsymbol{L}_{\text{dir},U}^{(q)} = \boldsymbol{D} - (\boldsymbol{A}_s \odot \exp(i\Theta^{(q)})), \quad \boldsymbol{L}_{\text{dir},N}^{(q)} = \boldsymbol{I} - \left((\boldsymbol{D}^{-1/2} \boldsymbol{A}_s \boldsymbol{D}^{-1/2}) \odot \exp(i\Theta^{(q)}) \right), \quad (31)$$

where \odot denotes the element-wise (Hadamard) product, i is the imaginary unit, and the phase matrix $\Theta^{(q)}$ is defined as:

$$\Theta_{u,v}^{(q)} = 2\pi q (\mathbf{A}_{u,v} - \mathbf{A}_{v,u}). \tag{32}$$

The potential parameter $q \geq 0$ controls the strength of the phase shift. For q=0, the Magnetic Laplacian reduces to the classical combinatorial Laplacian. The resulting complex-valued eigenvectors can effectively encode directionality patterns in the graph. We leverage the information by concatenating the real and complex parts of the eigenvectors to the node features, and the eigenvalues to the global graph features.

Multi-q **Magnetic Laplacian** Recently, Huang et al. (2025) extends the Magnetic Laplacian by introducing a multi-q formulation, which considers as positional encoding stacking together the eigenvalues and eigenvectors of Q distinct Magnetic Laplacians with potentials q_1, \ldots, q_Q . This approach enables the recovery of the bidirectional walk profile, a generalization of walk counting in undirected graphs that captures a broader range of directional relationships.

By incorporating information from multiple potentials, the multi-q formulation enhances the representational power for directed structures. In particular, they show that the method is robust to the chosen potentials q chosen. In our model, we leverage this information by concatenating the first k eigenvectors (real and imaginary parts) of each of the Q magnetic Laplacians to the global features, and the corresponding first k eigenvalues to the node features, providing direction-aware structural signals to both levels of representation. As a drawback, this positional encoding results in higher computational costs, as it is necessary to compute several eigenvalue decompositions and, in addition, results in a higher dimensional positional encoding to be processed by the denoising network.

Directed Relative Random Walk Probabilities (RRWP) For undirected graphs, RRWP encodes the likelihood of arriving from one node to another through k-step random walks. This is usually expressed via a transition matrix T^k , with $T = AD^{-1}$, that encodes the transition probabilities.

For directed graphs, it is possible to consider $T = AD_{out}^{-1}$, where we take into account the degree matrix of the outgoing edges D_{out}^{-1} (Geisler et al., 2023). The K-step transition probabilities are then captured by powers of T, producing the sequence $[I, T, T^2, \dots, T^{K-1}]$.

Additionally, in the directed setting, Geisler et al. (2023) suggest it is also informative to model reverse random walks, starting from incoming edges. For this, we can define the reverse transition matrix $\mathbf{R} = \mathbf{A}^{\top} \mathbf{D}_{\text{in}}^{-1}$, where \mathbf{D}_{in} is the in-degree matrix. This would represent the likelihood of arriving at a given edge starting from another through k-step random walks. Analogously, we compute $[\mathbf{I}, \mathbf{R}, \mathbf{R}^2, \dots, \mathbf{R}^{K-1}]$.

To have our final positional encoding, following Geisler et al. (2023), we ensure that graphs are not nilpotent and that the probabilities encoded in the matrices sum up to 1 by adding self-loops to sink nodes during pre-processing. Finally, the full positional encoding concatenates both forward and reverse walk features for a pre-defined K, yielding:

$$RRPW(G) = [I, T, T^{2}, \dots, T^{K-1}, I, R, R^{2}, \dots, R^{K-1}].$$
(33)

We concatenate the PE to the edge features, and additionally concatenate the diagonal elements of each matrix to the node features to further infuse them with the information.

Additionally, to mitigate that for large k the probabilities tend to converge to sink nodes, we optionally incorporate $Personalized\ PageRank\ (PPR)$ features. The PPR matrix is defined in closed form as:

$$PPR = p_r (I - (1 - p_r)T)^{-1}, (34)$$

where p_r denotes the restart probability.

C SAMPLING OPTIMIZATION IN DIRECTO

The decoupling of training and sampling in discrete flow matching enables principled, training-free modifications to the sampling procedure, offering a flexible design space to enhance generation quality across digraph distributions (Qin et al., 2025a). In this section, we detail the three core parameters that govern sampling behavior: (i) time distortion functions, (ii) target guidance intensity, and (iii) stochasticity strength. Each plays a distinct role in shaping the denoising trajectory and contributes to different aspects of generation quality and structural fidelity.

Time Distortion Functions A central part for sampling optimization lies in the application of *time distortion functions*. These functions transform the time variable $t \in [0, 1]$ through a bijective, monotonic mapping f(t), yielding a distorted time variable t' = f(t). While used in both training and sampling, their objectives differ. In training, time distortions skew the sampling distribution over time, concentrating the model's learning capacity on specific denoising intervals. In sampling, they induce variable step sizes along the denoising trajectory, with finer resolution where structural sensitivity is highest (e.g., late-stage edits near t = 1).

Formally, the probability density function (PDF) of the transformed time variable t' is:

$$\phi_{t'}(t') = \phi_t(t) \left| \frac{d}{dt'} f^{-1}(t') \right|, \text{ where } \phi_t(t) = 1 \text{ for } t \in [0, 1].$$
 (35)

We consider the same five representative time distortion functions from Qin et al. (2025a) that yield diverse distributions for t':

- **Identity**: f(t) = t Uniform time density, baseline behavior.
- Polydec: $f(t) = 2t t^2$ Increasing density over time, emphasizing late-stage denoising.
- Cos: $f(t) = \frac{1-\cos(\pi t)}{2}$ Concentrates density at both boundaries.
- Revcos: $f(t) = 2t \frac{1-\cos(\pi t)}{2}$ Peaks at intermediate times.
- **Polyinc**: $f(t) = t^2$ Decreasing density over time, emphasizes early steps.

In the sampling phase, the induced variable step sizes, particularly from functions like *polydec*, allow for finer resolution near the clean data, where structural coherence is most fragile. Empirically, these functions are selected based on dataset-specific properties to improve fidelity and structural constraints without need for retraining.

Target Guidance Another axis for improving sampling efficiency is the modification of the *conditional rate matrix* R_t to better guide the generation trajectory toward the clean target graph z_1 . This is achieved by incorporating an additive guidance term:

$$R_t(z_t, z_{t+\Delta t} \mid z_1) = R_t^*(z_t, z_{t+\Delta t} \mid z_1) + \omega \cdot \frac{\delta(z_{t+\Delta t}, z_1)}{\mathcal{Z}_t^{>0} \cdot p_{t|1}(z_t \mid z_1)}.$$
 (36)

Here, $\omega \in \mathbb{R}_+$ controls the strength of the guidance, $\mathcal{Z}_t^{>0}$ is a discrete variable with Z possible positive values, and $\delta(\cdot,\cdot)$ is the Kronecker delta. Intuitively, this formulation prioritizes transitions that directly align with the clean graph.

Stochasticity Control The final sampling-time parameter is the *stochasticity coefficient* η . This parameter scales an auxiliary rate matrix R_t^{DB} that satisfies the detailed balance condition (Campbell et al., 2024) and adds it to the optimal rate matrix R_t^* :

$$R_t^{\eta} = R_t^* + \eta \cdot R_t^{\text{DB}}. \tag{37}$$

The role of η is to regulate trajectory stochasticity: higher values promote broader exploration during denoising, potentially correcting suboptimal states. Setting $\eta=0$ recovers the deterministic path prescribed by R_t^* , minimizing the expected number of transitions.

Sampling Optimization Together, these sampling parameters constitute a flexible, principled toolkit for tailoring the sampling procedure to diverse graph domains and structural requirements. In our case, we optimize these parameters at sampling time to improve the performance of DIRECTO. In particular, we individually optimize each of them for the main results, and perform the final sampling using the best performing parameters in terms of V.U.N (a detailed description is available in Appendix G.2). and ratio performance. A study of the effect of these parameters on sampling performance can be found in H.8.

D DIRECTO TRAINING AND SAMPLING ALGORITHMS

This appendix provides detailed pseudocode for the training and sampling procedures used in the DIRECTO framework. Alg. 1 outlines the training loop, where a digraph is progressively noised and a denoising model is optimized to reconstruct the original graph.

We consider the original data distribution p_1 as well as the time distribution \mathcal{T} which in our case is set to be the uniform distribution. In addition, f^{θ} refers to the denoising network, in our case the graph transformer with dual attention.

Algorithm 1 DIRECTO Training

1080

1082

1084

1086 1087 1088

1089 1090 1091

1092

1093 1094

1095

1099

1100

1101

1102

1103

1104

1105

1106

1107

1108 1109 1110

1111

1112 1113

1114 1115

1116 1117

1118

1119

1120

1121

1122

1123

1124

1125

1126

1131 1132

1133

```
1: Input: Graph dataset \{G^1, \ldots, G^M\} \sim \boldsymbol{p}_1
2: while f_{\theta} not converged do
3:
          Sample G \sim \boldsymbol{p}_1
4:
          Sample t \sim \mathcal{T}
5:
          Iteratively sample G_t \sim \boldsymbol{p}_{t|1}(G_t|G)
                                                                                                                               ▶ Noising process
6:
          h \leftarrow \operatorname{PosEnc}(G_t)
                                                                                                                         ▶ Positional encoding
          \boldsymbol{p}_{1|t}^{\theta}(\cdot|G_t) \leftarrow f_{\theta}(G_t, h, t)
7:
                                                                                         ▷ Denoising prediction with dual attention
          loss \leftarrow \text{CE}_{\lambda}(G, \boldsymbol{p}_{1|t}^{\theta}(\cdot|G_t))
9: end while
```

Alg. 2 describes the generative sampling process in which new digraphs are synthesized by iteratively denoising from an initial random digraph structure. Again, we consider $p_0 = p_{noise}$ the predefined noise distribution, f^{θ} the denoising graph transformer with dual attention, $p_{1|t}^{\theta}$ the denoising predictions, and $p_{t+\Delta t|t}^{\theta}$ as the update rule, see Equation (41).

Algorithm 2 DIRECTO Sampling

```
1: Input: # graphs to sample S
 2: for i = 1 to S do
 3:
          Sample N from train set
                                                                                                                               ⊳ # nodes
 4:
          Sample G_0 \sim \boldsymbol{p}_0(G_0)
          for t=0 to 1-\Delta t with step \Delta t do
 5:
               h \leftarrow \operatorname{PosEnc}(G_t)
\boldsymbol{p}_{1|t}^{\theta}(\cdot|G_t) \leftarrow f_{\theta}(G_t, h, t)
 6:
                                                                                                              ▶ Positional encoding
 7:
                                                                                ▶ Denoising prediction with dual attention
                G_{t+\Delta t} \sim \boldsymbol{p}_{t+\Delta t|t}^{\theta}(G_{t+\Delta t}|G_t)
 8:
                                                                                                                         9:
          end for
10:
          Store G_1 as G^i
11: end for
```

E DATASET DESCRIPTIONS

In this section, we provide further detailed information about the datasets described in Section 4 and used for the experiments in Section 5.

E.1 SYNTHETIC DATASETS

We outline the mathematical formulation of each graph generation strategy used in our experiments. All graphs are generated as adjacency matrices $A \in \{0,1\}^{n \times n}$ (where $A_{ij} = 1$ denotes a directed edge from node i to node j), and preprocessed to adapt to the structure required by the model.

For all datasets, we generate a total of 200 graphs, split as: 128 train, 32 validation, 40 test. A study on the effect of the dataset size on the quality of the generations can be found in Appendix H.6. Furthermore, the dataset statistics can be found in Table 3.

Table 3: Synthetic dataset statistics.

Dataset	Min. nodes	Max. nodes	Avg. nodes	Min. edges	Max. edges	Avg. edges	#Train	#Val	#Test
Erdos-Renyi (ER)	20	80	46	223	3670	1446	128	32	40
SBM	44	175	106	340	3008	1426	128	32	40
ER (DAG)	20	80	49	103	1892	762	128	32	40
Price (DAG)	64	64	64	132	246	197	128	32	40

Erdős-Renyi (**Erdős & Rényi**, 1959) We generate graphs with a variable number of nodes between n=20 and n=80. For a number of nodes n, edges are sampled independently with a fixed probability p=0.6. The adjacency matrix A is generated by:

$$A_{ij} \sim \text{Bernoulli}(p), \quad \forall i \neq j$$

To generate a second dataset of DAGs, we enforce a lower-triangular structure (i.e., edges only from higher-indexed to lower-indexed nodes), which results in graphs generated with a probability p=0.3.

Price's model (de Solla Price, 1965) This is the directed version of the Barabási-Albert or preferential attachment model, which simulates the growth of citation networks. We build DAGs sequentially for a fixed number of nodes N=64. Each new node i forms $m=\log_2(N)$ edges to existing nodes j with probability proportional to their degree:

$$\mathbb{P}(i \to j) \propto \deg(j)$$
.

Since the number of nodes is fixed to N=64, mean out-degree results in m=6. In practice, we implement this "bag" of nodes that replicates existing connections. For each new node i, we sample m destination nodes from the bag. Then, for each selected node j, we set $\boldsymbol{A}_{ij}=1$ and add i and the selected nodes to the bag. This ensures a directed acyclic graph (DAG) due to the order of node addition.

Stochastic Block Model (Holland et al., 1983) We create K communities with sizes $\{n_1, n_2, \ldots, n_K\}$. We set the number of communities between K=2 and K=5, and the number of nodes per community between 20 and 40. The probability of an edge between any two nodes depends on their community assignments

$$A_{ij} \sim \text{Bernoulli}(P_{z_i z_i})$$

where $z_i \in \{1, ..., K\}$ is the block assignment of node i and $P \in [0, 1]^{K \times K}$ is a matrix of intraand inter-community connection probabilities. In particular, we use

$$P_{kk} = p_{\text{intra}} = 0.3, \quad P_{kl} = p_{\text{inter}} = 0.05 \text{ for } k \neq l$$

to generate a block-structured, directed graph.

E.2 TPU TILES

In this dataset introduced by Phothilimthana et al. (2023), each DAG represents a computation within a machine learning workload, such as a training epoch or an inference step. Each of the 6301 datapoints includes a computational graph, a specific compilation configuration, and the execution time of the graph when compiled with that configuration. The dataset features different model architectures, such as ResNets, EfficientNets, Masked R-CNNs, and Transformers, with graphs of up to ~ 400 nodes.

We adopt the processing and splits from Li et al. (2025). Details on dataset statistics for the three different splits can be found in Table 4.

1188 1189

Table 4: TPU Tiles dataset statistics.

	ı	90
1	1	91
1	1	92
1	1	93

1195

1196

1197 1198

1199 1201 1202

1203 1204 1205

1206 1207

1208 1209 1210

1211

1212

1218 1219

1217

1222 1223 1224

1225 1226

1231 1232 1233

1236

1237

1239 1240

1241

Dataset Min. nodes Max. nodes # Graphs Avg. nodes Min. edges Max. edges Avg. edges 5040 2 394 Train 711 43 41 Validation 2 113 41 123 43 630 1 2 154 41 249 44 Test 631

VISUAL GENOME E.3

The Visual Genome dataset (Krishna et al., 2017) aims at bridging computer vision and natural language understanding by providing richly annotated images. It comprises over 100,000 images annotated with object labels, attributes, relationships, which allows to capture the presence of objects but also their attributes and interactions. It has become a standard benchmark for tasks such as scene graph generation, visual question answering, and grounded language understanding.

To build the directed graph dataset, we set 3 types of nodes: objects, attributes, and relationships, with the actual node class being the text label. Then, we link them via directed edges according to the visual rules provided in the original data and taking into account that:

- 1. Objects have outgoing edges to attributes and relationships and incoming edges from relationships.
- 2. **Relationships** have outgoing edges to objects and incoming edges from objects.
- 3. Attributes have no outgoing edges and incoming edges from objects.

Once we built the digraphs, we select a relevant subset from this raw dataset by keeping graphs with 20 to 40 nodes, and with a minimum of 25 edges per graph. Then, for each graph, we only consider objects, attributes, and relationships that are in the top-20 in terms of prevalence in the full dataset, ending with 60 node classes. We randomly split the graphs into 203 train, 52 validation and 63 test graphs, with detailed statistics of each split available in Table 5. The total number of cyclic graph in the dataset is 119 (\sim 37.5% of the digraphs).

Table 5: Visual Genome dataset statistics.

Dataset	Min. nodes	Max. nodes	Avg. nodes	Min. edges	Max. edges	Avg. edges	# Graphs
Global	21	40	34	25	47	28	317
Train	21	40	33	25	47	28	203
Validation	24	40	34	25	40	28	51
Test	21	40	34	25	36	28	63

The selected top-20 objects, relationships, and attributes are:

- Objects: ['window', 'tree', 'man', 'shirt', 'wall', 'person', 'building', 'ground', 'sign', 'light', 'sky', 'head', 'leaf', 'leg', 'hand', 'pole', 'grass', 'hair', 'car', 'cloud']
- Relationships: ['on', 'has', 'in', 'of', 'wearing', 'with', 'behind', 'holding', 'on top of', 'on a', 'near', 'next to', 'has a', 'on', 'under', 'by', 'of a', 'wears', 'above', 'sitting on']
- ['white', 'black', 'blue', 'green', 'red', 'brown', 'yellow', 'small', 'large', 'wooden', 'gray', 'silver', 'metal', 'orange', 'grey', 'tall', 'long', 'dark', 'pink', 'clear']

FURTHER DETAILS ON EVALUATION METRICS

In this section, we detail the statistical procedures used to evaluate the graphs generated by our model. We detail how we compute the validity metrics for the different datasets, as well as how we make the validity and uniqueness computation more efficient.

F.1 VALIDITY METRICS

Erdős-Renyi Given a graph G=(V,E) with n=|V| nodes and m=|E| edges, we want to determine whether the graph likely originates from an Erdős–Rényi model G(n,p) with edge probability p using a Wald test (Held & Sabanés Bové, 2013). For that, we follow the following steps distinguishing the cases in which the graphs are DAGs or not:

1. Empirical edge probability: we compute the number of possible edges

$$m_{\mathrm{max}} = egin{cases} rac{n(n-1)}{2} & ext{if the graph acyclic} \\ n(n-1) & ext{if the graph is not acyclic} \end{cases}$$

and then estimate the empirical probability of edge presence $\hat{p} = \frac{m}{m_{max}}$.

2. Wald test statistic: the Wald statistic tests the null hypothesis $H_0: \hat{p} = p$, where p is the expected edge probability:

$$W = \frac{(\hat{p} - p)^2}{\hat{p}(1 - \hat{p}) + \varepsilon}$$

and where we add a small regularization $\varepsilon = 10^{-6}$ to prevent division by zero.

3. p-value computation: assuming the null hypothesis, the Wald statistic W asymptotically follows a Chi-squared distribution with 1 degree of freedom:

$$p$$
-value = $1 - F_{\chi^2}(W; df = 1)$

where F_{χ^2} is the cumulative distribution function (CDF) of the Chi-squared distribution.

In the rare limit case where graphs contain only one node, we consider that the graph does not follow the distribution.

Stochastic Block Model To assess whether a graph G=(V,E) conforms to a Stochastic Block Model (SBM), we recover the block structure and probability parameters. The test then computes Wald statistics for intra- and inter-block edge probabilities.

1. Block assignment via model inference: Given the adjacency matrix $A \in \{0,1\}^{n \times n}$ of a graph G, we use an algorithm (Peixoto, 2014) to infer the stochastic block model (block assignment) from a given network:

Infer
$$z: V \to \{1, \dots, B\}$$
 using min $\mathcal{L}(G, z)$

where B is the number of non-empty blocks found and \mathcal{L} is the description length. The model can be further refined using Markov-Chain Monte Carlo (MCMC) for T timesteps.

2. Estimating intra- and inter-block probabilities: let N_i be number of nodes in block i and E_{ij} the number of edges between block i and block j recovered by the algorithm in the previous step. Then the estimated probabilities for directed SBM graphs are:

$$\hat{p}_{\text{intra},i} = \frac{E_{ii}}{N_i(N_i - 1) + \varepsilon}$$

$$\hat{p}_{\mathrm{inter},ij} = \frac{E_{ij}}{N_i N_j + \varepsilon}, \quad i \neq j$$

where $\varepsilon = 10^{-6}$ is a small regularization constant.

3. Wald test statistic: we compare the empirical estimates to expected values p_{intra} and p_{inter} using a Wald statistic:

$$\begin{split} W_{ii} &= \frac{(\hat{p}_{\mathsf{intra},i} - p_{\mathsf{intra}})^2}{\hat{p}_{\mathsf{intra},i}(1 - \hat{p}_{\mathsf{intra},i}) + \varepsilon} \\ W_{ij} &= \frac{(\hat{p}_{\mathsf{inter},ij} - p_{\mathsf{inter}})^2}{\hat{p}_{\mathsf{inter},ij}(1 - \hat{p}_{\mathsf{inter},ij}) + \varepsilon}, \quad i \neq j \end{split}$$

4. *p*-value computation: assuming the null hypothesis (i.e., estimated probabilities match expected ones), each Wald statistic follows a Chi-squared distribution with 1 degree of freedom:

$$p_{ij} = 1 - F_{\chi^2}(W_{ij}; df = 1),$$

and therefore the overall p-value can be computed as the mean of all p_{ij}

$$p$$
-value = $\frac{1}{B^2} \sum_{i=1}^{B} \sum_{j=1}^{B} p_{ij}$

Price's model To assess whether a graph follows a Price's model, we use a nonparametric two-sample Kolmogorov–Smirnov (KS) test:

- 1. Computing degree distribution: let $D = \{d_1, d_2, \dots, d_n\}$ be the degree sequence of the nodes in G. To reduce noise and ensure a more stable distribution, ignore nodes with degree ≤ 1 and end with the distribution $D' = \{d_i \in D \mid d_i > 1\}$.
- 2. Synthetic graph generation: we construct a synthetic graph G_{BA} using the Barabási–Albert model with the same number of nodes: $G_{BA} \sim BA(n, m)$, where n = |V| is the number of nodes and m = 6 is the number of edges each new node adds during attachment, fixed to the same value as in our data generation. The degree sequence of the synthetic graph is D_{BA} .
- 3. **Kolmogorov-Smirnov Two-Sample test:** we perform a two-sample Kolmogorov–Smirnov (KS) test to compare the empirical distribution functions of D' and D_{BA}

$$p$$
-value = $1 - KS_{2 \ sampled}(D', D_{BA})$

which evaluates the null hypothesis: $H_0: D' \sim D_{BA}$.

TPU Tiles For the TPU Tiles dataset, we report the percentage of valid Directed Acyclic Graphs (DAGs) as our primary validity metric, reflecting our focus on accurately reconstructing acyclic computational graphs.

Visual Genome As seen in Appendix E.3, by construction, object nodes can have outgoing edges to relationship or attribute nodes but only receive incoming edges from relationship nodes. Relationship nodes only have incoming edges from object nodes and send outgoing edges to objects. Finally, attributes can only receive edges from object nodes and do not have any outgoing edges. Therefore, to measure digraph validity we evaluate that the generated graphs verify these constraints.

F.2 Uniqueness and novelty

To evaluate the quality and novelty of generated graphs, we employ the usual metrics based on graph isomorphism. In particular we measure the fraction of isomorphic graphs from the sampled set to the train set (uniqueness) and the fraction of graphs from the sampled set that are not isomorphic to any other in the same sampled set (novelty).

However, since exact graph isomorphism testing can be computationally expensive, particularly for large or dense graphs such as the one in the TPU Tiles dataset, we incorporate a timeout mechanism. Specifically, if an isomorphism check does not complete within 5 seconds, it is treated as a timeout and the graph is conservatively assumed to be non-isomorphic.

In Table 10, we see that in three of the model configurations the computations timed out. We report the average percentage of graphs that could not be tested, which was 2.5% for DIGRESS, 0.8% for DEFOG, and 2% for DIRECTO RRWP.

F.3 MAXIMUM MEAN DISCREPANCY METRICS

For the different metrics, we adapt previous work from Martinkus et al. (2022); Law et al. (2025). We propose to measure both out-degree and in-degree distributions, as well as clustering, spectre and walvelet. To measure the *clustering* coefficient, we compute the distribution of directed local clustering coefficients using networkx function clustering (), which supports digraphs. For

the spectral features (*spectre* and *wavelet*), we derive the spectral features from the directed Laplacian, as described in Section 4.

In addition, the *orbit* metric that was also computed in Martinkus et al. (2022) has not been adapted to the directed setting as it relies on the Orbit Counting Algorithm (ORCA) which counts graphlets in networks but is only implemented in the undirected setting. Therefore, adapting this metric to the directed setting remains an open challenge.

F.4 JOINT NODE-EDGE DISTRIBUTIONAL METRICS

Downstream evaluations in graph generative models usually assume conditional graph generation and alignment with auxiliary inputs. Moreover, standard evaluations in domains such as Scene Graph Generation (Li et al., 2024; Lorenz et al., 2024) assume access to input images to compare generated graphs against ground truth images using retrieval metrics such as Precision@K and Recall@K. These require alignment with specific input conditions, which is not possible in our formulation as there are no ground truth images for the generated graphs. Instead, we propose metrics to directly evaluate generative performance by assessing joint node-edge distributional coverage, an essential aspect for labeled graphs such as NAS and scene graphs.

- **Node type distribution MMD:** To evaluate coverage of node class distributions, we compute normalized histograms over node labels for each graph and calculate the MMD score between generated and reference sets, which captures how well categorical proportions are preserved across generated graphs.
- Triplet-based precision and recall: Inspired by retrieval-style evaluations in Scene Graph Generation (Li et al., 2024; Lorenz et al., 2024), we extract semantic tuples from graphs. For scene graphs, we use (subject, attribute) pairs and (object, relation, object) triplets. For the TPU Tiles dataset, we extract element–element pairs. We compare the tuples from generated graphs with those in the test set and compute:

$$Precision = \frac{|correctly \text{ generated tuples}|}{|generated \text{ tuples}|} \quad Recall = \frac{|correctly \text{ generated tuples}|}{|test \text{ tuples}|}$$

• Embedding-based distances (FID and RBF): Following Thompson et al. (2022), we compute RBF-kernel MMD and Fréchet Inception Distance (FID) over embeddings extracted from a random GNN trunk. These embeddings encode both node labels and structural information, thus capturing *joint node-edge distributions*.

F.5 DOWNSTREAM TASKS METRICS

In addition to the distributional alignment evaluations, we also provide a evaluations on downstream tasks for the TPU Tiles dataset. Here, we train a *conditional* generative model and follow the evaluation protocol of LayerDAG (Li et al., 2025). Specifically, we employ their ML-based surrogate cost models to approximate the computational performance of generated architectures. This ensures direct comparability with prior work.

G EXPERIMENTAL DETAILS

G.1 DETAILS ON BASELINES

Maximum Likelihood Estimation (MLE) We define a simple baseline by estimating empirical probabilities from the training dataset via maximum likelihood estimation. The following distributions are computed:

1. **Number of Nodes Distribution:** Let n denote the number of nodes in a graph. The empirical distribution over n is given by:

$$P(n) = \frac{\text{Number of training graphs with } n \text{ nodes}}{\text{Total number of training graphs}}.$$

2. Node Class Distribution: Let c be a node class. The empirical node class distribution is:

$$P(v=c) = \frac{\text{Number of nodes of class } c}{\text{Total number of nodes in all training graphs}}.$$

3. Edge Type Distribution Conditioned on Node Pairs: Let (v_i, v_j) be a pair of nodes such that v_i has class c_a and v_j has class c_b . Let $e_{ij} \in \{1, \dots, K\}$ denote the edge type between them (with K total edge types). The empirical conditional distribution is:

$$P(e_{ij} = k \mid v_i = c_a, v_j = c_b) = \frac{\text{Number of edges of type } k \text{ between } (c_a, c_b)}{\sum_{k'=1}^K \text{Number of edges of type } k' \text{ between } (c_a, c_b)}$$

These distributions are stored and later used to construct graphs by first sampling the number of nodes, then sampling node types independently, and finally sampling edge types between each node pair according to the conditional edge distribution.

D-VAE (**Zhang et al., 2019**) This autoregressive method encodes and decodes directed acyclic graphs (DAGs) using an asynchronous message passing scheme. Unlike standard graph neural networks (GNNs), which apply simultaneous message passing across all nodes and updates them all at once, D-VAE updates nodes sequentially, allowing it to capture the computational flow within the graph rather than just its structure. During generation, the DAG is built one node at a time in topological order, with edges always directed toward newly added nodes ensuring the resulting graph remains acyclic. To enable this process, input graphs must be topologically sorted before being processed by the model.

To reproduce this baseline, we adapted the code available in their GitHub and arranged both the TPU Tiles and ER-DAG datasets to match the input format expected by the original model. We used the same hyperparameter configurations as suggested in the original paper to ensure consistency in training, which happened for 500 epochs. After generation, we converted the output DAGs back into the required format for compatibility with our evaluation metrics.

For ER-DAG, we tested two different learning rates 10^{-4} and 10^{-5} , and ended using the model with 10^{-5} , which resulted in better V.U.N. results with a training time of \sim 3min per epoch. For TPU Tiles, due to the large size of the dataset and some of the graphs in it, it was impossible to perform a training epoch in a reasonable time, as each of them was predicted to take \sim 12h.

LayerDAG (Li et al., 2025) This autoregressive diffusion model generates DAGs by converting them into sequences of bipartite graphs, effectively enabling a layer-wise tokenization suitable for autoregressive generation. At each step, a layer-wise diffusion process captures dependencies between nodes that are not directly comparable (i.e., not connected by a path). As with other autoregressive DAG models, the input graphs must be topologically sorted to ensure correct processing.

To reproduce this baseline, we adopted the implementation from GitHub adapted the ER-DAG data to the correct format ordering the graphs topologically, as TPU Tiles was already in the correct format. We kept the hyperparameters from the default configurations, including the number of epochs for each of the elements of the model. After generation, we converted the output DAGs back into the required format for compatibility with our evaluation metrics.

DiGress (Vignac et al., 2023a) To benchmark against DIGRESS, we consider its directed version by simply removing the symmetrization operations. This corresponds to DIRECTO-DD without dual attention and using the Laplacian positional encoding.

DeFoG (**Qin et al., 2025a**) To benchmark against DEFOG, we consider its directed version by again removing the symmetrization operations. In this case this corresponds to DIRECTO without dual attention and using the RRWP Positional encoding (without PPR).

G.2 TRAINING SETUP

This section details the training hyperparameters used across all experiments presented in the main text. Unless otherwise specified, the values reported below were used uniformly across all positional encoding variants and ablation settings. In particular, we report the choices for the training, for the positional encodings employed, and for the sampling.

Training The training hyperparameters used in our experiments are summarized in Table 6. These settings were consistently applied across all training runs for both DIRECTO and DIRECTO-DD (with discrete diffusion). We trained each model for up to 10,000 epochs, stopping the runs based on validation performance to account for variations in convergence behavior across datasets.

Table 6: Training and model hyperparameters used in all experiments.

Hyperparameter	Value				
Trai	ning Settings				
Learning rate	0.0002				
Weight decay	1×10^{-12}				
Optimizer	AdamW				
Mo	odel Settings				
Initial distribution	Marginal				
Train distortion	Identity				
Number of diffusion steps	500				
Noise schedule	Cosine				
Number of layers	5				
Hidden MLP dimensions	<i>X</i> : 256, <i>E</i> : 128, <i>y</i> : 128				
Transformer hidden dimensions	d_x : 256, d_e : 64, d_y : 64, n_{head} : 8				
Feedforward dims	\dim_{ff_X} : 256, \dim_{ff_E} : 128, \dim_{ff_u} : 128				
Training loss weights (λ_{train})	[5, 0]				

Positional encodings For RRWP, we set the walk length parameter to K=20. For MagLap with Q=5, we used equidistant potentials $\mathbf{q}_5=(0,0.1,0.2,0.3,0.4)$. For Q=10, we selected again 10 equidistant potentials $\mathbf{q}_{10}=(0.01,\ldots,0.1)$. In all cases, we then kept the k=10 first eigenvalues and eigenvectors, padding with null values whenever the graphs had less than 10 nodes.

Conditional generation To train with classifier-free guidance conditioning, we first conducted a hyperparameter search to determine the guidance strength with values from 0 to 4, in particular $\omega_{cond} \in (0, 0.25, 0.5, 1, 1.5, 2, 3, 4)$. We ultimately set the parameter to $\omega_{cond} = 0.25$.

Sampling To perform sampling optimization, we conducted a targeted search over the three key hyperparameters: the time distortion function, the target guidance factor (ω) , and the stochasticity coefficient (η) . Each hyperparameter was varied independently, while the others were held at their default values (identity distortion and $\omega = \eta = 0$). For computational efficiency, all searches were performed using 100 sampling steps, and each configuration was evaluated using five independent sampling runs to ensure robustness. An exception was made for the TPU Tiles dataset, where only a single sampling run was performed per configuration due to the large size of the dataset and some individual graphs.

Based on the outcome of this optimization, we selected the best-performing configurations for each combination of dataset and positional encoding, balancing the trade-off between V.U.N and ratio. The optimal configurations of the results reported in the main paper are summarized in Table 7. For the final evaluation, we performed five sampling runs per configuration using 1000 sampling steps. In all cases, the number of generated graphs matched the size of the test set (40 for synthetic datasets, 63 for Visual Genome), except for TPU Tiles, where we again limited the number of sampled digraphs to 40 due to computational constraints.

Finally, for the ablations on dual attention and positional encodings, we did not perform sampling optimization on η and ω to avoid the consequent computational cost, but searched for the optimal time distortion. For the scalability experiments, we also did not perform sampling optimization but chose the relevant optimal configuration (from Table 7). For DIRECTO-DD we performed 500 sampling steps in all the different model configurations.

G.3 RESOURCES AND RUNTIME

All experiments were conducted on a single NVIDIA A100-SXM4-80GB GPU. Table 8 summarizes the runtime of the training and sampling stages across the different datasets. These timings reflect

Table 7: Optimal sampling hyperparameters for each dataset and positional encoding variant.

Encoding	Distortion	ω	η
	ER-DAG		
Baseline	Polydec	0.3	10
RRWP	Polydec	0.1	25
MagLap	Polydec	0	100
	SBM		
Baseline	Revcos	0	0
RRWP	Polyinc	0.1	50
MagLap	Polydec	0.01	10
	TPU Tiles		
Baseline	Polydec	0	0
RRWP	Polyinc	0.3	10
MagLap	Polydec	0.5	100
	Visual Genom	ne	
Baseline	Cos	0.1	0
RRWP	Polydec	0.3	10
MagLap	Polydec	0.1	50

the training time until best performance and the average sampling time per sample, for all the configurations reported in the main results for DIRECTO.

Table 8: Training and sampling runtimes for each dataset and positional encoding variant.

Encoding	Training graphs	Training time (h)	Graphs sampled	Sampling time (min/sample)						
	ER-DAG									
Baseline	128	13.6	40	0.125						
RRWP	128	13.5	40	0.3						
MagLap	128	14.4	40	0.8						
		SB	M							
Baseline	128	23.7	40	0.3						
RRWP	128	13.7	40	0.5						
MagLap	128	21	40	2.1						
		TPU	Tiles							
Baseline	5040	10	40	1.1						
RRWP	5040	21	40	1.1						
MagLap	5040	49	40	6.7						
	Visual Genome									
Baseline	203	7.5	63	0.9						
RRWP	203	9	63	1.1						
MagLap	203	10	63	1.3						

H ADDITIONAL RESULTS

In this section, we present additional results that offer deeper insights into our model's performance and design choices. Specifically, we analyze the impact of the dual attention mechanism and the choice of positional encoding, compare performance on ER and DAG accuracy metrics, examine how dataset size influences generation quality, provide detailed results for conditional generation, and evaluate the effect of the sampling optimization step in discrete flow matching.

H.1 EXTENDED RESULTS FOR SYNTHETIC DATASETS

Table 9 reports the performance of DIRECTO across different configurations on synthetic datasets. We observe that the choice of architecture and positional encodings leads to noticeable differences in the distributional alignment metrics (MMD), highlighting the strong performance of DIRECTO. At

the same time, uniqueness and novelty remain consistently at 100% across all models, confirming that the V.U.N. ratio is driven uniquely by the validity metric.

Table 9: Directed graph generation performance on synthetic graphs for different configurations of DIRECTO. Results are presented as mean \pm standard deviation across five sampling runs. We considered Q=10 for the MagLap variants.

Model	Out-degree ↓	In-degree ↓	Clustering ↓	Spectre \	Wavelet ↓	Ratio ↓	Valid ↑	Unique ↑	Novel ↑	V.U.N. ↑
		Erdős-Renyi Directed Acyclic Graph (ER-DAG)								
Training set	0.0113	0.0103	0.0355	0.0038	0.0024	1.0	99.2	100	0.0	0.0
MLE	0.0083 ± 0.0004	0.0089 ± 0.0003	0.1318 ± 0.0077	0.0823 ± 0.0013	0.1162 ± 0.0018	15.1 ± 0.2	0.0 ± 0.0	100 ± 0.0	100 ± 0.0	0.0 ± 0.0
D-VAE	0.6158 ± 0.0160	0.6246 ± 0.0103	1.0509 ± 0.00304	0.6160 ± 0.0315	0.5432 ± 0.0389	106.6 ± 5.4	0.0 ± 0.0	100 ± 0.0	100 ± 0.0	0.0 ± 0.0
LayerDAG	0.0750 ± 0.0697	0.1773 ± 0.0722	0.1842 ± 0.0463	0.0159 ± 0.0120	0.0218 ± 0.0160	4.2 ± 3.2	21.5 ± 2.7	99.9 ± 0.0	100 ± 0.0	21.5 ± 2.7
DIGRESS	0.0138 ± 0.0035	0.0143 ± 0.0050	0.1074 ± 0.0090	0.0073 ± 0.0017	0.0042 ± 0.0011	1.9 ± 0.3	34.0 ± 4.1	100 ± 0.0	100 ± 0.0	34.0 ± 4.1
DEFoG	0.0407 ± 0.0008	0.0041 ± 0.0011	0.0460 ± 0.0052	0.0061 ± 0.0008	0.0008 ± 0.0003	1.6 ± 0.2	75 ± 2.2	100 ± 0.0	100 ± 0.0	75.0 ± 2.2
DIRECTO-DD RRWP	0.0142 ± 0.0040	0.0129 ± 0.0034	0.0408 ± 0.0053	0.0055 ± 0.0010	0.0048 ± 0.0014	1.4 ± 0.3	79.0 ± 3.7	100 ± 0.0	100 ± 0.0	79.0 ± 3.7
DIRECTO-DD MagLap	0.0145 ± 0.0040	0.0134 ± 0.0033	0.0582 ± 0.0083	0.0063 ± 0.0015	0.0034 ± 0.0011	1.5 ± 0.2	85.0 ± 9.2	100 ± 0.0	100 ± 0.0	85.0 ± 9.2
DIRECTO RRWP	0.0107 ± 0.0019	0.0104 ± 0.0012	0.1209 ± 0.0194	0.0054 ± 0.0005	0.0043 ± 0.0008	1.7 ± 0.1	94.0 ± 1.0	100 ± 0.0	100 ± 0.0	94.0 ± 1.0
DIRECTO MagLap	0.0117 ± 0.0014	0.0110 ± 0.0015	0.0711 ± 0.0120	0.0055 ± 0.0016	0.0026 ± 0.0004	1.3 ± 0.2	92.0 ± 3.7	100 ± 0.0	100 ± 0.0	92.0 ± 3.7
				Stochastic	Block Model (SB	M)				
Training set	0.0031	0.0031	0.0274	0.0027	0.0011	1.0	97.7	100	0.0	0.0
MLE	0.0020 ± 0.0002	0.0020 ± 0.0002	0.1973 ± 0.0162	0.0087 ± 0.0003	0.0508 ± 0.0009	11.6 ± 0.2	0.0 ± 0.0	100 ± 0.0	100 ± 0.0	0.0 ± 0.0
DIGRESS	0.0037 ± 0.0018	0.0038 ± 0.0018	0.0722 ± 0.0098	0.0045 ± 0.0004	0.0142 ± 0.0039	3.9 ± 0.9	41.5 ± 5.1	100 ± 0.0	100 ± 0.0	41.5 ± 5.1
DEFoG	0.0026 ± 0.0019	0.0022 ± 0.0016	0.0813 ± 0.0058	0.0048 ± 0.0002	0.0110 ± 0.0019	4.3 ± 0.8	37 ± 6.6	100 ± 0.0	100 ± 0.0	37.0 ± 6.6
DIRECTO-DD RRWP	0.0036 ± 0.0019	0.0036 ± 0.0018	0.0592 ± 0.0027	0.0038 ± 0.0007	0.0027 ± 0.0009	1.7 ± 0.4	81.5 ± 3.2	100 ± 0.0	100 ± 0.0	81.5 ± 3.2
DIRECTO-DD MagLap	0.0037 ± 0.0019	0.0038 ± 0.0018	0.0450 ± 0.0037	0.0038 ± 0.0006	0.0021 ± 0.0009	1.5 ± 0.4	95.5 ± 3.7	100 ± 0.0	100 ± 0.0	95.5 ± 3.7
DIRECTO RRWP	0.0031 ± 0.0014	0.0028 ± 0.0013	0.0594 ± 0.0027	0.0035 ± 0.0004	0.0027 ± 0.0009	1.8 ± 0.5	99.5 ± 1.0	100 ± 0.0	100 ± 0.0	99.5 ± 1.0
DIRECTO MagLap	0.0039 ± 0.0012	0.0038 ± 0.0010	0.0654 ± 0.0052	0.0038 ± 0.0003	0.0039 ± 0.0008	2.0 ± 0.3	96.5 ± 2.5	100 ± 0.0	100 ± 0.0	96.5 ± 2.5

H.2 EXTENDED RESULTS FOR REAL-WORLD DATASETS

Table 10 reports the performance of DIRECTO across different configurations on real-world datasets. While some configurations show evidence of partial memorization, particularly in node and edge distributions, this does not negatively affect the overall generative quality: V.U.N. remains high, and DIRECTO consistently achieves the best or second-best performance across the majority of metrics. These results highlight that, despite occasional replication of training structures, the model maintains strong distributional alignment and generates diverse, valid, and novel graphs.

Table 10: Directed graph generation performance on real-world graphs for different configurations of DIRECTO. Results are presented as mean \pm standard deviation across five sampling runs. We considered Q=5 for the MagLap variants. OOT indicates that the model could not be run within a reasonable timeframe. (*) indicates that isomorphism tests occasionally timed out, due to the large size of some graphs in this dataset; such cases were excluded from the uniqueness computation.

Model	Out-degree ↓	In-degree ↓	Clustering ↓	Spectre ↓	Wavelet ↓	Ratio ↓	Valid ↑	Unique ↑	Novel ↑	V.U.N. ↑
					TPU Tiles					
Training set	0.0003	0.0003	0.0007	0.0006	0.0002	1.0	100	100	0.0	0.0
MLE D-VAE LAYERDAG	0.0354 ± 0.0005 OOT 0.1933 ± 0.0905	0.0878 ± 0.0014 OOT 0.2225 ± 0.0395	0.0141 ± 0.0006 OOT 0.1512 ± 0.0522	0.0689 ± 0.0013 OOT 0.0501 ± 0.0206	0.0407 ± 0.0004 OOT 0.0765 ± 0.0251	149.8 ± 0.7 OOT 413.6 ± 70.1	24.7 ± 0.0 OOT 100 ± 0.0	99.9 ± 0.0 OOT 99.5 ± 1.0	100 ± 0.0 OOT 98.5 ± 3.0	24.7 ± 0.0 OOT 98.5 ± 3.0
DIGRESS DEFOG	0.0084 ± 0.0009 0.0099 ± 0.0012	$0.0726 \pm 0.0019 \\ 0.0794 \pm 0.0023$	$0.0020 \pm 0.0026 \\ 0.0042 \pm 0.0027$	0.0033 ± 0.0003 0.0040 ± 0.0005	$0.0018 \pm 0.0003 0.0017 \pm 0.0003$	$\frac{57.5}{63.7} \pm 1.7$	86.1 ± 2.3 86.3 ± 2.2	87.1 ^(*) ± 5.8 87.7 ^(*) ± 5.4	99.4 ± 0.6 93.3 ± 2.5	70.9 ± 3.4 72.0 ± 2.4
DIRECTO-DD RRWP DIRECTO-DD MagLap DIRECTO RRWP DIRECTO MagLap	$\begin{array}{c} 0.0093 \pm 0.0010 \\ 0.0115 \pm 0.0035 \\ 0.0133 \pm 0.0025 \\ 0.0039 \pm 0.0017 \end{array}$	$\begin{array}{c} 0.0767 \pm 0.0035 \\ 0.0703 \pm 0.0033 \\ 0.0859 \pm 0.0072 \\ 0.0376 \pm 0.0051 \end{array}$	$\begin{array}{c} 0.0015 \pm 0.0013 \\ 0.0103 \pm 0.0021 \\ 0.0136 \pm 0.0075 \\ 0.0211 \pm 0.0117 \end{array}$	$\begin{array}{c} 0.0045 \pm 0.0007 \\ 0.0076 \pm 0.0007 \\ 0.0086 \pm 0.0010 \\ 0.0126 \pm 0.0022 \end{array}$	$\begin{array}{c} 0.0018 \pm 0.0005 \\ 0.0043 \pm 0.0014 \\ 0.0038 \pm 0.0009 \\ 0.0062 \pm 0.0009 \end{array}$	61.0 ± 2.9 64.3 ± 5.3 75.4 ± 8.1 44.0 ± 7.1	86.5 ± 1.9 86.5 ± 5.1 97.0 ± 1.0 90.5 ± 3.3	$\begin{array}{c} 90.3 \pm 0.8 \\ 90.5 \pm 3.3 \\ 81.8^{(*)} \pm 4.5 \\ 90.5 \pm 4.6 \end{array}$	$\begin{array}{c} 99.6 \pm 0.5 \\ 100 \pm 0.0 \\ 96.5 \pm 1.2 \\ 97.5 \pm 3.2 \end{array}$	76.8 ± 1.9 77.0 ± 7.0 77.0 ± 2.9 80.5 ± 4.6
				,	Visual Genome					
Training set	0.0018	0.0030	0.0000	0.0072	0.0036	1.0	100	100	0.0	0.0
MLE DIGRESS DEFOG	$\begin{array}{c} 0.0607 \pm 0.0036 \\ 0.0654 \pm 0.0044 \\ 0.0447 \pm 0.0044 \end{array}$	$\begin{array}{c} 0.0474 \pm 0.0023 \\ 0.0389 \pm 0.0032 \\ 0.0396 \pm 0.0028 \end{array}$	$\begin{array}{c} 0.5342 \pm 0.0830 \\ 0.0008 \pm 0.0008 \\ 0.0002 \pm 0.0002 \end{array}$	$\begin{array}{c} 0.0535 \pm 0.0015 \\ 0.0416 \pm 0.0017 \\ 0.0122 \pm 0.0020 \end{array}$	$\begin{array}{c} 0.0399 \pm 0.0017 \\ 0.0225 \pm 0.0007 \\ 0.0089 \pm 0.0011 \end{array}$	$\begin{array}{c} 17.0 \pm 0.6 \\ 17.0 \pm 0.6 \\ 10.6 \pm 0.8 \end{array}$	$\begin{array}{c} 0 \pm 0.0 \\ 0.3 \pm 0.6 \\ 39.6 \pm 2.8 \end{array}$	$\begin{array}{c} 100 \pm 0.0 \\ 100 \pm 0.0 \\ 100 \pm 0.0 \end{array}$	$\begin{array}{c} 100 \pm 0.0 \\ 100 \pm 0.0 \\ 100 \pm 0.0 \end{array}$	$\begin{array}{c} 0.0 \pm 0.0 \\ 0.3 \pm 0.6 \\ 39.6 \pm 2.8 \end{array}$
DIRECTO-DD RRWP DIRECTO-DD MagLap DIRECTO RRWP DIRECTO MagLap	$\begin{array}{c} 0.0424 \pm 0.0043 \\ 0.0245 \pm 0.0022 \\ 0.0494 \pm 0.0021 \\ 0.0180 \pm 0.0024 \end{array}$	$\begin{array}{c} 0.0413 \pm 0.0037 \\ 0.0359 \pm 0.0036 \\ 0.0425 \pm 0.0029 \\ 0.0302 \pm 0.0040 \end{array}$	$\begin{array}{c} 0.0000 \pm 0.0000 \\ 0.0000 \pm 0.0000 \\ 0.0000 \pm 0.0000 \\ 0.0000 \pm 0.0000 \end{array}$	$\begin{array}{c} 0.0132 \pm 0.0053 \\ 0.0163 \pm 0.0026 \\ 0.0226 \pm 0.0075 \\ 0.0142 \pm 0.0021 \end{array}$	$\begin{array}{c} 0.0074 \pm 0.0008 \\ 0.0086 \pm 0.0011 \\ 0.0228 \pm 0.0058 \\ 0.0099 \pm 0.0013 \end{array}$	15.3 ± 0.8 $\frac{7.6}{12.8} \pm 0.7$ 12.8 ± 0.6 6.2 ± 0.5	$72.7 \pm 3.9 \\ 86.5 \pm 5.1 \\ 86.0 \pm 4.5 \\ 67.6 \pm 3.6$	$\begin{array}{c} 100 \pm 0.0 \\ 100 \pm 0.0 \\ 98.4 \pm 1.7 \\ 99.7 \pm 0.6 \end{array}$	$\begin{array}{c} 100 \pm 0.0 \\ 100 \pm 0.0 \\ 99.3 \pm 0.7 \\ 99.7 \pm 0.6 \end{array}$	$\frac{72.7}{61.9} \pm 3.9$ 83.8 ± 4.3 67.0 ± 4.3

Table 11 reports the node-label distributional alignment metrics for the two real-world datasets considered. The results highlight that DIRECTO consistently manages to capture node-label distributions accurately. On TPU Tiles, DIRECTO achieve the lowest node-type MMD, indicating strong alignment with the training set, while also maintaining high precision and competitive recall. On Visual Genome, although DIRECTO exhibits slightly lower node-type MMD compared to DeFoG, it attains the highest precision, recall, and RBF MMD, reflecting its ability to capture the underlying distribution. Overall, these results indicate that DIRECTO effectively balances reproducing node label

distributions while capturing richer graph structure, with the different positional encoding strategies providing complementary strengths in distributional alignment.

It is relevant to note that the low precision achieved in the training sets is due to the fact that the ground truth set is much larger than the generated set, and therefore there are many pairs and triplets present in the ground truth dataset that have not been generated.

Table 11: Directed graph generation performance on node-label distributional alignment metrics for the two real-world datasets. Results are presented as mean \pm standard deviation across five sampling runs.

Model	Node type (MMD) ↓	Precision ↑	Recall ↑	FID ↓	RBF (MMD) ↓
			TPU Tiles		
Training set	0.0001	0.64	0.99	0.0854	0.0021
MLE D-VAE LAYERDAG DIGRESS DEFOG	$\begin{array}{c} 0.4573 \pm 0.0070 \\ \text{OOT} \\ 0.0130 \pm 0.0077 \\ 0.0037 \pm 0.0033 \\ \underline{0.0031} \pm 0.0015 \end{array}$	$\begin{array}{c} 0.10 \pm 0.01 \\ OOT \\ 0.31 \pm 0.03 \\ 0.95 \pm 0.03 \\ 0.90 \pm 0.03 \end{array}$	$\begin{array}{c} 0.22 \pm 0.01 \\ OOT \\ 0.24 \pm 0.10 \\ \underline{0.46} \pm 0.05 \\ 0.45 \pm 0.05 \end{array}$	$\begin{array}{c} 105776.8 \pm 22676.3 \\ \hline OOT \\ 2864.1 \pm 1715.6 \\ 887.7 \pm 313.8 \\ \hline 159.5 \pm 108.9 \end{array}$	$\begin{array}{c} 1.0392 \pm 0.0326\\ \hline OOT\\ 1.0208 \pm 0.0225\\ 0.0969 \pm 0.0331\\ 0.0579 \pm 0.0150\\ \end{array}$
DIRECTO-DD RRWP DIRECTO-DD MagLap DIRECTO RRWP DIRECTO MagLap	$\begin{array}{c} 0.0028 \pm 0.0008 \\ 0.0051 \pm 0.0030 \\ \textbf{0.0018} \pm 0.0004 \\ 0.0086 \pm 0.0014 \end{array}$	$\begin{array}{c} 0.92 \pm 0.03 \\ 0.91 \pm 0.03 \\ \textbf{0.97} \pm 0.01 \\ \underline{0.96} \pm 0.02 \end{array}$	$\begin{array}{c} \textbf{0.48} \pm 0.02 \\ 0.42 \pm 0.03 \\ 0.44 \pm 0.03 \\ 0.42 \pm 0.02 \end{array}$	$\begin{array}{c} 336.6 \pm 163.9 \\ 482.2 \pm 124.3 \\ 293.0 \pm 110.1 \\ \textbf{96.0} \pm 64.0 \end{array}$	$\begin{array}{c} 0.0587 \pm 0.0225 \\ 0.0792 \pm 0.0266 \\ \underline{0.0438} \pm 0.0179 \\ \hline{\textbf{0.0421}} \pm 0.0080 \end{array}$
		•	Visual Genom	e	
Training set	0.0072	0.34	0.81	1.2	0.0214
MLE DIGRESS DEFOG	$\begin{array}{c} 0.0807 \pm 0.0030 \\ \underline{0.0206} \pm 0.0034 \\ \hline \textbf{0.0181} \pm 0.0030 \end{array}$	$\begin{array}{c} 0.25 \pm 0.03 \\ \underline{0.46} \pm 0.04 \\ 0.51 \pm 0.02 \end{array}$	$\begin{array}{c} 0.13 \pm 0.01 \\ 0.35 \pm 0.04 \\ 0.39 \pm 0.02 \end{array}$	$48941.0 \pm 19586.5 42.6 \pm 1.3 19.9 \pm 5.6$	$\begin{array}{c} 0.6179 \pm 0.0253 \\ 0.2321 \pm 0.0276 \\ 0.0845 \pm 0.0233 \end{array}$
DIRECTO-DD RRWP DIRECTO-DD MagLap DIRECTO RRWP DIRECTO MagLap	$\begin{array}{c} 0.0231 \pm 0.0082 \\ 0.0288 \pm 0.0069 \\ 0.0272 \pm 0.0056 \\ 0.0299 \pm 0.0047 \end{array}$	0.48 ± 0.02 0.50 ± 0.02 0.53 ± 0.02 0.58 ± 0.02	$\begin{array}{c} \textbf{0.48} \pm 0.02 \\ \underline{0.46} \pm 0.02 \\ 0.45 \pm 0.02 \\ \underline{0.46} \pm 0.01 \end{array}$	$\frac{4.8}{8.4} \pm 1.2$ 8.4 ± 2.5 4.7 ± 2.1 9.3 ± 2.6	$\begin{array}{c} \underline{0.0391} \pm 0.0047 \\ \hline 0.0420 \pm 0.0056 \\ \textbf{0.0383} \pm 0.0049 \\ 0.0507 \pm 0.0118 \end{array}$

H.3 THE ROLE OF DUAL ATTENTION

To assess the impact of the dual-attention mechanism in our model, we conduct an ablation study in which we remove the cross-attention between edge features and their transposes. This mechanism is designed to capture both source-to-target and target-to-source interactions, which are critical for modeling directional dependencies in directed graphs. By disabling dual attention, we isolate its contribution to generation quality, particularly in terms of validity, expressiveness, and generalization. We compare the full model with its ablated variant across model combinations to quantify the importance of this component.

DIRECTO Table 12 presents ablation results highlighting the impact of the dual attention mechanism in our method. The results are presented for two datasets: ER-DAG and SBM.

Table 12: Directed Graph Generation performance across different transformer architectures using discrete flow matching. MagLap considers Q=1.

Dataset	Model	Out-degree ↓	In-degree ↓	Clustering \downarrow	Spectre \	Wavelet ↓	Ratio ↓	Valid ↑	Unique ↑	Novel ↑	V.U.N. ↑
	No PE No PE - Dual	$\begin{array}{c} 0.0078 \pm 0.0008 \\ 0.0109 \pm 0.0012 \end{array}$	$\begin{array}{c} 0.0078 \pm 0.0010 \\ 0.0110 \pm 0.0012 \end{array}$	$\begin{array}{c} 0.1293 \pm 0.0024 \\ 0.0807 \pm 0.0147 \end{array}$	$\begin{array}{c} 0.0735 \pm 0.0023 \\ 0.0073 \pm 0.0007 \end{array}$	$\begin{array}{c} 0.0874 \pm 0.0030 \\ 0.0215 \pm 0.0017 \end{array}$	$12.2 \pm 0.4 \\ 3.0 \pm 0.2$	$\begin{array}{c} 0.0 \pm \scriptstyle{0.0} \\ 47.0 \pm \scriptstyle{12.1} \end{array}$	$\begin{array}{c} 100 \pm 0.0 \\ 100 \pm 0.0 \end{array}$	$\begin{array}{c} 100 \pm 0.0 \\ 100 \pm 0.0 \end{array}$	$\begin{array}{c} 0.0 \pm 0.0 \\ 47.0 \pm 12.1 \end{array}$
ER-DAG	RRWP RRWP - Dual	$\begin{array}{c} 0.0109 \pm 0.0019 \\ 0.0107 \pm 0.0019 \end{array}$	$\begin{array}{c} 0.0108 \pm 0.0017 \\ 0.0104 \pm 0.0012 \end{array}$	$\begin{array}{c} 0.0540 \pm 0.0112 \\ 0.1209 \pm 0.0194 \end{array}$	$\begin{array}{c} 0.0061 \pm 0.0008 \\ 0.0054 \pm 0.0005 \end{array}$	$\begin{array}{c} 0.0030 \pm 0.0005 \\ 0.0043 \pm 0.0008 \end{array}$	1.3 ± 0.1 1.7 ± 0.1	$67.5 \pm 1.6 \\ 94.0 \pm 1.0$	100 ± 0.0 100 ± 0.0	$\begin{array}{c} 100 \pm 0.0 \\ 100 \pm 0.0 \end{array}$	67.5 ± 1.6 94.0 ± 1.0
	MagLap MagLap - Dual	$\begin{array}{c} 0.0113 \pm 0.0024 \\ 0.0110 \pm 0.0017 \end{array}$	$\begin{array}{c} 0.0110 \pm 0.0015 \\ 0.0116 \pm 0.0021 \end{array}$	$\begin{array}{c} 0.1196 \pm 0.0107 \\ 0.0509 \pm 0.0017 \end{array}$	$\begin{array}{c} 0.0061 \pm 0.0011 \\ 0.0062 \pm 0.0014 \end{array}$	$\begin{array}{c} 0.0029 \pm 0.0006 \\ 0.0027 \pm 0.0005 \end{array}$	1.7 ± 0.2 1.3 ± 0.2	$74.0 \pm 4.4 \\ 91.0 \pm 2.5$	$\begin{array}{c} 100 \pm 0.0 \\ 100 \pm 0.0 \end{array}$	$\begin{array}{c} 100 \pm 0.0 \\ 100 \pm 0.0 \end{array}$	74.0 ± 4.4 91.0 ± 2.5
	No PE No PE - Dual	$\begin{array}{c} 0.0038 \pm 0.0021 \\ 0.0038 \pm 0.0011 \end{array}$	$\begin{array}{c} 0.0040 \pm 0.0020 \\ 0.0037 \pm 0.0010 \end{array}$	$\begin{array}{c} 0.1912 \pm 0.0178 \\ 0.0638 \pm 0.0059 \end{array}$	$\begin{array}{c} 0.0975 \pm 0.0028 \\ 0.0037 \pm 0.0003 \end{array}$	$\begin{array}{c} 0.0961 \pm 0.0071 \\ 0.0127 \pm 0.0018 \end{array}$	$\begin{array}{c} 20.5 \pm 2.0 \\ 3.5 \pm 0.4 \end{array}$	$\begin{array}{c} 0.0 \pm 0.0 \\ 48.5 \pm 6.4 \end{array}$	$\begin{array}{c} 100 \pm 0.0 \\ 100 \pm 0.0 \end{array}$	$\begin{array}{c} 100 \pm 0.0 \\ 100 \pm 0.0 \end{array}$	$\begin{array}{c} 0.0 \pm 0.0 \\ 48.5 \pm 6.4 \end{array}$
SBM	RRWP RRWP - Dual	$\begin{array}{c} 0.0036 \pm 0.0009 \\ 0.0038 \pm 0.0011 \end{array}$	$\begin{array}{c} 0.0034 \pm 0.0008 \\ 0.0037 \pm 0.0012 \end{array}$	$\begin{array}{c} 0.1276 \pm 0.0065 \\ 0.0492 \pm 0.0041 \end{array}$	$\begin{array}{c} 0.0345 \pm 0.0028 \\ 0.0035 \pm 0.0007 \end{array}$	$\begin{array}{c} 0.0961 \pm 0.0071 \\ 0.0015 \pm 0.0004 \end{array}$	21.4 ± 1.6 1.4 ± 0.2	13.5 ± 5.4 87.0 ± 5.1	100 ± 0.0 100 ± 0.0	100 ± 0.0 100 ± 0.0	13.5 ± 5.4 87.0 ± 5.1
	MagLap MagLap - Dual	$\begin{array}{c} 0.0033 \pm 0.0008 \\ 0.0039 \pm 0.0011 \end{array}$	$\begin{array}{c} 0.0034 \pm 0.0008 \\ 0.0036 \pm 0.0010 \end{array}$	$\begin{array}{c} 0.1356 \pm 0.0118 \\ 0.0653 \pm 0.0026 \end{array}$	$\begin{array}{c} 0.0481 \pm 0.0022 \\ 0.0033 \pm 0.0003 \end{array}$	$\begin{array}{c} 0.1250 \pm 0.0017 \\ 0.0038 \pm 0.0010 \end{array}$	27.7 ± 4.3 1.9 ± 0.3	$\begin{array}{c} 21.5 \pm 2.0 \\ 77.0 \pm 7.6 \end{array}$	100 ± 0.0 100 ± 0.0	$\begin{array}{c} 100 \pm 0.0 \\ 100 \pm 0.0 \end{array}$	21.5 ± 2.0 77.0 ± 7.6

In particular, we observe that, across both datasets, the inclusion of the dual attention mechanism consistently improves the validity of the generated graphs and reduces structural discrepancies as measured by clustering, spectral, and wavelet distances. In the ER-DAG setting, models with dual attention (e.g., RRWP-Dual and MagLap-Dual) significantly outperform their non-dual counterparts in validity, achieving up to 94% validity with RRWP-Dual and 91% with MagLap-Dual, compared to just

67.5% and 74%, respectively. These models also demonstrate better structural fidelity, particularly in clustering and spectral metrics. A similar trend is observed in the SBM dataset, where dual attention boosts validity (e.g., RRWP-Dual: 87%, MagLap-Dual: 77%). These results demonstrate how incorporating bidirectional information flow into the attention mechanism contributes to improved model performance and provides insight into the effectiveness of this architectural component.

DIRECTO-DD Table 13 shows a second ablation assessing the contribution of the dual attention mechanism within the discrete diffusion framework. In this case, we see a similar pattern to that observed under discrete flow matching: the incorporation of dual attention leads to consistent gains in graph validity across both ER-DAG and SBM datasets. Models augmented with dual attention not only produce more valid graphs but also exhibit improved alignment with structural statistics such as clustering, spectre, and wavelet.

Table 13: Directed Graph Generation performance across different transformer architectures using discrete diffusion. MagLap considers Q=1.

Dataset	Model	Out-degree ↓	In-degree ↓	Clustering ↓	Spectre ↓	Wavelet ↓	Ratio ↓	Valid ↑	Unique ↑	Novel ↑	V.U.N. ↑
	No PE No PE - Dual	$\begin{array}{c} 0.0094 \pm 0.0024 \\ 0.0149 \pm 0.0037 \end{array}$	$\begin{array}{c} 0.0095 \pm 0.0023 \\ 0.0138 \pm 0.0035 \end{array}$	$\begin{array}{c} 0.1221 \pm 0.0122 \\ 0.1256 \pm 0.0088 \end{array}$	$\begin{array}{c} 0.0814 \pm 0.0030 \\ 0.0089 \pm 0.0018 \end{array}$	$\begin{array}{c} 0.1094 \pm 0.0066 \\ 0.0106 \pm 0.0014 \end{array}$	14.4 ± 0.8 2.6 ± 0.3	0.0 ± 0.0 53.0 ± 2.9	100 ± 0.0 100 ± 0.0	$\begin{array}{c} 100 \pm 0.0 \\ 100 \pm 0.0 \end{array}$	0.0 ± 0.0 53.0 ± 2.9
ER-DAG	RRWP RRWP - Dual	$\begin{array}{c} 0.0147 \pm 0.0038 \\ 0.0142 \pm 0.0040 \end{array}$	$\begin{array}{c} 0.0139 \pm 0.0038 \\ 0.0129 \pm 0.0034 \end{array}$	$\begin{array}{c} 0.0985 \pm 0.0154 \\ 0.0408 \pm 0.0053 \end{array}$	$\begin{array}{c} 0.0067 \pm 0.0009 \\ 0.0055 \pm 0.0010 \end{array}$	$\begin{array}{c} 0.0038 \pm 0.0009 \\ 0.0048 \pm 0.0014 \end{array}$	2.1 ± 0.3 1.4 ± 0.3	$42.0 \pm 1.0 \\ 79.0 \pm 3.7$	$\begin{array}{c} 100 \pm 0.0 \\ 100 \pm 0.0 \end{array}$	$\begin{array}{c} 100 \pm 0.0 \\ 100 \pm 0.0 \end{array}$	42.0 ± 1.0 79.0 ± 3.7
	MagLap MagLap - Dual	$\begin{array}{c} 0.0144 \pm 0.0040 \\ 0.0142 \pm 0.0044 \end{array}$	$\begin{array}{c} 0.0135 \pm 0.0038 \\ 0.0135 \pm 0.0034 \end{array}$	$\begin{array}{c} 0.0792 \pm 0.0126 \\ 0.0438 \pm 0.0071 \end{array}$	$\begin{array}{c} 0.0071 \pm 0.0012 \\ 0.0057 \pm 0.0013 \end{array}$	$\begin{array}{c} 0.0036 \pm 0.0011 \\ 0.0046 \pm 0.0010 \end{array}$	1.6 ± 0.3 1.4 ± 0.3	$\begin{array}{c} 59.0 \pm 6.8 \\ 69.0 \pm 6.4 \end{array}$	$\begin{array}{c} 100 \pm 0.0 \\ 100 \pm 0.0 \end{array}$	$\begin{array}{c} 100 \pm 0.0 \\ 100 \pm 0.0 \end{array}$	$\begin{array}{c} 59.0 \pm 6.8 \\ 69.0 \pm 6.4 \end{array}$
	No PE No PE - Dual	$\begin{array}{c} 0.0038 \pm 0.0021 \\ 0.0037 \pm 0.0020 \end{array}$	$\begin{array}{c} 0.0040 \pm 0.0020 \\ 0.0039 \pm 0.0019 \end{array}$	$\begin{array}{c} 0.1912 \pm 0.0177 \\ 0.0721 \pm 0.0059 \end{array}$	$\begin{array}{c} 0.0120 \pm 0.0019 \\ 0.0055 \pm 0.0007 \end{array}$	$\begin{array}{c} 0.0975 \pm 0.0081 \\ 0.0403 \pm 0.0067 \end{array}$	$20.5 \pm 2.0 \\ 8.8 \pm 1.3$	0.0 ± 0.0 35.0 ± 9.1	100 ± 0.0 100 ± 0.0	$\begin{array}{c} 100 \pm 0.0 \\ 100 \pm 0.0 \end{array}$	0.0 ± 0.0 35.0 ± 9.1
SBM	RRWP RRWP - Dual	$\begin{array}{c} 0.0038 \pm 0.0019 \\ 0.0036 \pm 0.0019 \end{array}$	$\begin{array}{c} 0.0038 \pm 0.0018 \\ 0.0036 \pm 0.0018 \end{array}$	$\begin{array}{c} 0.1085 \pm 0.0205 \\ 0.0592 \pm 0.0027 \end{array}$	$\begin{array}{c} 0.0088 \pm 0.0009 \\ 0.0038 \pm 0.0007 \end{array}$	$\begin{array}{c} 0.0359 \pm 0.0043 \\ 0.0027 \pm 0.0009 \end{array}$	8.5 ± 0.3 1.7 ± 0.4	4.0 ± 2.0 81.5 ± 3.2	$\begin{array}{c} 100 \pm 0.0 \\ 100 \pm 0.0 \end{array}$	$\begin{array}{c} 100 \pm 0.0 \\ 100 \pm 0.0 \end{array}$	4.0 ± 2.0 81.5 ± 3.2
	MagLap MagLap - Dual	$\begin{array}{c} 0.0038 \pm 0.0019 \\ 0.0035 \pm 0.0018 \end{array}$	$\begin{array}{c} 0.0039 \pm 0.0019 \\ 0.0036 \pm 0.0018 \end{array}$	$\begin{array}{c} 0.0186 \pm 0.0046 \\ 0.0670 \pm 0.0032 \end{array}$	$\begin{array}{c} 0.0043 \pm 0.0006 \\ 0.0045 \pm 0.0008 \end{array}$	$\begin{array}{c} 0.0543 \pm 0.0072 \\ 0.0033 \pm 0.0013 \end{array}$	$11.3 \pm 1.6 \\ 1.9 \pm 0.4$	10.0 ± 4.2 66.5 ± 4.1	100 ± 0.0 100 ± 0.0	$\begin{array}{c} 100 \pm 0.0 \\ 100 \pm 0.0 \end{array}$	10.0 ± 4.2 66.5 ± 4.1

H.4 THE ROLE OF POSITIONAL ENCODINGS

To evaluate the importance of positional encodings in our model, we perform an ablation study comparing different options. Directed graphs lack a canonical node ordering, making positional information crucial for capturing structural context. We test several variants, including no positional encoding, encodings that do not take into accounts directed information, and then different directed positional encodings. This analysis isolates how each encoding contributes to the model's ability to generate valid and semantically meaningful graphs. We report performance across synthetic datasets for both discrete diffusion and flow matching.

DIRECTO Table 14 presents an ablation study analyzing the impact of various positional encoding (PE) strategies on directed graph generation performance under the discrete flow matching framework. This evaluation highlights the critical role of positional information in enabling models to capture the asymmetric and hierarchical structure inherent to directed graphs.

Table 14: Directed Graph Generation performance across different positional encodings using discrete flow matching.

Dataset	Model	Out-degree \downarrow	In-degree \downarrow	Clustering \downarrow	Spectre \downarrow	Wavelet \downarrow	Ratio ↓	Valid ↑	Unique ↑	Novel ↑	V.U.N. ↑
	No PE	0.0109 ± 0.0012	0.0110 ± 0.0012	0.0807 ± 0.0147	0.0073 ± 0.0007	0.0215 ± 0.0017	3.0 ± 0.2	47.0 ± 12.1	100 ± 0.0	100 ± 0.0	47.0 ± 12.1
	Lap	0.0119 ± 0.0020	0.0115 ± 0.0025	0.1272 ± 0.0224	0.0047 ± 0.0009	0.0048 ± 0.0005	1.8 ± 0.0	84.0 ± 4.9	100 ± 0.0	100 ± 0.0	84.0 ± 4.9
ER-DAG	RRWP	0.0107 ± 0.0019	0.0104 ± 0.0012	0.1209 ± 0.0194	0.0054 ± 0.0005	0.0043 ± 0.0008	1.7 ± 0.1	94.0 ± 1.0	100 ± 0.0	100 ± 0.0	94.0 ± 1.0
ER-DAG	MagLap	0.0110 ± 0.0017	0.0116 ± 0.0021	0.0509 ± 0.0017	0.0062 ± 0.0014	0.0027 ± 0.0005	1.3 ± 0.2	91.0 ± 2.5	100 ± 0.0	100 ± 0.0	91.0 ± 2.5
	MagLap(Q = 5)	0.0112 ± 0.0015	0.0107 ± 0.0022	0.0527 ± 0.0059	0.0056 ± 0.0009	0.0032 ± 0.0006	1.3 ± 0.2	91.5 ± 2.5	100 ± 0.0	100 ± 0.0	91.5 ± 2.5
	MagLap(Q = 10)	0.0117 ± 0.0014	0.0110 ± 0.0015	0.0711 ± 0.0120	0.0055 ± 0.0016	0.0026 ± 0.0004	1.3 ± 0.2	92.0 ± 3.7	100 ± 0.0	100 ± 0.0	92.0 ± 3.7
	No PE	0.0038 ± 0.0011	0.0037 ± 0.0010	0.0638 ± 0.0059	0.0037 ± 0.0003	0.0127 ± 0.0018	3.5 ± 0.4	48.5 ± 6.4	100 ± 0.0	100 ± 0.0	48.5 ± 6.4
	Lap	0.0040 ± 0.0012	0.0038 ± 0.0011	0.0552 ± 0.0042	$0.0048 \pm 0.000g$	0.0044 ± 0.0008	2.1 ± 0.3	71.5 ± 4.1	100 ± 0.0	100 ± 0.0	71.5 ± 4.1
SBM	RRWP	0.0038 ± 0.0011	0.0037 ± 0.0012	0.0492 ± 0.0041	0.0035 ± 0.0007	0.0015 ± 0.0004	1.4 ± 0.2	87.0 ± 5.1	100 ± 0.0	100 ± 0.0	87.0 ± 5.1
SDM	MagLap	0.0039 ± 0.0011	0.0036 ± 0.0010	0.0653 ± 0.0026	0.0033 ± 0.0003	0.0038 ± 0.0010	1.9 ± 0.3	77.0 ± 7.6	100 ± 0.0	100 ± 0.0	77.0 ± 7.6
	MagLap(Q = 5)	0.0039 ± 0.0010	0.0038 ± 0.0011	0.0748 ± 0.0028	0.0041 ± 0.0005	0.0070 ± 0.0015	2.6 ± 0.2	92.5 ± 2.2	100 ± 0.0	100 ± 0.0	92.5 ± 2.2
	MagLap(Q = 10)	0.0039 ± 0.0012	0.0038 ± 0.0010	0.0654 ± 0.0052	$0.0038\pm {\scriptstyle 0.0003}$	0.0039 ± 0.0008	2.0 ± 0.3	96.5 ± 2.5	100 ± 0.0	100 ± 0.0	96.5 ± 2.5

Overall, the inclusion of any form of positional encoding significantly improves generation validity compared to the baseline with no PE. Among the methods tested, directed encodings like RRWP and magnetic Laplacian-based variants demonstrate particularly strong performance. These encodings consistently enhance graph validity and reduce MMD ratio in both datasets. Notably, the MagLap variant with multiple potentials (Q=10) achieves the best results in terms of validity and structural fidelity, although resulting in a higher computational cost.

Interestingly, although classical Laplacian encodings (Lap) also play a role in increasing the V.U.N. ratio, they obtain worse results than the directed counterparts, emphasizing that for directed generation tasks, the choice of positional encoding is not merely a design detail but a relevant architectural decision that affects model success.

DIRECTO-DD Table 15 presents an ablation study assessing the influence of various positional encodings within the discrete diffusion framework across four synthetic datasets: SBM, ER-DAG, ER, and Price's model.

Table 15: Directed Graph Generation performance across different positional encodings using discrete diffusion.

Dataset	Model	Out-degree ↓	In-degree ↓	Clustering \(\psi	Spectre ↓	Wavelet ↓	Ratio ↓	Valid ↑	Unique ↑	Novel ↑	V.U.N.↑
ER-DAG	No PE Lap RRWP MagLap MagLap $(Q = 5)$ MagLap $(Q = 10)$	$\begin{array}{c} 0.0149 \pm 0.0037 \\ 0.0138 \pm 0.0038 \\ 0.0142 \pm 0.0040 \\ 0.0142 \pm 0.0044 \\ 0.0135 \pm 0.0032 \\ 0.0145 \pm 0.0040 \end{array}$	$\begin{array}{c} 0.0138 \pm 0.0035 \\ 0.0144 \pm 0.0042 \\ 0.0129 \pm 0.0034 \\ 0.0135 \pm 0.0034 \\ 0.0140 \pm 0.0045 \\ 0.0134 \pm 0.0033 \end{array}$	$\begin{array}{c} 0.1256 \pm 0.0088 \\ 0.0462 \pm 0.0071 \\ 0.0408 \pm 0.0053 \\ 0.0438 \pm 0.0071 \\ 0.0596 \pm 0.0081 \\ 0.582 \pm 0.0083 \end{array}$	$\begin{array}{c} 0.0089 \pm 0.0018 \\ 0.0055 \pm 0.0011 \\ 0.0055 \pm 0.0010 \\ 0.0057 \pm 0.0013 \\ 0.0061 \pm 0.0007 \\ 0.0063 \pm 0.0015 \end{array}$	$\begin{array}{c} 0.0106 \pm 0.0014 \\ 0.0052 \pm 0.0015 \\ 0.0048 \pm 0.0014 \\ 0.0046 \pm 0.0010 \\ 0.0037 \pm 0.0017 \\ 0.0034 \pm 0.0011 \end{array}$	2.6 ± 0.3 1.5 ± 0.3 1.4 ± 0.3 1.4 ± 0.3 1.4 ± 0.2 1.5 ± 0.2	53.0 ± 2.9 67.0 ± 5.3 79.0 ± 3.7 69.0 ± 6.4 78.5 ± 2.5 85.0 ± 9.2	$\begin{array}{c} 100 \pm 0.0 \\ \end{array}$	$\begin{array}{c} 100 \pm 0.0 \\ 100 \pm 0.0 \end{array}$	53.0 ± 2.9 67.0 ± 5.3 79.0 ± 3.7 69.0 ± 6.4 78.5 ± 2.5 85.0 ± 9.2
SBM	No PE Lap RRWP MagLap ($Q = 5$) MagLap ($Q = 10$)	$\begin{array}{c} 0.0037 \pm 0.0020 \\ 0.0037 \pm 0.0020 \\ 0.0036 \pm 0.0019 \\ 0.0035 \pm 0.0018 \\ 0.0039 \pm 0.0021 \\ 0.0037 \pm 0.0019 \end{array}$	$\begin{array}{c} 0.0039 \pm 0.0019 \\ 0.0038 \pm 0.0017 \\ 0.0036 \pm 0.0018 \\ 0.0036 \pm 0.0018 \\ 0.0038 \pm 0.0018 \\ 0.0038 \pm 0.0018 \end{array}$	$\begin{array}{c} 0.0721 \pm 0.0059 \\ 0.0531 \pm 0.0042 \\ 0.0592 \pm 0.0027 \\ 0.0670 \pm 0.0032 \\ 0.0504 \pm 0.0011 \\ 0.0450 \pm 0.0037 \end{array}$	$\begin{array}{c} 0.0055 \pm 0.0007 \\ 0.0038 \pm 0.0006 \\ 0.0038 \pm 0.0007 \\ 0.0045 \pm 0.0008 \\ 0.0047 \pm 0.0006 \\ 0.0038 \pm 0.0006 \end{array}$	$\begin{array}{c} 0.0403 \pm 0.0067 \\ 0.0106 \pm 0.0009 \\ 0.0027 \pm 0.0009 \\ 0.0033 \pm 0.0013 \\ 0.0065 \pm 0.0018 \\ 0.0021 \pm 0.0009 \end{array}$	8.8 ± 1.3 1.4 ± 0.4 1.7 ± 0.4 1.9 ± 0.4 2.4 ± 0.4 1.5 ± 0.4	35.0 ± 9.1 81.0 ± 3.7 81.5 ± 3.2 66.5 ± 4.1 92.0 ± 1.9 95.5 ± 3.7	$\begin{array}{c} 100 \pm 0.0 \\ 100 \pm 0.0 \end{array}$	$\begin{array}{c} 100 \pm 0.0 \\ 100 \pm 0.0 \end{array}$	35.0 ± 9.1 81.0 ± 3.7 81.5 ± 3.2 66.5 ± 4.1 92.0 ± 1.9 95.5 ± 3.7
ER	No PE Lap RRWP MagLap MagLap $(Q = 5)$	$\begin{array}{c} 0.0039 \pm 0.0022 \\ 0.0022 \pm 0.0014 \\ 0.0021 \pm 0.0013 \\ 0.0021 \pm 0.0013 \\ 0.0022 \pm 0.0014 \end{array}$	$\begin{array}{c} 0.0038 \pm 0.0023 \\ 0.0021 \pm 0.0014 \\ 0.0021 \pm 0.0013 \\ 0.0021 \pm 0.0013 \\ 0.0021 \pm 0.0014 \end{array}$	$\begin{array}{c} 0.0486 \pm 0.0039 \\ 0.0479 \pm 0.0058 \\ 0.0505 \pm 0.0037 \\ 0.0515 \pm 0.0055 \\ 0.0456 \pm 0.0068 \end{array}$	$\begin{array}{c} 0.0039 \pm 0.0009 \\ 0.0037 \pm 0.0013 \\ 0.0033 \pm 0.0013 \\ 0.0029 \pm 0.0004 \\ 0.0029 \pm 0.0006 \end{array}$	$\begin{array}{c} 0.0030 \pm 0.0019 \\ 0.0017 \pm 0.0010 \\ 0.0018 \pm 0.0010 \\ 0.0019 \pm 0.0011 \\ 0.0017 \pm 0.0010 \end{array}$	$\begin{array}{c} 2.8 \pm 1.4 \\ 1.8 \pm 0.9 \\ 1.8 \pm 0.8 \\ 1.8 \pm 0.8 \\ 1.8 \pm 0.9 \end{array}$	$\begin{array}{c} 100 \pm 0.0 \\ 99.5 \pm 1.0 \\ 99.5 \pm 1.0 \\ 99.5 \pm 1.0 \\ 100 \pm 0.0 \end{array}$	$\begin{array}{c} 100 \pm 0.0 \\ 100 \pm 0.0 \end{array}$	$\begin{array}{c} 100 \pm 0.0 \\ \end{array}$	$\begin{array}{c} 100 \pm 0.0 \\ 99.5 \pm 1.0 \\ 99.5 \pm 1.0 \\ 99.0 \pm 1.2 \\ 100 \pm 0.0 \end{array}$
Price	No PE Lap RRWP MagLap MagLap $(Q = 5)$	$\begin{array}{c} 0.0149 \pm 0.0020 \\ 0.0219 \pm 0.0030 \\ 0.0231 \pm 0.0034 \\ 0.0232 \pm 0.0013 \\ 0.0191 \pm 0.0031 \end{array}$	$\begin{array}{c} 0.0011 \pm 0.0002 \\ 0.0010 \pm 0.0002 \\ 0.0010 \pm 0.0002 \\ 0.0012 \pm 0.0001 \\ 0.0010 \pm 0.0001 \end{array}$	$\begin{array}{c} 0.0524 \pm 0.0030 \\ 0.0725 \pm 0.0016 \\ 0.0837 \pm 0.0022 \\ 0.0752 \pm 0.0028 \\ 0.0653 \pm 0.0118 \end{array}$	$\begin{array}{c} 0.0041 \pm 0.0004 \\ 0.0476 \pm 0.0034 \\ 0.0619 \pm 0.0048 \\ 0.0531 \pm 0.0059 \\ 0.0239 \pm 0.0023 \end{array}$	$\begin{array}{c} 0.0017 \pm 0.0000 \\ 0.0124 \pm 0.0020 \\ 0.0123 \pm 0.0027 \\ 0.0126 \pm 0.0019 \\ 0.0044 \pm 0.0016 \end{array}$	$\begin{array}{c} 2.9 \pm 0.1 \\ 16.2 \pm 2.0 \\ 17.0 \pm 2.8 \\ 16.8 \pm 2.1 \\ 6.8 \pm 1.7 \end{array}$	$\begin{array}{c} 92.5 \pm 1.6 \\ 99.0 \pm 1.2 \\ 99.0 \pm 1.2 \\ 97.5 \pm 2.2 \\ 99.5 \pm 1.0 \end{array}$	$\begin{array}{c} 100 \pm 0.0 \\ 100 \pm 0.0 \end{array}$	$\begin{array}{c} 100 \pm 0.0 \\ \end{array}$	$\begin{array}{c} 92.5 \pm 1.6 \\ 99.0 \pm 1.2 \\ 99.0 \pm 1.2 \\ 97.5 \pm 2.2 \\ 99.5 \pm 1.0 \end{array}$

We observe that that ER and Price graphs, due to their simplicity and highly regular generative processes, pose a relatively easy modeling challenge. As a result, performance is consistently high across all variants, including the baseline with no positional encoding. In contrast, the SBM and ER-DAG datasets present more intricate structural patterns, which amplify the benefits of informed positional encodings. In these cases, clear performance gaps emerge between the baseline, non-directed encodings (e.g., Lap), and directed-aware methods such as RRWP and MagLapPE.

These differences highlight the importance of encoding directionality to faithfully capture the distribution of more structurally diverse directed graphs. For this reason, in the main paper we focus our synthetic evaluations on SBM and ER-DAG, where the modeling challenge is sufficiently rich to reveal the comparative strengths of different modeling strategies.

H.5 ER VS DAG PERFORMANCE

To evaluate the structural quality of generated synthetic directed acyclic graphs, we defined a composite validity metric that captures two key properties: (i) the percentage of generated graphs that are Directed Acyclic Graphs (DAGs), and (ii) the percentage that follow the target structural distribution (e.g. Erdős-Renyi). The validity score is computed as the proportion of generated graphs that satisfy both criteria. For completeness, we also report each component individually to disentangle the contributions of acyclicity and distributional alignment.

Table 16: ER vs DAG accuracy

Model	% DAG	% ER	Valid
Training set	100	99.2	99.2
MLE D-VAE LAYERDAG DIGRESS DEFOG	$\begin{array}{c} 0.0 \pm 0.0 \\ 100 \pm 0.0 \\ 100 \pm 0.0 \\ 35.0 \pm 4.2 \\ 21.5 \pm 2.7 \end{array}$	$\begin{array}{c} 97.0 \pm 2.1 \\ 0.0 \pm 0.0 \\ 21.5 \pm 2.7 \\ 98.5 \pm 2.0 \\ 100 \pm 0.0 \end{array}$	$\begin{array}{c} 0.0 \pm 0.0 \\ 0.0 \pm 0.0 \\ 21.5 \pm 2.7 \\ 34.0 \pm 4.1 \\ 21.5 \pm 2.7 \end{array}$
DIRECTO-DD RRWP DIRECTO-DD MagLap ($Q = 10$) DIRECTO RRWP DIRECTO MagLap ($Q = 10$)	79.0 ± 3.7 86.0 ± 9.4 94.0 ± 1.0 99.5 ± 1.0	100 ± 0.0 99 ± 1.2 100 ± 0.0 92.5 ± 2.7	$79.0 \pm 3.7 \\ 85.0 \pm 10.2 \\ 94.0 \pm 1.0 \\ 92.0 \pm 3.7$

As shown in Table 16, baselines such as MLE and LAYERDAG exhibit a stark imbalance: while LAYERDAG guarantees acyclicity, both fail to model the target ER distribution, resulting in low overall validity. On the other hand, MLE closely aligns with the distribution but fails to generate acyclic graphs.

In contrast, diffusion- and flow matching—based methods paired with dual attention and relevant directed positional encodings achieve strong performance on both fronts, demonstrating their ability to generate structurally valid DAGs that also align with the underlying data distribution. This highlights the limitations of purely autoregressive or heuristic DAG-specific approaches when used in isolation.

H.6 SCALABILITY EXPERIMENTS

In this section, we investigate the scalability of our method with respect to three key axes: dataset size, parameter efficiency, and graph size. These experiments are designed to disentangle the contributions of data availability, architectural choices, and input complexity to the overall generative performance, providing a clearer understanding of the trade-offs between accuracy, efficiency, and computational cost in our framework.

Effect of dataset size To evaluate the effect on the number of graphs available at training time, we conduct an ablation study using the synthetic ER-DAG dataset in two configurations: the standard size and a variant with 10× more training, test, and validation samples. This setup allows us to assess whether the method encodings benefit from increased data. We compare the different positional encodings for discrete diffusion using dual attention, with results in Table 17.

Dataset	Model	Out-degree ↓	In-degree ↓	Clustering ↓	Spectre ↓	Wavelet ↓	Ratio ↓	Valid ↑	Unique ↑	Novel ↑	V.U.N. ↑
	Train set	0.0113	0.0103	0.0355	0.0038	0.0024	1.0	99.2	100	0.0	0.0
	Lap	0.0138 ± 0.0038	0.0144 ± 0.0042	0.0462 ± 0.0071	0.0055 ± 0.0011	0.0052 ± 0.0015	1.5 ± 0.3	67.0 ± 5.3	100 ± 0.0	100 ± 0.0	67.0 ± 5.3
Standard	RRWP	0.0142 ± 0.0040	0.0129 ± 0.0034	0.0408 ± 0.0053	0.0055 ± 0.0010	0.0048 ± 0.0014	1.4 ± 0.3	79.0 ± 3.7	100 ± 0.0	100 ± 0.0	79.0 ± 3.7
	MagLap	0.0142 ± 0.0044	0.0135 ± 0.0034	0.0438 ± 0.0071	0.0057 ± 0.0013	0.0046 ± 0.0010	1.4 ± 0.3	69.0 ± 6.4	100 ± 0.0	100 ± 0.0	69.0 ± 6.4
	MagLap (Q = 5)	0.0135 ± 0.0032	0.0140 ± 0.0045	0.0596 ± 0.0081	0.0061 ± 0.0007	0.0037 ± 0.0017	1.4 ± 0.2	78.5 ± 2.5	100 ± 0.0	100 ± 0.0	78.5 ± 2.5
	Train set	0.0002	0.0003	0.0021	0.0004	0.0000	1.0	99.9	100	0.0	0.0
	Lap	0.00035 ± 0.0007	0.0032 ± 0.0008	0.0261 ± 0.0025	0.0024 ± 0.0003	0.0006 ± 0.0001	10.5 ± 1.3	85.5 ± 2.4	100 ± 0.0	100 ± 0.0	85.5 ± 2.4
x 10	RRWP	0.0030 ± 0.0008	0.0031 ± 0.0006	0.0277 ± 0.0075	0.0024 ± 0.0004	0.0006 ± 0.0002	10.1 ± 2.2	94.0 ± 4.4	100 ± 0.0	100 ± 0.0	94.0 ± 4.4
	MagLap	0.0030 ± 0.0006	0.0033 ± 0.0005	0.0305 ± 0.0051	0.0025 ± 0.0005	0.0007 ± 0.0003	14.5 ± 2.4	89.5 ± 3.7	100 ± 0.0	100 ± 0.0	89.5 ± 3.7
	MagLap (Q = 5)	0.0031 ± 0.0008	0.0028 ± 0.0006	0.0237 ± 0.0028	0.0022 ± 0.0006	0.0008 ± 0.0001	9.6 ± 1.6	93.5 ± 2.5	100 ± 0.0	100 ± 0.0	93.5 ± 2.5

Overall, we see that increasing the dataset size significantly improves generation performance across all positional encoding variants, confirming that additional training data helps models better capture structural patterns. However, this performance gain comes at the cost of substantially longer training times and greater computational demand (\sim 12h for the standard dataset vs \sim 32h for the bigger version). These trade-offs motivate our focus on architectural innovations such as employing discrete flow matching as more efficient alternatives to scaling purely through data and compute.

Effect of model size (parameter efficiency) We next evaluate parameter efficiency by contrasting our dual-attention mechanism with an alternative approach that scales model capacity by doubling the number of parameters. Dual attention increases the parameter space by introducing two adjacency-based attention heads, each specialized for handling edge directionality. To ablate for model size, we compare against a baseline in which the architecture is widened to match the parameter count, but without dual-attention.

Table 18: Directed Graph Generation performance for the dual attention architecture versus doubling the depth of the network without using the dual attention mechanism.

Dataset	Model	Out-degree \downarrow	In-degree \downarrow	Clustering \downarrow	Spectre \downarrow	Wavelet ↓	Ratio ↓	Valid ↑	Unique ↑	Novel ↑	V.U.N. ↑
ER-DAG	RRWP - Double RRWP - Dual	$\begin{array}{c} 0.0129 \pm 0.0020 \\ 0.0107 \pm 0.0019 \end{array}$	$\begin{array}{c} 0.0130 \pm 0.0015 \\ 0.0104 \pm 0.0012 \end{array}$	$\begin{array}{c} 0.1741 \pm 0.0200 \\ 0.1209 \pm 0.0194 \end{array}$	$\begin{array}{c} 0.0107 \pm 0.0007 \\ 0.0054 \pm 0.0005 \end{array}$	$\begin{array}{c} 0.0020 \pm 0.0005 \\ 0.0043 \pm 0.0008 \end{array}$	4.9 ± 0.2 1.7 ± 0.1	$\begin{array}{c} 72.0 \pm 9.8 \\ 94.0 \pm 1.0 \end{array}$	$\begin{array}{c} 100 \pm 0.0 \\ 100 \pm 0.0 \end{array}$	$\begin{array}{c} 100 \pm 0.0 \\ 100 \pm 0.0 \end{array}$	72.0 ± 9.8 94.0 ± 1.0
	MagLap - Double MagLap - Dual	$\begin{array}{c} 0.0131 \pm 0.0019 \\ 0.0110 \pm 0.0017 \end{array}$	$\begin{array}{c} 0.0118 \pm 0.0022 \\ 0.0116 \pm 0.0021 \end{array}$	$\begin{array}{c} 0.1237 \pm 0.0217 \\ 0.0509 \pm 0.0017 \end{array}$	$\begin{array}{c} 0.0095 \pm 0.0030 \\ 0.0062 \pm 0.0014 \end{array}$	$\begin{array}{c} 0.0020 \pm 0.0008 \\ 0.0027 \pm 0.0005 \end{array}$	4.3 ± 0.7 1.3 ± 0.2	$\begin{array}{c} 80.0 \pm 6.3 \\ 91.0 \pm 2.5 \end{array}$	$\begin{array}{c} 100 \pm 0.0 \\ 100 \pm 0.0 \end{array}$	$\begin{array}{c} 100 \pm 0.0 \\ 100 \pm 0.0 \end{array}$	80.0 ± 6.3 91.0 ± 2.5
SBM	RRWP - Double RRWP - Dual	$\begin{array}{c} 0.0083 \pm 0.0024 \\ 0.0038 \pm 0.0011 \end{array}$	$\begin{array}{c} 0.0081 \pm 0.0025 \\ 0.0037 \pm 0.0012 \end{array}$	$\begin{array}{c} 0.1789 \pm 0.0107 \\ 0.0492 \pm 0.0041 \end{array}$	$\begin{array}{c} 0.0084 \pm 0.0014 \\ 0.0035 \pm 0.0007 \end{array}$	0.000 0.000	27.1 ± 2.3 1.4 ± 0.2	$\begin{array}{c} 0.0 \pm 0.0 \\ 87.0 \pm 5.1 \end{array}$	$\begin{array}{c} 100 \pm 0.0 \\ 100 \pm 0.0 \end{array}$	$\begin{array}{c} 100 \pm 0.0 \\ 100 \pm 0.0 \end{array}$	0.0 ± 0.0 87.0 ± 5.1
	MagLap - Double MagLap - Dual	$\begin{array}{c} 0.0081 \pm 0.0025 \\ 0.0039 \pm 0.0011 \end{array}$	$\begin{array}{c} 0.0079 \pm 0.0020 \\ 0.0036 \pm 0.0010 \end{array}$	$\begin{array}{c} 0.1799 \pm 0.0097 \\ 0.0653 \pm 0.0026 \end{array}$	$\begin{array}{c} 0.0307 \pm 0.0052 \\ 0.0033 \pm 0.0003 \end{array}$	$\begin{array}{c} 0.0723 \pm 0.0156 \\ 0.0038 \pm 0.0010 \end{array}$	$\begin{array}{c} 24.8 \pm 4.6 \\ \textbf{1.9} \pm \textbf{0.3} \end{array}$	$\begin{array}{c} 6.0 \pm 4.9 \\ 77.0 \pm 7.6 \end{array}$	$\begin{array}{c} 100 \pm 0.0 \\ 100 \pm 0.0 \end{array}$	$\begin{array}{c} 100 \pm 0.0 \\ 100 \pm 0.0 \end{array}$	6.0 ± 4.9 77.0 \pm 7.6

As shown in Table 18, this baseline fails to recover the correct edge distribution, particularly in more challenging regimes such as SBM graphs. In contrast, the dual-attention model achieves

substantially higher fidelity, demonstrating that our architecture leverages parameters more effectively by embedding structural inductive bias rather than merely increasing model scale.

Effect of node size We finally investigate how the method scales with increasing graph size by conducting experiments on ER-DAG datasets ranging from 80–150 up to 200–250 nodes (see Table 19 for dataset statistics). Due to the poor scalability of MultMagLap encodings, we restrict this ablation to RRWP and MagLap positional encodings, with the largest graphs (200–250 nodes) evaluated only under RRWP. Training and sampling times, together with generation quality, are reported in Table 20. Importantly, the computational overhead introduced by dual attention remains bounded by a constant factor of two and does not affect the overall asymptotic complexity, which matches that of standard graph transformers.

Table 19: Dataset statistics for the synthetic experiments with larger graph size (nodes and edges).

Min. nodes	Max. nodes	Avg. nodes	Min. edges	Max. edges	Avg. edges
80	150	117	1866	6699	4170
150	200	173	6643	11851	9046
200	250	225	11982	18645	15148

In terms of positional encodings, MagLap exhibits clear scalability limitations, both in runtime and performance, whereas RRWP features scale considerably better, consistent with prior findings (e.g., Appendix G.4 of DeFoG (Qin et al., 2025a)). Regarding generative performance, DIRECTO demonstrates strong distributional fidelity across node sizes, as reflected in the Ratio and distributional validity scores. However, ensuring strict acyclicity becomes increasingly challenging at scale: a single misplaced edge can violate the constraint entirely, and the risk grows quadratically with the number of nodes. This highlights the inherent difficulty of enforcing global constraints in large directed graphs, motivating future work on more robust inductive biases for acyclicity preservation.

Table 20: Scaling performance of DIRECTO on ER-DAG datasets of increasing node size.

Model	Out-degree \downarrow	In-degree \downarrow	Clustering \downarrow	Spectre ↓	Wavelet ↓	Ratio ↓	Valid ↑	Unique ↑	Novel ↑	V.U.N. ↑	Train (h)	Min / sample
80-150 (RRWP)	0.0045 ± 0.0001	0.0044 ± 0.0008	0.3233 ± 0.0676	0.0010 ± 0.0003	0.0003 ± 0.0001	3.7 ± 0.5	53.5 ± 3.0	100 ± 0.0	100 ± 0.0	53.5 ± 3.0	22	0.285
80-150 (MagLap)	0.0040 ± 0.0005	0.0044 ± 0.0005	0.3382 ± 0.0361	0.0015 ± 0.0002	0.0007 ± 0.0002	4.2 ± 0.3	45.0 ± 7.1	100 ± 0.0	100 ± 0.0	45.0 ± 7.1	26	0.940
150-200 (RRWP)	0.0034 ± 0.0002	0.0031 ± 0.0002	0.1570 ± 0.0496	0.003 ± 0.0000	0.0000 ± 0.0000	1.7 ± 0.3	60.0 ± 5.9	100 ± 0.0	100 ± 0.0	60.0 ± 5.9	28	0.555
150-200 (MagLap)	0.0031 ± 0.0005	0.0031 ± 0.0004	0.6691 ± 0.0558	0.0004 ± 0.0000	0.0001 ± 0.0001	3.2 ± 0.4	34.5 ± 1.9	100 ± 0.0	100 ± 0.0	34.5 ± 1.9	38	1.365
200-250 (RRWP)	0.0034 ± 0.0002	0.0033 ± 0.0003	0.0411 ± 0.0178	0.0003 ± 0.0000	0.0000 ± 0.0000	1.9 ± 0.3	2.0 ± 2.4	100 ± 0.0	100 ± 0.0	2.0 ± 2.4	40	0.645

H.7 CONDITIONAL GENERATION

Table 21 shows the results of the experiments with classifier-free guidance conditional generation. We followed the setup of Li et al. (2025), training on the TPU Tiles dataset with the provided conditional information and evaluating with their available suite and surrogate models.

Table 21: Averaged conditional generation results across 3 runs. Baseline results were obtained from Li et al. (2025), where Spearman correlation was not reported.

Model	Pearson	Spearman	MAE
Real graphs	0.75 ± 0.01	0.83 ± 0.01	0.96 ± 0.00
D-VAE	0.50 ± 0.01	N/A	1.4 ± 0.00
GRAPHRNN	0.62 ± 0.02	N/A	1.3 ± 0.00
GRAPHPNAS	0.24 ± 0.10	N/A	2.1 ± 0.06
ONESHOTDAG	0.56 ± 0.02	N/A	1.4 ± 0.01
LAYERDAG (T=1)	0.37 ± 0.11	N/A	2.0 ± 0.04
LayerDAG	0.65 ± 0.01	N/A	1.2 ± 0.01
DIRECTO	0.59 ± 0.01	0.63 ± 0.03	1.3 ± 0.01

Unlike methods explicitly designed for conditional DAG generation, our framework is general and primarily optimized for unconditional digraph generation. In contrast, autoregressive models such as GraphRNN and LayerDAG (especially the latter, where conditional generation is the default training setup) are naturally more suited for this task and thus represent strong baselines. Moreover, our evaluation follows their official suite, which is tailored to their own method and may not fully align with our formulation.

Despite this, DIRECTO achieves competitive performance. In Pearson correlation, DIRECTO ranks just behind LayerDAG and GraphRNN, while performing on par with them in mean absolute error (MAE). Notably, it also outperforms LAYERDAG's one-shot variant ONESHOTDAG. We further report Spearman correlation, which is implemented in the evaluation suite but was not included in prior work. These results show that even though conditional generation is not our main focus, DIRECTO achieves a strong balance across all metrics, demonstrating that our framework can readily extend to conditional tasks without specialized architectural modifications.

Finally, our results were obtained using classifier-free guidance, a straightforward extension that may not be optimal for conditional training in our setting. We expect that more dedicated strategies for conditioning could further improve performance. Overall, these findings highlight the versatility of DIRECTO: while unconditional generation remains our primary focus, its ability to adapt effectively to conditional generation underscores the promise of diffusion-based formulations for directed graph generation.

H.8 IMPACT OF SAMPLING OPTIMIZATION USING DISCRETE FLOW MATCHING

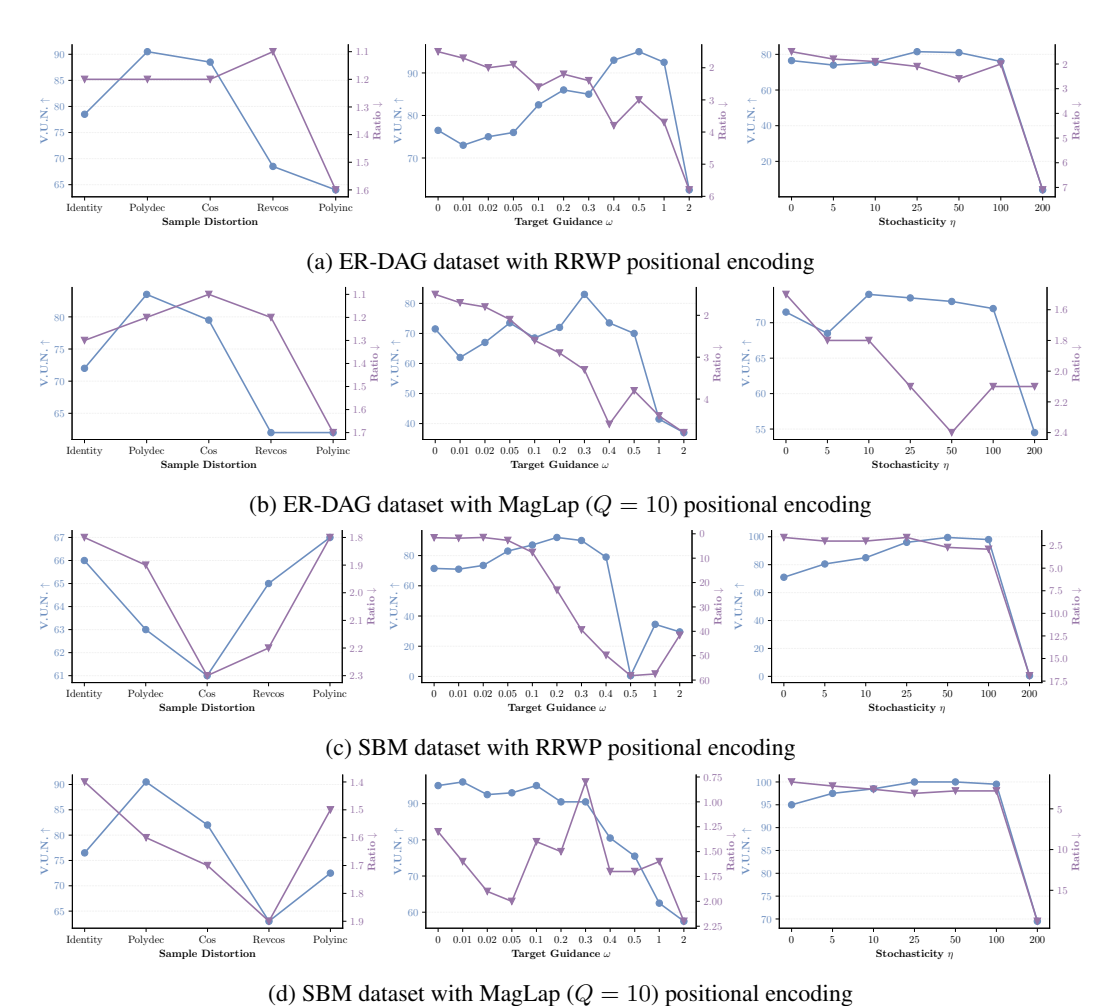


Figure 4: Sampling optimization curves for the synthetic datasets with 100 sampling steps and 5 sampling runs. We represent V.U.N. (blue) and MMD ratio (purple) and optimize for best trade-off for each of the three parameters individually.

To better understand the influence of the three sampling hyperparameters discussed in Appendix C: time distortion, stochasticity coefficient (η) , and target guidance factor (ω) on generative performance, we analyze their effect on the V.U.N. and the structural ratio. Specifically, we present performance curves for the four primary datasets reported in the main results table: SBM, RRWP, TPU Tiles, and

Visual Genome. For each dataset, we evaluate the impact of these parameters under two positional encoding strategies: RRWP and MagLap. We report the results for 100 sampling steps and 5 different sampling runs (except for TPU Tiles where only 1 run was performed due to computational constraints).

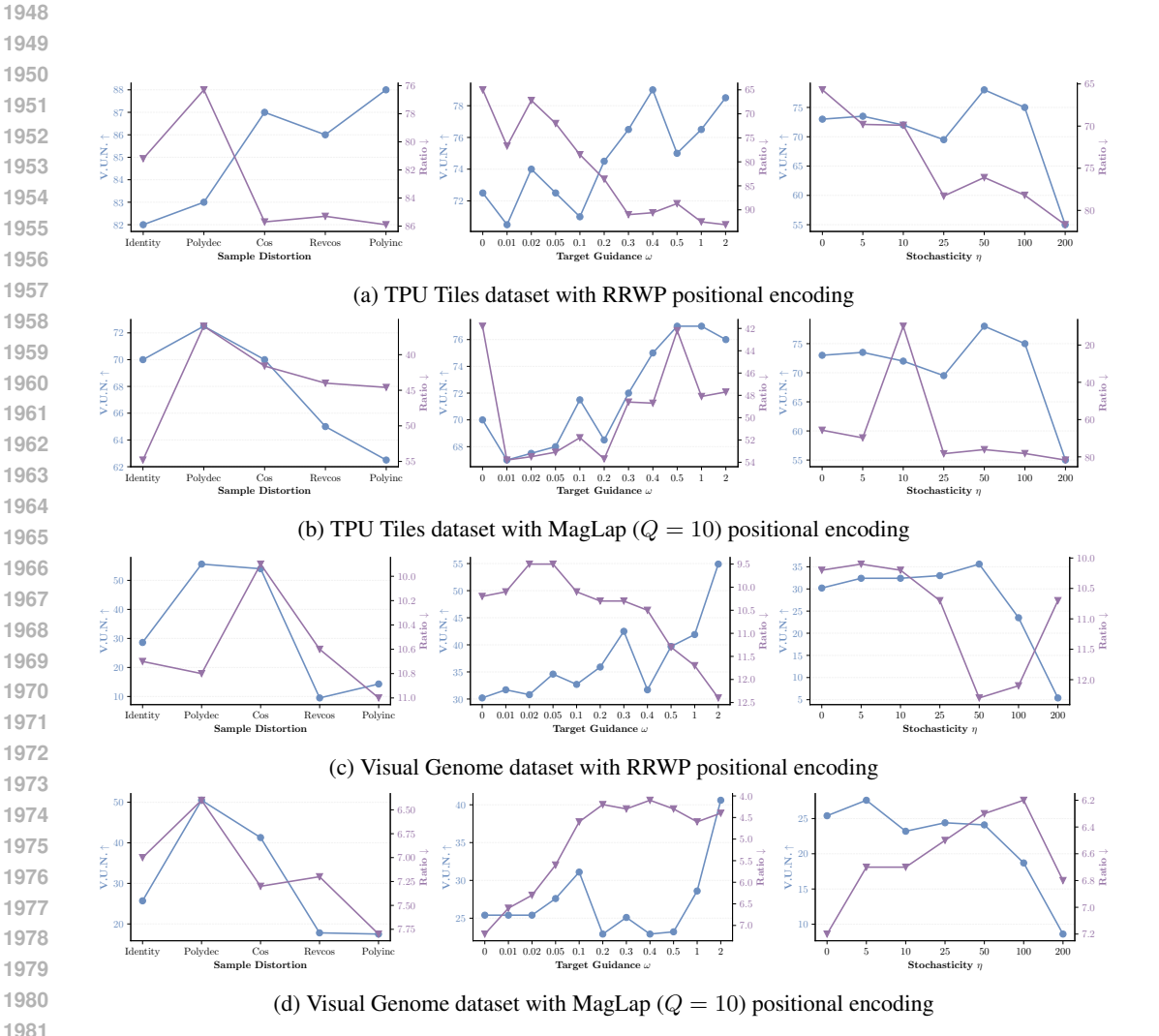


Figure 5: Sampling optimization curves for the synthetic datasets with 100 sampling steps and 5 sampling runs. We represent V.U.N. (blue) and MMD ratio (purple) and optimize for best trade-off for each of the three parameters individually.

The results for the synthetic datasets in Figure 4 illustrate that the sampling hyperparameters influence the generative performance. We observe that different values can lead to variations in both V.U.N. and the structural ratio. However, a higher V.U.N. does not necessarily correspond to a lower ratio. While certain configurations tend to perform well across both RRWP and MagLap positional encodings, the improvements are generally modest, suggesting that optimal settings may vary slightly depending on the dataset and positional encoding strategy used.

A similar pattern is observed in the results for the real-world datasets (TPU Tiles and Visual Genome), as shown in Figure 5. The sampling hyperparameters continue to affect generation performance, and there is no clear one-to-one relationship between V.U.N. and ratio. As with the synthetic datasets, some hyperparameter combinations show slightly more consistent behavior across positional encodings, but overall, the best hyperparameters combination remain dependent on the dataset and positional encoding used.

I ITERATIVE REFINEMENT METHODS FOR GRAPH GENERATION

I.1 Graph iterative refinement methods

Within the realm of undirected graph generation, discrete state-space iterative refinement approaches (Vignac et al., 2023a; Xu et al., 2024; Siraudin et al., 2024; Qin et al., 2025a) have emerged as a powerful framework for capturing the intricate dependencies that govern target graph distributions. These methods achieve state-of-the-art performance by naturally aligning with the structure of graphs: they operate directly in discrete state spaces, matching the inherent discreteness of adjacency matrices, and respect node permutation equivariances due to their one-shot prediction formulation. These characteristics make iterative refinement approaches particularly well-suited for the task of directed graph generation.

These methods comprise two main processes: a noising process and a denoising process. For consistency, we define t=0 as corresponding to fully noised graphs and t=1 to clean graphs. The noising process runs from t=1 to t=0, progressively corrupting the original graphs, while the denoising process learns how to reverse this trajectory, running from t=0 to t=1.

Denoising is performed using a neural network parametrized by θ ,

$$\mathbf{p}_{1|t}^{\theta}(\cdot|G_t) = \left(\left(p_{1|t}^{\theta,(n)}(x_1^{(n)} \mid G_t) \right)_{1 \le n \le N}, \left(p_{1|t}^{\theta,(i,j)}(e_1^{(i,j)} \mid G_t) \right)_{1 \le i \ne j \le N} \right), \tag{38}$$

which predicts categorical distributions over nodes and edges given a noised graph G_t . In practice, $\mathbf{p}_{1|t}^{\theta}(\cdot|G_t)$ is parameterized using a graph transformer such as the one from Dwivedi & Bresson (2021), which allows for expressive modeling of complex graph structures. The network is trained using a cross-entropy loss applied independently to each node and each edge:

$$\mathcal{L} = \mathbb{E}_{t,G_1,G_t} \left[-\sum_{n} \log \left(p_{1|t}^{\theta,(n)} \left(x_1^{(n)} \mid G_t \right) \right) - \lambda \sum_{i \neq j} \log \left(p_{1|t}^{\theta,(i,j)} \left(e_1^{(i,j)} \mid G_t \right) \right) \right], \quad (39)$$

where the expectation is taken over time t sampled from a predefined distribution over [0,1] (e.g., uniform); $G_1 \sim p_1(G_1)$ is a clean graph from the dataset; and $G_t \sim p_t(G_t|G_1)$ is its noised version at time t. The hyperparameter $\lambda \in \mathbb{R}^+$ controls the relative weighting between node and edge reconstruction losses. Once the denoising network is trained, different graph iterative refinement methods vary in how they leverage the predicted $\mathbf{p}_{1|t}^{\theta}(\cdot|G_t)$ to progressively recover the clean graphs.

I.2 DISCRETE FLOW MATCHING FOR GRAPH GENERATION

Among graph iterative refinement methods, Discrete Flow Matching (DFM) (Campbell et al., 2024; Gat et al., 2024) has recently emerged as a particularly powerful framework. By decoupling the training and sampling processes, DFM enables a broader and more flexible design space, which has been shown to improve generative performance. This framework has proven particularly effective for undirected graph generation (Qin et al., 2025a).

The noising process in DFM is defined as a linear interpolation between the data distribution and a pre-specified noise distribution. This interpolation is applied independently to each variable, corresponding to each node and each edge in the case of graphs:

$$p_{t|1}^{X}(x_t^{(n)} \mid x_1^{(n)}) = t \,\delta(x_t^{(n)}, x_1^{(n)}) + (1 - t) \,p_{\text{noise}}^{X}(x_t^{(n)}),\tag{40}$$

where $\delta(\cdot,\cdot)$ is the Kronecker delta and p_{noise}^X is a reference distribution over node categories. A similar construction is used for edges. Therefore, the complete noising process corresponds to independently noising each node and edge through $p_{t|1}^X$ and $p_{t|1}^E$, respectively.

To reverse this process, DFM models denoising as a Continuous-Time Markov Chain (CTMC). Starting from an initial distribution p_0 , the generative process evolves according to:

$$\mathbf{p}_{t+\Delta t|t}(G_{t+\Delta t} \mid G_t) = \delta(G_t, G_{t+\Delta t}) + \mathbf{R}_t(G_t, G_{t+\Delta t}) \,\mathrm{d}t,\tag{41}$$

where R_t is the CTMC rate matrix. In practice, this update is approximated over a finite interval Δt , in an Euler method step, with the rate matrix estimated from the network predictions $\mathbf{p}_{1|t}^{\theta}(\cdot \mid G_t)$ via:

$$\mathbf{R}_{t}^{\theta}(G_{t}, G_{t+\Delta t}) = \sum_{n} \delta(G_{t}^{\setminus (n)}, G_{t+\Delta t}^{\setminus (n)}) \mathbb{E}_{p_{1|t}^{\theta, (n)}(x_{1}^{(n)}|G_{t})} \left[R_{t}^{(n)}(x_{t}^{(n)}, x_{t+\Delta t}^{(n)} \mid x_{1}^{(n)}) \right]$$
(42)

$$+ \sum_{i \neq j} \delta(G_t^{\setminus (i,j)}, G_{t+\Delta t}^{\setminus (i,j)}) \mathbb{E}_{p_{1|t}^{\theta,(i,j)}(e_1^{(i,j)}|G_t)} \left[R_t^{(i,j)}(e_t^{(i,j)}, e_{t+\Delta t}^{(i,j)} \mid e_1^{(i,j)}) \right], \quad (43)$$

where the $G^{\setminus (d)}$ denote the full graph G except variable d (node or edge). The Knonecker deltas ensure that each variable-specific rate matrix, $R_t^{(n)}$ or $R_t^{(i,j)}$, is applied independently at each node and edge, respectively. Finally, each node-specific rate matrix is defined as:

$$R_{t}(x_{t}^{(n)}, x_{t+\Delta t}^{(n)} \mid x_{1}^{(n)}) = \frac{\text{ReLU}\left[\partial_{t} p_{t|1}(x_{t+\Delta t}^{(n)} \mid x_{1}^{(n)}) - \partial_{t} p_{t|1}(x_{t}^{(n)} \mid x_{1}^{(n)})\right]}{X_{t}^{>0} p_{t|1}(x_{t}^{(n)} \mid x_{1}^{(n)})}, \tag{44}$$

for each node $x^{(n)}$, where $X_t^{>0} = \left|\left\{x_t^{(n)}: p_{t|1}(x_t^{(n)}\mid x_1^{(n)})>0\right\}\right|$. An analogous definition applies for edge rate matrices.

I.3 DISCRETE DIFFUSION FOR GRAPH GENERATION

Among discrete diffusion-based models for undirected graphs, DIGRESS (Vignac et al., 2023a), grounded in the structured discrete diffusion framework (Austin et al., 2021), has been particularly influential. This approach mostly differs from the DFM-based formulation described in Appendix I.2, as it operates in discrete time, with the denoising process modeled as a Discrete-Time Markov Chain (DTMC), in contrast to the continuous-time formulation used in DFM.

The forward, or noising, process is modeled as a Markov noise process q, which generates a sequence of progressively noised graphs G_t , for $t=1,\ldots,T$. At each timestep, node and edge tensors are perturbed using categorical transition matrices $[\mathbf{Q}_t^X]^{(i,j)} = q(x_t=j \mid x_{t-1}=i)$ and $[\mathbf{Q}_t^E]^{(i,j)} = q(e_t=j \mid e_{t-1}=i)$, respectively. This process induces structural changes such as edge addition or deletion, and edits to node and edge categories. The transition probabilities can be summarized as:

$$q(G_t \mid G_{t-1}) = \left(\mathbf{X}_{t-1}\mathbf{Q}_t^X, \, \mathbf{E}_{t-1}\mathbf{Q}_t^E\right) \quad \text{and} \quad q(G_t \mid G) = \left(\mathbf{X}\prod_{i=1}^t \mathbf{Q}_i^X, \, \mathbf{E}\prod_{i=1}^t \mathbf{Q}_i^E\right). \tag{45}$$

In practice, these noise matrices are implemented based on the marginal noise model, defined as:

$$\mathbf{Q}_t^X = \alpha^t \mathbf{I} + (1 - \alpha^t) \mathbf{1}_X \mathbf{m}_X^\top \quad \text{and} \quad \mathbf{Q}_t^E = \alpha^t \mathbf{I} + (1 - \alpha^t) \mathbf{1}_E \mathbf{m}_E^\top,$$

where α^t transitions from 1 to 0 with t according to the popular cosine scheduling (Nichol & Dhariwal, 2021). The vectors $\mathbf{1}_X \in \{1\}^X$ and $\mathbf{1}_E \in \{1\}^{E+1}$ are filled with ones, and $\mathbf{m}_X \in \Delta^X$ and $\mathbf{m}_E \in \Delta^{E+1}$ are vectors filled with the marginal node and edge distributions, respectively².

This noising process can be rewritten using the analogous notation to the one used for DFM in Equation (46) as:

$$p_{t'|1}^{X}(x_{t'}^{(n)} \mid x_{1}^{(n)}) = \bar{\alpha}(t')\,\delta(x_{t'}^{(n)}, x_{1}^{(n)}) + (1 - \bar{\alpha}(t'))\,p_{\text{noise}}^{X}(x_{t'}^{(n)}),\tag{46}$$

with $t'=1-\frac{t}{T}$ and $\bar{\alpha}(t')=\cos\left(\frac{\pi}{2}\frac{1-t'+s}{1+s}\right)^2$, with a small s. Importantly, this function is only evaluated in the discrete values of time considered for the DTMC associated to the diffusion model. For the remaining of this section, we consider the transformed variable t' as the reference time variable.

In the reverse, or denoising, process, a clean graph is progressively built leveraging the denoising neural network predictions $p_{1|t'}^{\theta}(\cdot|G_t')$, analogously to the DFM setting. In particular, the model

²We denote the probability simplex of the state-space of cardinality Z by Δ^Z

begins from a noise sample G_0 and iteratively predicts the clean graph G_1 by modeling node and edge distributions conditioned on the full graph structure. The reverse transition is defined as:

$$p_{t'+\Delta t'|t'}^{\theta}(G_{t'+\Delta t'} \mid G_{t'}) = \prod_{i=1}^{N} p_{t'+\Delta t'|t'}^{\theta}(x_{t'+\Delta t'}^{(n)} \mid G_{t'}) \prod_{1 \le i < j \le N}^{N} p_{t'+\Delta t'|t'}^{\theta}(e_{t'+\Delta t'}^{(i,j)} \mid G_{t'}). \tag{47}$$

with each of the node and edge denoising terms are computer through the following marginalization:

$$\boldsymbol{p}_{t'+\Delta t'|t'}^{\theta}(x_{t'+\Delta t'}^{(n)} \mid G_{t'}) = \sum_{x_{1}^{(n)} \in \{1,\dots,X\}} \boldsymbol{p}_{t'+\Delta t'|1,t'}(x_{t'+\Delta t'}^{(n)} \mid x_{1}^{(n)}, G_{t'}) \ p_{1|t'}^{\theta,(n)}(x_{1}^{(n)} \mid G_{t'}), \quad (48)$$

and similarly for edges. To compute the missing posterior term in Equation (48), $p_{t'+\Delta t'|1,t'}(x_{t'+\Delta t'}^{(n)}|x_1^{(n)},G_{t'})$, we equate it to the posterior term of the forward process:

$$p_{t'+\Delta t'|1,t'}(x_{t'+\Delta t'}^{(n)}|x_1^{(n)}, G_{t'}) = \begin{cases} \frac{\mathbf{x}_{t'}^{(n)}(\mathbf{Q}_{t'}^X)^{\top} \odot \mathbf{x}_1^{(n)} \bar{\mathbf{Q}}_{t'+\Delta t'}^X}{\mathbf{x}_{t'}^{(n)} \bar{\mathbf{Q}}_{t'}^X \mathbf{x}_1^{(n)}} & \text{if } q(x_{t'}^{(n)}|x_1^{(n)}) > 0, \\ 0 & \text{otherwise,} \end{cases}$$
(49)

where $\mathbf{x}_{t'}^{(n)}$ and $\mathbf{x}_1^{(n)}$ denote the vectorized versions of $x_{t'}^{(n)}$ and $x_1^{(n)}$, respectively. Crucially, and contrarily to DFM, the sampling strategy with discrete diffusion is fixed at training time, which restricts the design space of this generative framework.

J USE OF LARGE LANGUAGE MODELS

Large Language Models (LLMs) were used as a writing assistant tool in the preparation of this manuscript. Specifically, they were employed to aid in writing, checking spelling, and editing for clarity. Nonetheless, all text produced with the assistance of LLMs was carefully reviewed, verified, and revised by the authors to ensure accuracy and appropriateness. The use of LLMs was limited to these support functions, and the authors take full responsibility for the final content of the paper.

K VISUALIZATIONS

In this section, we present visualizations of the digraphs generated with DIRECTO for the different synthetic and real-world datasets and combinations of positional encodings reported in the main paper. To allow for a fair comparison between original and generated digraphs, we additionally report digraphs from the train splits of the original datasets.

Original digraphs for the SBM dataset are shown in Figure 6. Figure 7 and Figure 8 show examples of digraphs from the Stochastic Block Model (SBM), where clear community structures are visible, consistent with the underlying block partitioning. These visualizations help illustrate how the positional encodings preserve modularity and inter-cluster connectivity. Similarly, Figure 9 shows original digraphs from the ER-DAG dataset, with Figure 10 and Figure 11 displaying generated digraphs from the Erdős–Rényi (ER-DAG) model. In this case, digraphs are plotted with nodes in topological order, to highlight the acyclicity.

For the real-world datasets, in particular for the TPU Tiles dataset, which consists of directed acyclic graphs (DAGs) representing hardware execution plans, we can see the original DAGs in Figure 12 From the visualizations in Figure 13 and Figure 14 we see that the model is able to capture and generalize across structural patterns that emerge in computational workloads. In a similar way as before, digraphs are represented with nodes in topological order to highlight acyclicity.

Finally, for the Visual Genome dataset, we represent the three different node types: objects (blue), relationships (red) and attributes (green), alongside their respective node label. Figure 15 shows the original graphs, while Figure 16 and Figure 17 report the generations. They show how the model effectively captures the semantic and relational structure across these node categories, learning meaningful patterns that align with human understanding (i.e. *a person wears a yellow shirt*, or *a white cloud in the sky*).

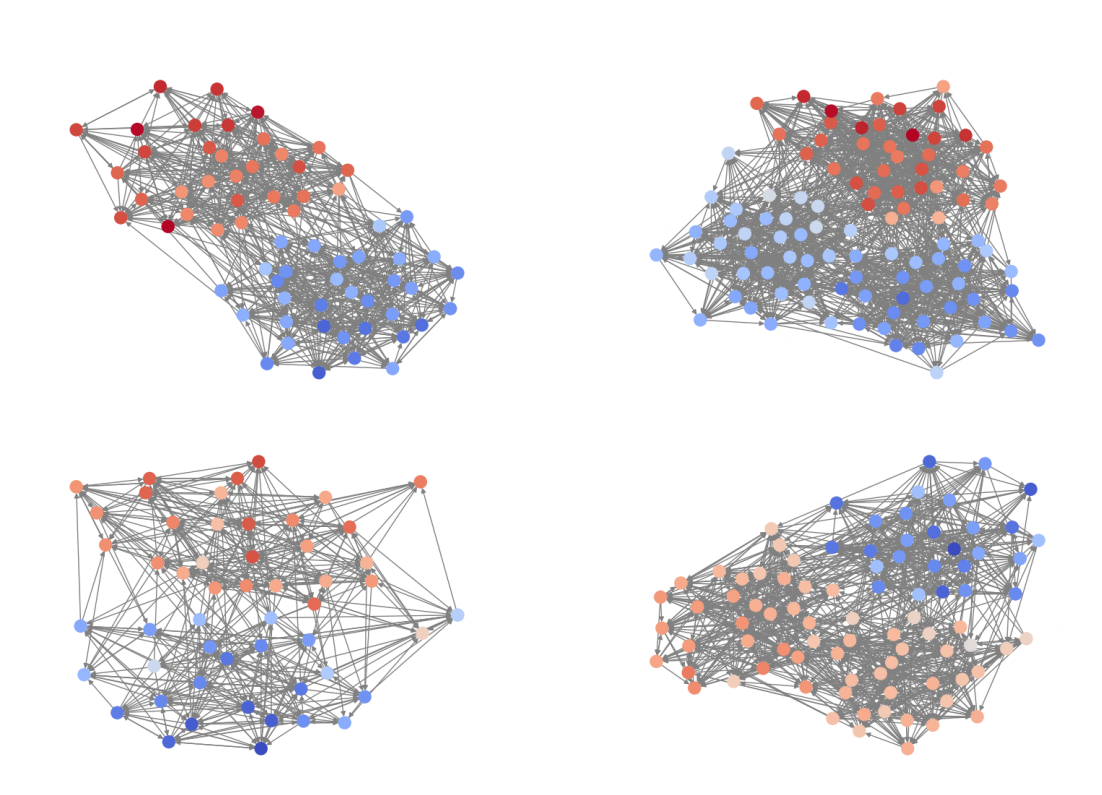


Figure 6: Visualizations of original synthetic digraphs from the train splits of the SBM dataset.

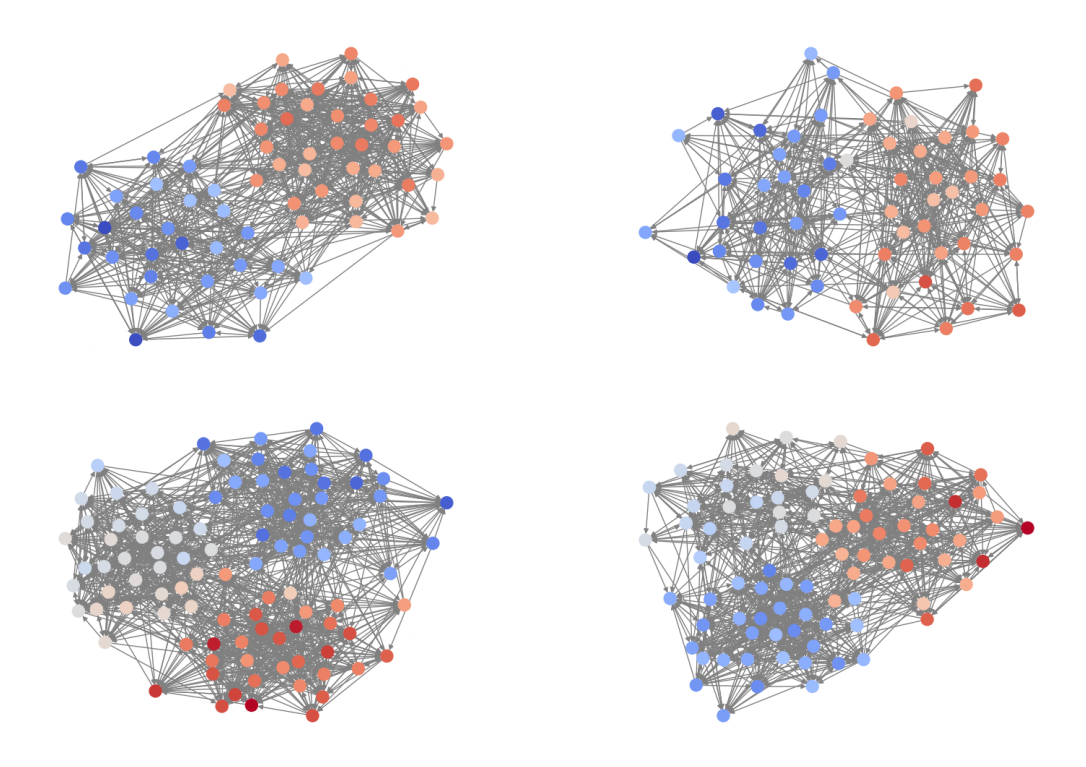


Figure 7: Visualizations of four generated digraphs for the SBM dataset with RRWP positional encoding.

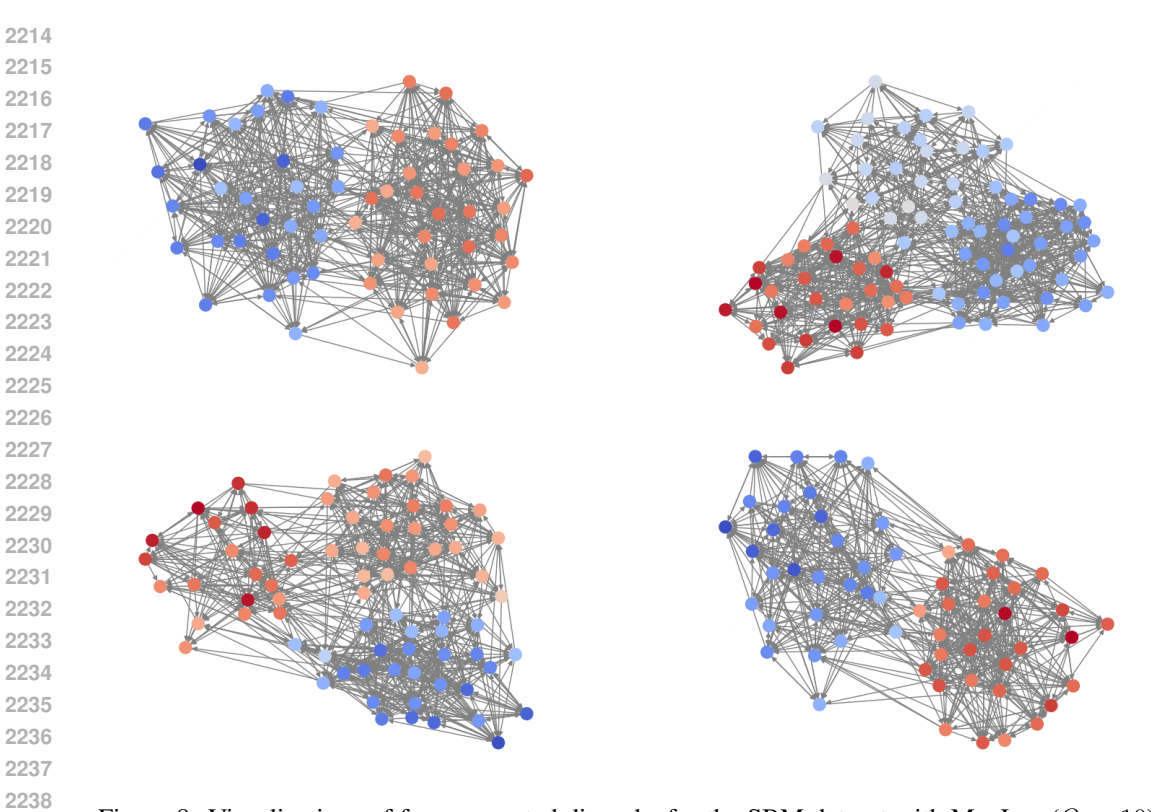


Figure 8: Visualizations of four generated digraphs for the SBM dataset with MagLap (Q=10) positional encoding.

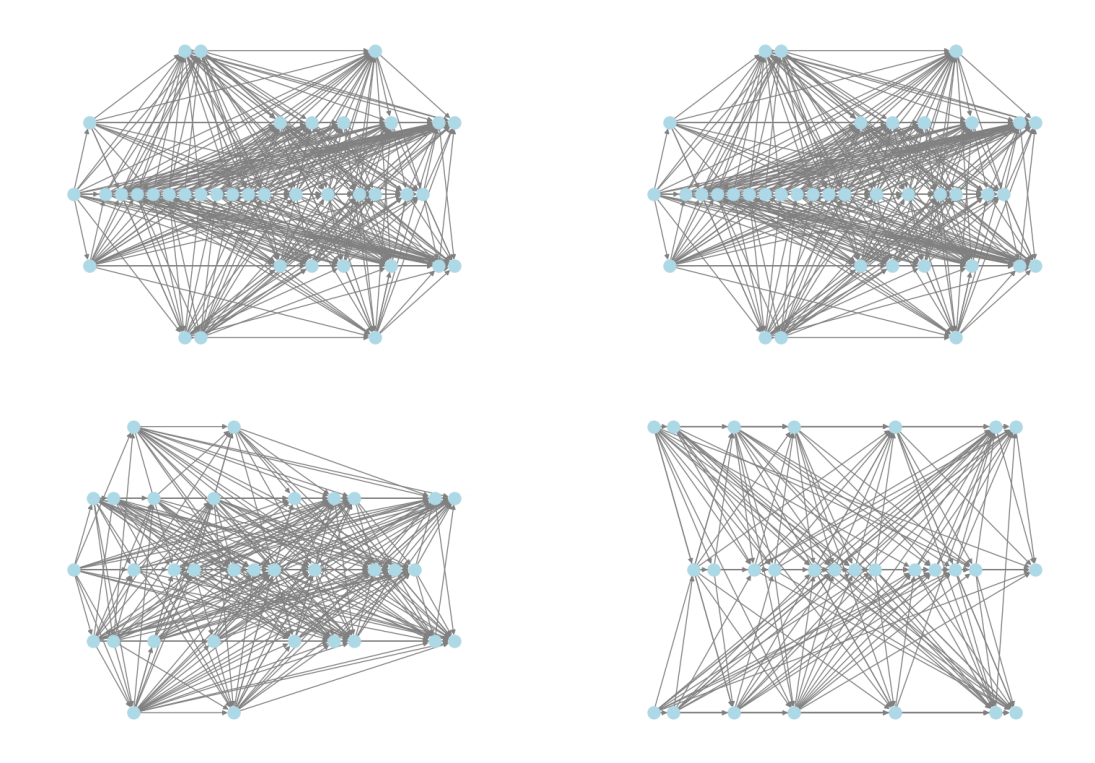


Figure 9: Visualizations of original synthetic digraphs from the train splits of the ER-DAG datasets. Nodes are in topological ordering to highlight the acyclic structure.

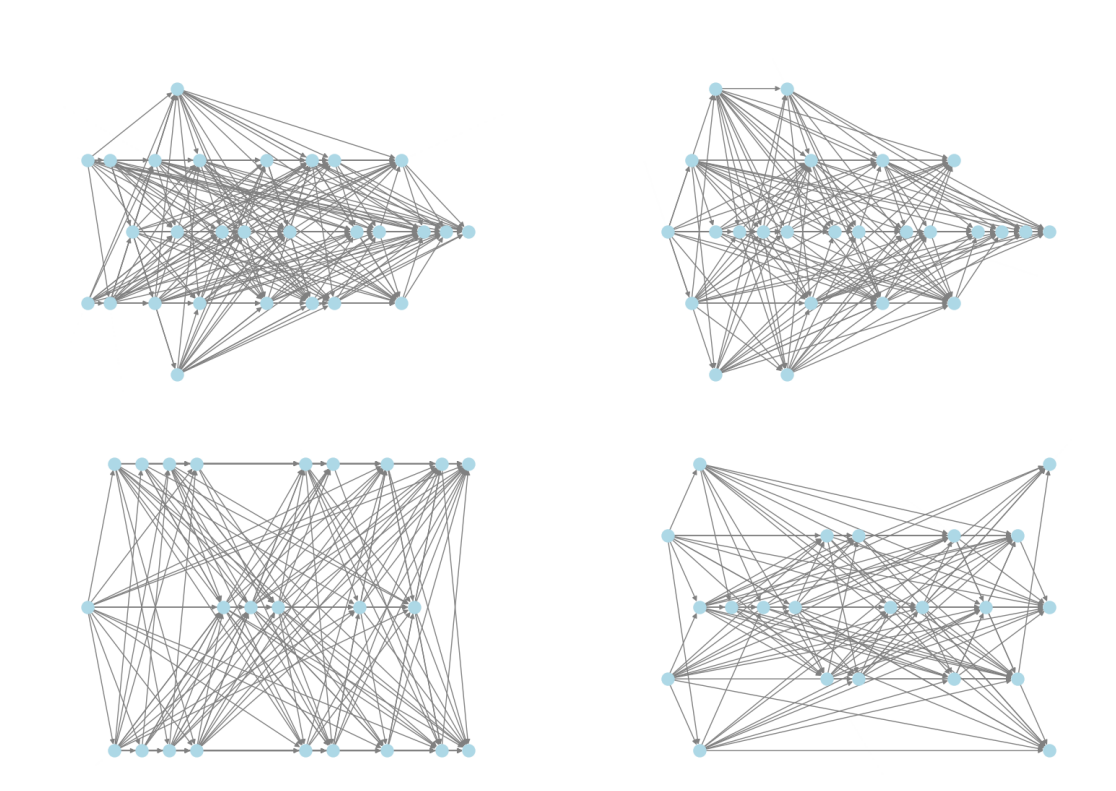


Figure 10: Visualizations of four generated digraphs for the ER-DAG dataset with RRWP positional encoding. Nodes are in topological ordering to highlight the acyclic structure.

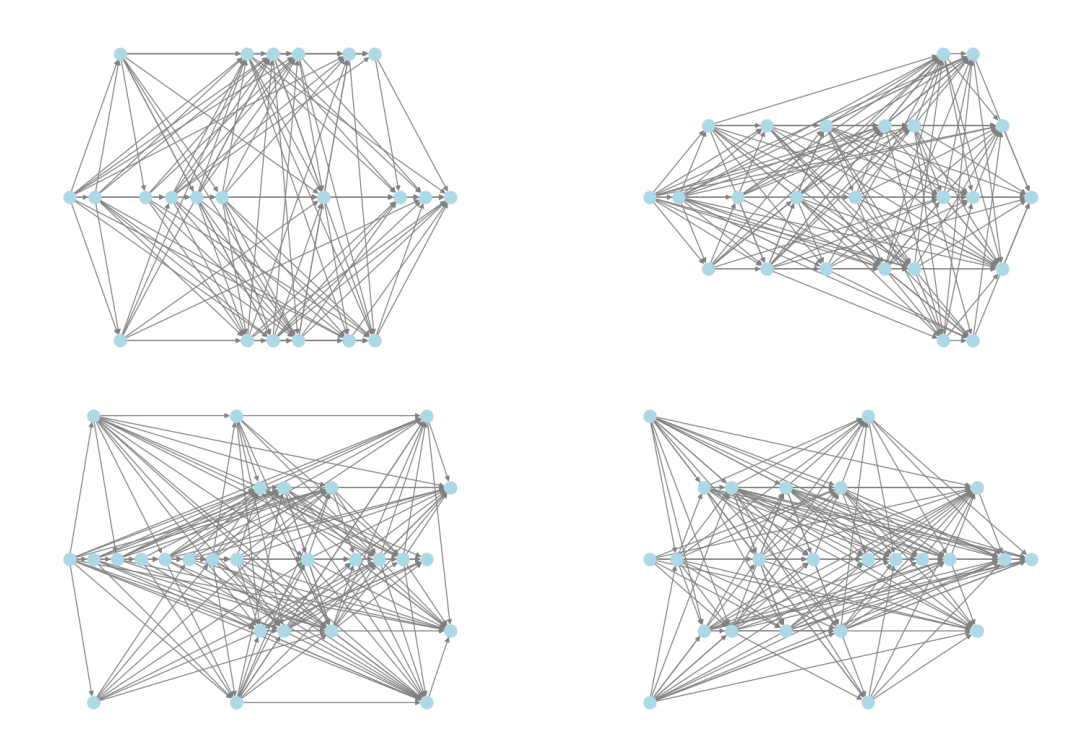


Figure 11: Visualizations of four generated digraphs for the ER-DAG dataset with MagLap (Q=10) positional encoding. Nodes are in topological ordering to highlight the acyclic structure.

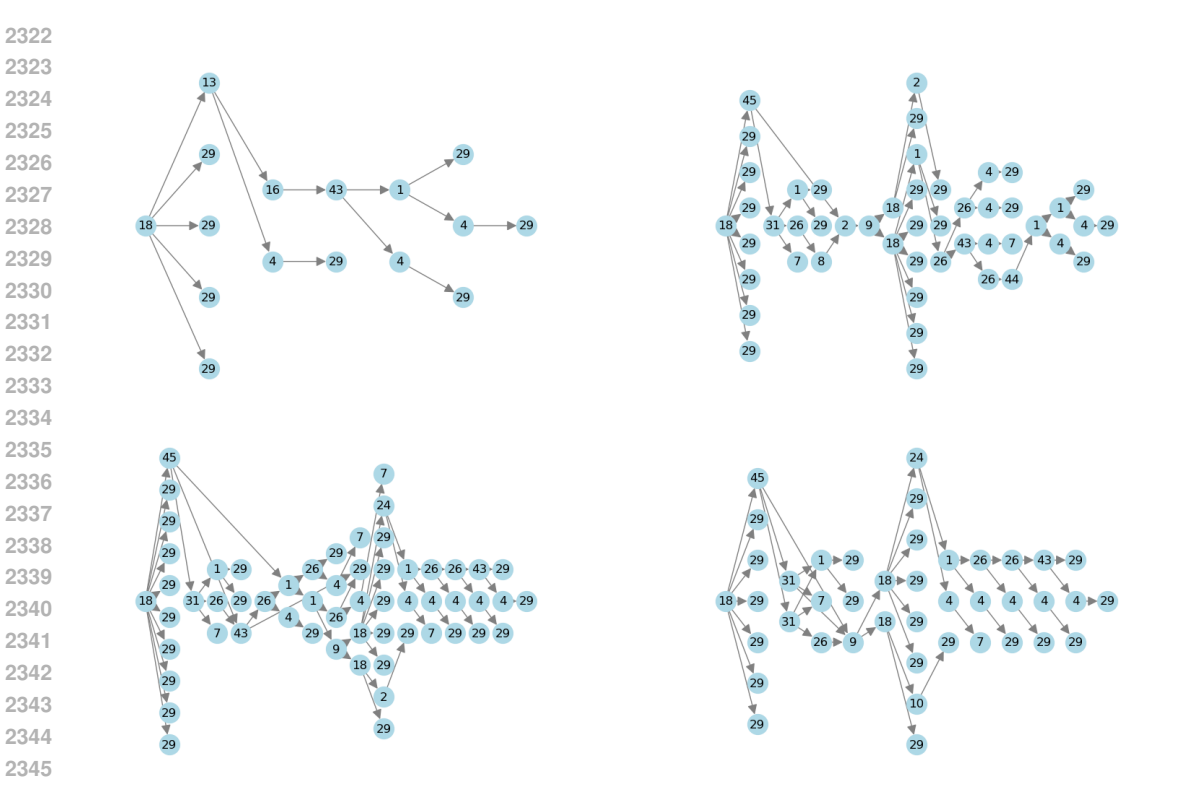


Figure 12: Visualizations of original real-world digraphs from the train splits of the TPU Tiles dataset. Nodes are in topological ordering to highlight the acyclic structure.

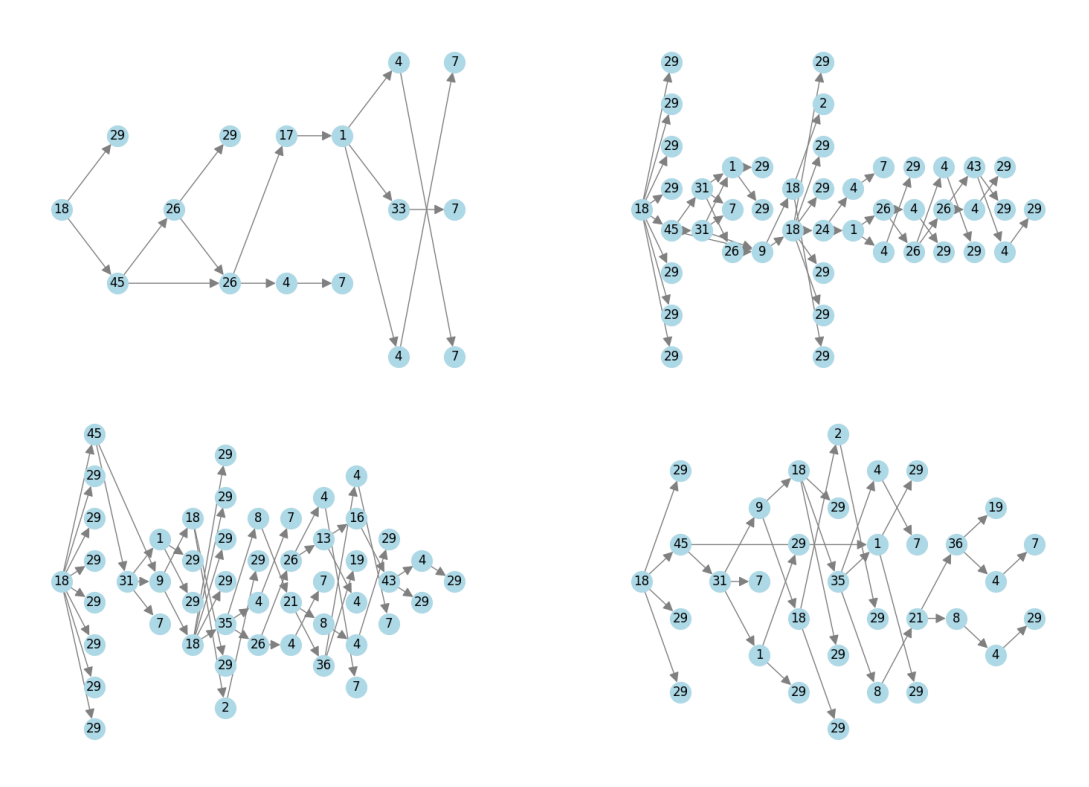


Figure 13: Visualizations of four generated dgraphs for the TPU Tiles dataset with RRWP positional encoding. Nodes are in topological ordering to highlight the acyclic structure.

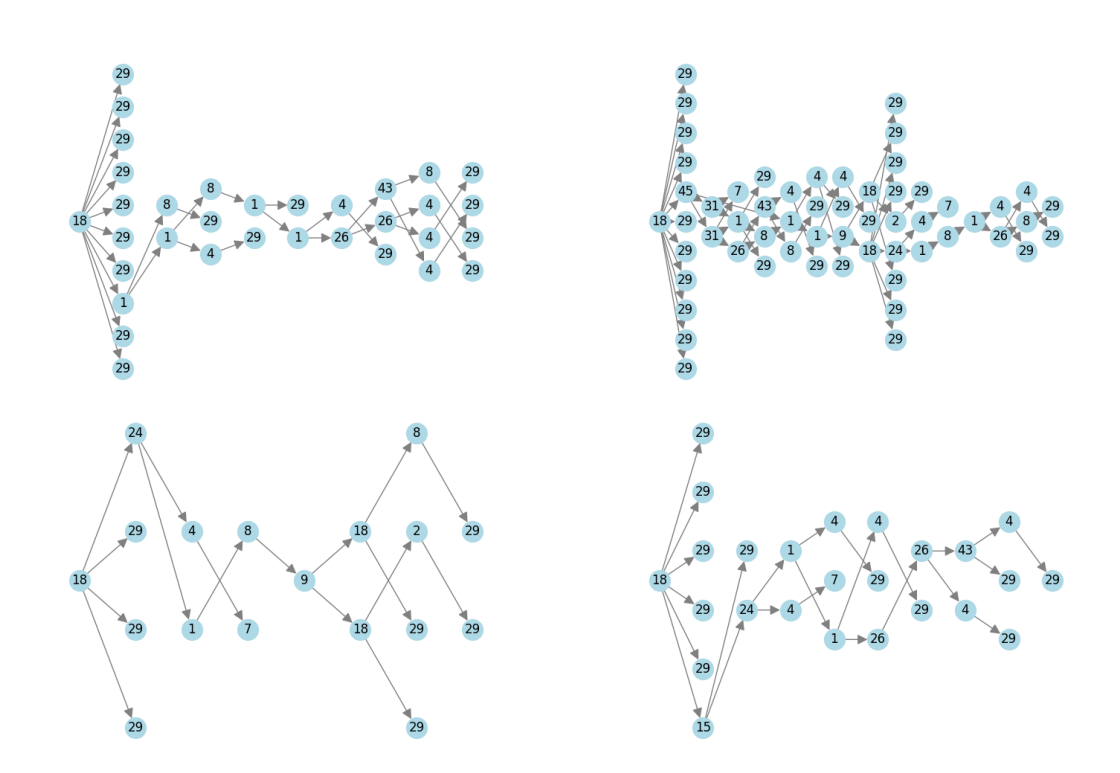


Figure 14: Visualizations of four generated digraphs for the TPU Tiles dataset with MagLap (Q=5) positional encoding. Nodes are in topological ordering to highlight the acyclic structure.

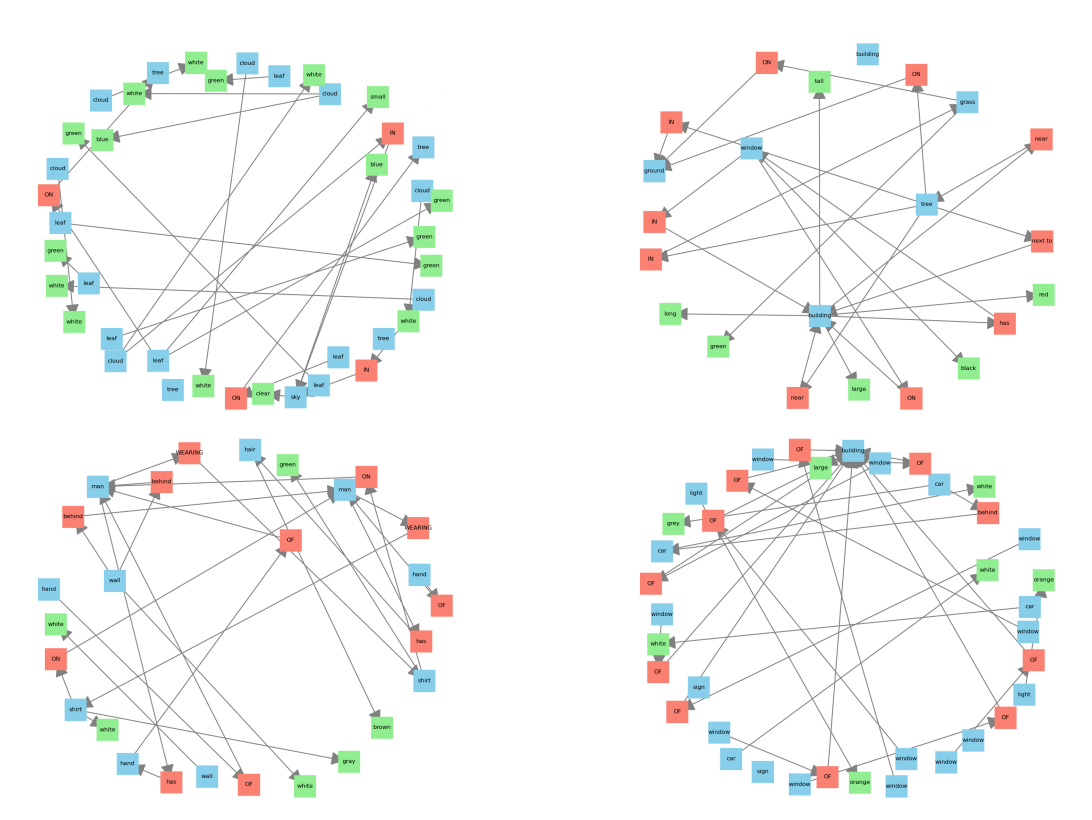


Figure 15: Visualizations of original real-world digraphs from the train splits of the Visual Genome dataset. Nodes represent objects (blue), relationships (red), and attributes (green).

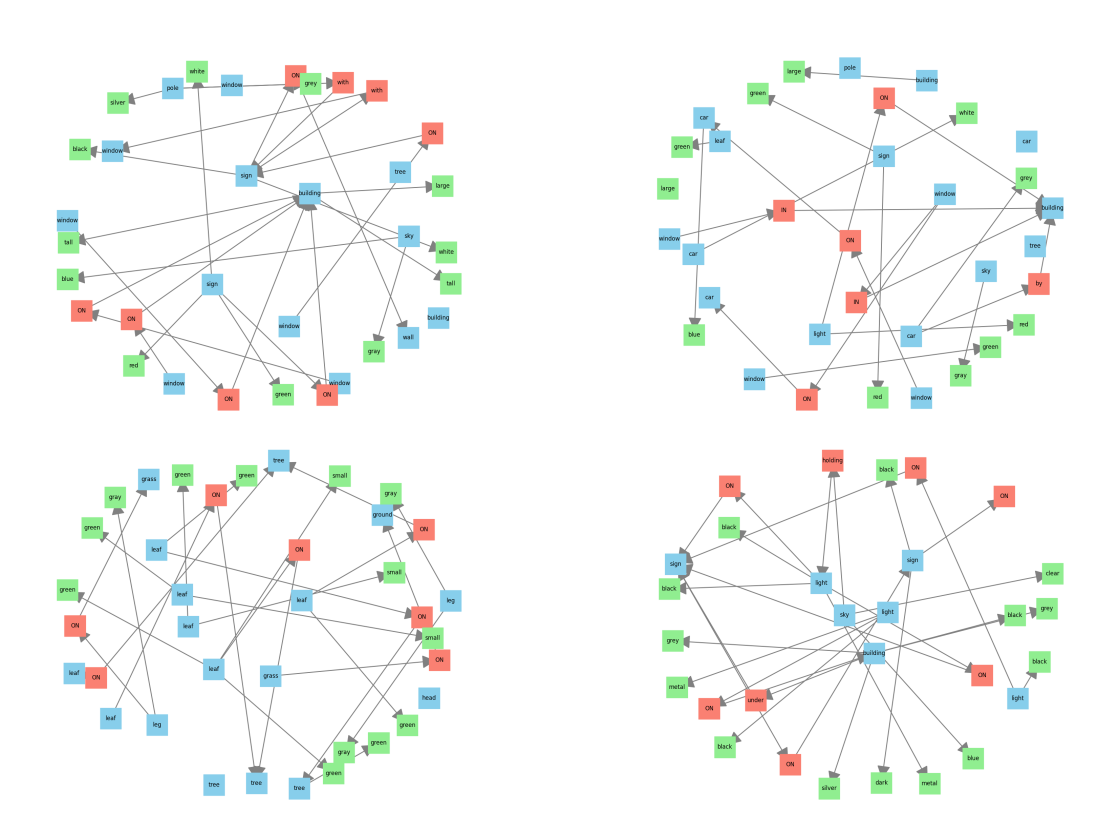


Figure 16: Visualizations of four generated digraphs for the Visual Genome dataset with RRWP positional encoding. Nodes represent objects (blue), relationships (red), and attributes (green).

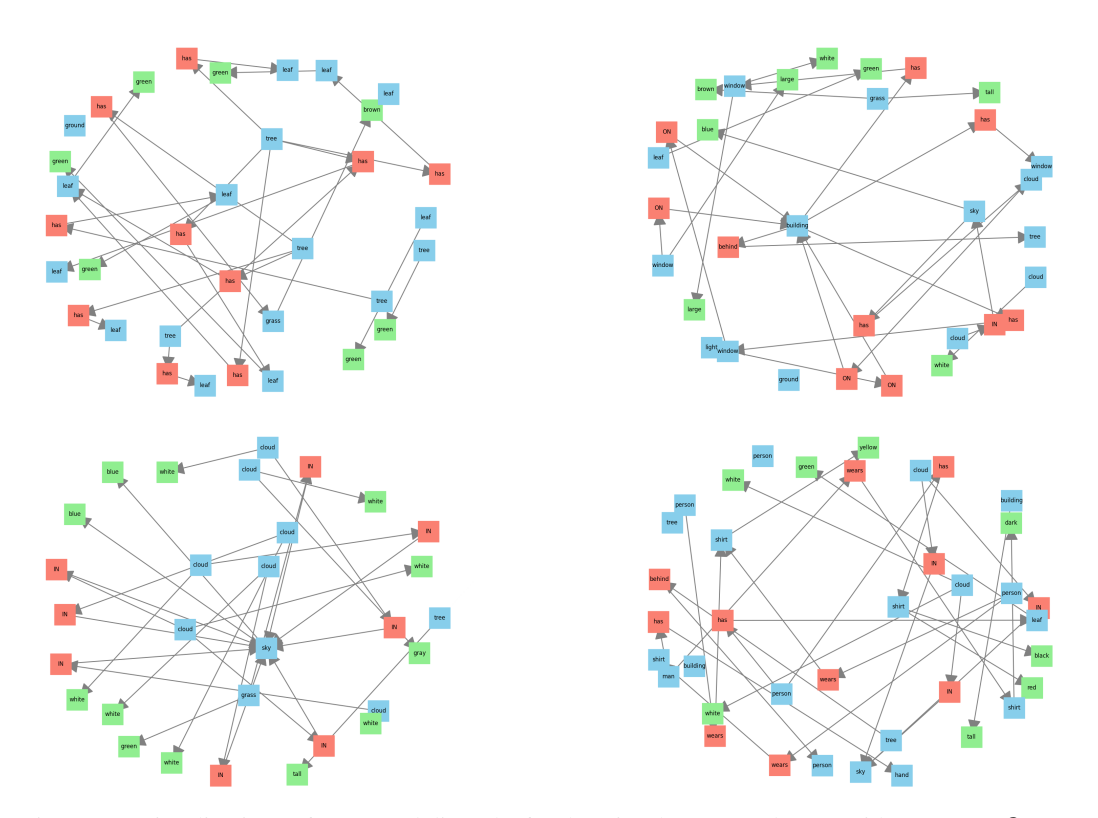


Figure 17: Visualizations of generated digraphs for the Visual Genome dataset with MagLap (Q=5) positional encoding. Nodes represent objects (blue), relationships (red), and attributes (green).

L LIMITATIONS AND FUTURE WORK

 Although DIRECTO shows strong performance in the generation of directed graphs, several avenues for future work could further enhance its scalability, controllability, and applicability.

Scalability to Large Graphs and Datasets: Directed graphs present a combinatorial explosion in the space of possible edges due to asymmetry, posing challenges in both training and sampling efficiency. Future work could explore *sparsity-aware attention mechanisms* (Qin et al., 2025b) to reduce quadratic memory and computational complexity. *Hierarchical* or *latent diffusion approaches* (Bergmeister et al., 2024; Jang et al., 2024; Yang et al., 2024) may allow the model to efficiently generate large-scale graphs by operating at multiple levels of granularity or in a lower-dimensional latent space. Investigating adaptive sampling schedules and dataset subsampling strategies could also help manage computational costs without sacrificing model quality.

Conditional Graph Generation: Many real-world applications require generating graphs conditioned on specific properties or context, such as node features, initial subgraphs, or global graph characteristics. DIRECTO already supports *classifier-free* conditional generation, which allows flexible conditioning without requiring additional networks. However, this approach may not be optimal for all tasks, and exploring *alternative conditional strategies* (such as learned conditional embeddings or auxiliary networks) could further improve performance. Such extensions would enable targeted graph design, e.g., generating traffic networks with predefined entry/exit nodes, molecular graphs with given scaffolds, or DAGs adhering to specific causal structures

Explicit Structural Constraints: While DIRECTO can implicitly learn structural constraints such as acyclicity, certain domains require *strict adherence* to properties like DAG structure, planarity, or node degree limits. Integrating ideas from methods such as ConStrucy (Madeira et al., 2024) or PRODIGY (Sharma et al., 2024) could enforce these constraints explicitly, enhancing control over generated graphs. Future research could also explore *soft vs. hard constraint integration*, allowing a trade-off between flexibility and domain-specific validity.

Integration with Downstream Tasks: Beyond purely generative evaluation, integrating DIRECTO with downstream tasks such as causal inference, traffic simulation, or molecular optimization—could highlight practical benefits and guide model improvements. Extending the metrics in the benchmark to further reflect *task-specific objectives* could be relevant to quantify real-world impact.

Interpretability and Controllability: Understanding which components (e.g., dual attention vs. directional positional encodings) drive specific structural properties in the generated graphs is an open research question. Future work could investigate *interpretable latent representations* and mechanisms to control generation in a predictable manner.